

REPORT DOCUMENTATION PAGE			Form Approved OMB NO. 0704-0188		
<p>The public reporting burden for this collection of information is estimated to average 1 hour per response, including the time for reviewing instructions, searching existing data sources, gathering and maintaining the data needed, and completing and reviewing the collection of information. Send comments regarding this burden estimate or any other aspect of this collection of information, including suggestions for reducing this burden, to Washington Headquarters Services, Directorate for Information Operations and Reports, 1215 Jefferson Davis Highway, Suite 1204, Arlington VA, 22202-4302. Respondents should be aware that notwithstanding any other provision of law, no person shall be subject to any penalty for failing to comply with a collection of information if it does not display a currently valid OMB control number.</p> <p>PLEASE DO NOT RETURN YOUR FORM TO THE ABOVE ADDRESS.</p>					
1. REPORT DATE (DD-MM-YYYY) 29-08-2012		2. REPORT TYPE Final Report		3. DATES COVERED (From - To) 14-Jul-2009 - 13-Dec-2013	
4. TITLE AND SUBTITLE DESIGN AND CONTROL OF OMNIDIRECTIONAL UNMANNED GROUND VEHICLES FOR ROUGH TERRAIN			5a. CONTRACT NUMBER W911NF-09-1-0334		
			5b. GRANT NUMBER		
			5c. PROGRAM ELEMENT NUMBER 633005		
6. AUTHORS Karl Iagnemma			5d. PROJECT NUMBER		
			5e. TASK NUMBER		
			5f. WORK UNIT NUMBER		
7. PERFORMING ORGANIZATION NAMES AND ADDRESSES Massachusetts Institute of Technology (MIT) Office of Sponsored Programs Bldg. E19-750 Cambridge, MA 02139 -4307			8. PERFORMING ORGANIZATION REPORT NUMBER		
9. SPONSORING/MONITORING AGENCY NAME(S) AND ADDRESS(ES) U.S. Army Research Office P.O. Box 12211 Research Triangle Park, NC 27709-2211			10. SPONSOR/MONITOR'S ACRONYM(S) ARO		
			11. SPONSOR/MONITOR'S REPORT NUMBER(S) 56552-EV.4		
12. DISTRIBUTION AVAILABILITY STATEMENT Approved for Public Release; Distribution Unlimited					
13. SUPPLEMENTARY NOTES The views, opinions and/or findings contained in this report are those of the author(s) and should not be construed as an official Department of the Army position, policy or decision, unless so designated by other documentation.					
14. ABSTRACT Research under this ARO grant has studied the design of highly agile ground vehicles. This has involved work in three related areas. First, research was performed on the design and control of ultra high-performance unmanned ground vehicles (UHP-UGVs) that utilize a new wheel drive system to achieve omnidirectional mobility in rough terrain. The result of this research was an experimental demonstration of a prototype UHP-UGV with measurable agility improvement in rough terrain compared to Ackerman or skid-steered vehicles. Next, research focused on the					
15. SUBJECT TERMS Mobile robots, UGVs, terrain, omnidirectional					
16. SECURITY CLASSIFICATION OF:			17. LIMITATION OF ABSTRACT UU	15. NUMBER OF PAGES	19a. NAME OF RESPONSIBLE PERSON Karl Iagnemma
a. REPORT UU	b. ABSTRACT UU	c. THIS PAGE UU			19b. TELEPHONE NUMBER 617-452-3262

Report Title

DESIGN AND CONTROL OF OMNIDIRECTIONAL UNMANNED GROUND VEHICLES FOR ROUGH TERRAIN

ABSTRACT

Research under this ARO grant has studied the design of highly agile ground vehicles. This has involved work in three related areas. First, research was performed on the design and control of ultra high-performance unmanned ground vehicles (UHP-UGVs) that utilize a new wheel drive system to achieve omnidirectional mobility in rough terrain. The result of this research was an experimental demonstration of a prototype UHP-UGV with measurable agility improvement in rough terrain compared to Ackerman or skid-steered vehicles. Next, research focused on the development of an entirely novel omnidirectional vehicle with anisotropic friction wheels. The wheels are arranged such that the robot wheel exhibits high traction in its driving direction (much like a conventional tire), but low traction when sliding laterally.

Exploiting this “anisotropic friction” property, the proposed wheel enables a vehicle to realize omnidirectional motion (i.e. the vehicle can move any direction within the plane—forward, back, or laterally). Finally, research focused on developing novel experimental methods to analyze detailed robot-terrain interaction phenomena, with an ultimate goal of developing models that will lead to improved robot mobility performance.

Enter List of papers submitted or published that acknowledge ARO support from the start of the project to the date of this printing. List the papers, including journal references, in the following categories:

(a) Papers published in peer-reviewed journals (N/A for none)

Received

Paper

TOTAL:

Number of Papers published in peer-reviewed journals:

(b) Papers published in non-peer-reviewed journals (N/A for none)

Received

Paper

TOTAL:

Number of Papers published in non peer-reviewed journals:

(c) Presentations

Non Peer-Reviewed Conference Proceeding publications (other than abstracts):

Received Paper

TOTAL:

Number of Non Peer-Reviewed Conference Proceeding publications (other than abstracts):

Peer-Reviewed Conference Proceeding publications (other than abstracts):

Received Paper

08/28/2012	3.00	Karl Iagnemma, Carmine Senatore, Markus Wulfmeier, Paramsothy Jayakumar. INVESTIGATION OF STRESS AND FAILURE IN GRANULAR SOILS FOR LIGHTWEIGHT ROBOTIC VEHICLE APPLICATIONS, 2012 NDIA GROUND VEHICLE SYSTEMS ENGINEERING AND TECHNOLOGY SYMPOSIUM. 2012/08/14 00:00:00, . : ,
	2.00	Genya Ishigami, Jim Overholt, Karl Iagnemma. Multi-material Anisotropic Friction Wheels for Omnidirectional Ground Vehicles, International Conference on Advanced Mechatronics. 2010/10/04 00:00:00, . : ,

TOTAL: 2

Number of Peer-Reviewed Conference Proceeding publications (other than abstracts):

(d) Manuscripts

Received Paper

	1.00	Genya Ishigami, Jim Overholt, Karl Iagnemma. Multi-material Anisotropic Friction Wheels for Omnidirectional Ground Vehicles, ()
--	------	--

TOTAL: 1

Number of Manuscripts:	
Books	
Received	Paper

TOTAL:

Patents Submitted

Patents Awarded

Awards

Best paper award, 2012 GVSETS Conference

Graduate Students

<u>NAME</u>	<u>PERCENT SUPPORTED</u>
FTE Equivalent:	
Total Number:	

Names of Post Doctorates

<u>NAME</u>	<u>PERCENT SUPPORTED</u>
FTE Equivalent:	
Total Number:	

Names of Faculty Supported

<u>NAME</u>	<u>PERCENT SUPPORTED</u>	National Academy Member
Karl Iagnemma	0.20	
FTE Equivalent:	0.20	
Total Number:	1	

Names of Under Graduate students supported

<u>NAME</u>	<u>PERCENT SUPPORTED</u>
FTE Equivalent:	
Total Number:	

Student Metrics

This section only applies to graduating undergraduates supported by this agreement in this reporting period

The number of undergraduates funded by this agreement who graduated during this period: 0.00

The number of undergraduates funded by this agreement who graduated during this period with a degree in science, mathematics, engineering, or technology fields:..... 0.00

The number of undergraduates funded by your agreement who graduated during this period and will continue to pursue a graduate or Ph.D. degree in science, mathematics, engineering, or technology fields:..... 0.00

Number of graduating undergraduates who achieved a 3.5 GPA to 4.0 (4.0 max scale): 0.00

Number of graduating undergraduates funded by a DoD funded Center of Excellence grant for Education, Research and Engineering:..... 0.00

The number of undergraduates funded by your agreement who graduated during this period and intend to work for the Department of Defense 0.00

The number of undergraduates funded by your agreement who graduated during this period and will receive scholarships or fellowships for further studies in science, mathematics, engineering or technology fields: 0.00

Names of Personnel receiving masters degrees

NAME

Total Number:

Names of personnel receiving PhDs

NAME

Total Number:

Names of other research staff

NAME

PERCENT SUPPORTED

FTE Equivalent:

Total Number:

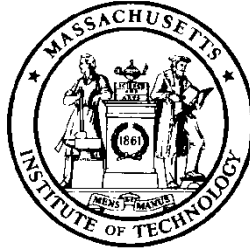
Sub Contractors (DD882)

Inventions (DD882)

Scientific Progress

See Attachment

Technology Transfer



DESIGN AND CONTROL OF OMNIDIRECTIONAL UNMANNED GROUND VEHICLES FOR ROUGH TERRAIN

ARO Award Number: W911NF-09-1-0334

Final Report
July 14, 2009 – August 29, 2012

Prepared for:

U.S. Army Research Office
Terrestrial Sciences Division
P.O. Box 12211
Research Triangle Park, NC 27709-2211

Technical POC:
Dr. Karl Iagnemma
Department of Mechanical Engineering
Massachusetts Institute of Technology
77 Massachusetts Avenue, Room 35-237a
Cambridge, MA 02139
Tel #: 617-452-3262 Fax #: 617-258-5802
Email: kdi@mit.edu

ABSTRACT

Research under this ARO grant has studied the design of highly agile ground vehicles. This has involved work in three related areas. First, research was performed on the design and control of ultra high-performance unmanned ground vehicles (UHP-UGVs) that utilize a new wheel drive system to achieve omnidirectional mobility in rough terrain. The result of this research was an experimental demonstration of a prototype UHP-UGV with measurable agility improvement in rough terrain compared to Ackerman or skid-steered vehicles. Next, research focused on the development of an entirely novel omnidirectional vehicle with anisotropic friction wheels. The wheels are arranged such that the robot wheel exhibits high traction in its driving direction (much like a conventional tire), but low traction when sliding laterally. Exploiting this “anisotropic friction” property, the proposed wheel enables a vehicle to realize omnidirectional motion (i.e. the vehicle can move any direction within the plane—forward, back, or laterally). Finally, research focused on developing novel experimental methods to analyze detailed robot-terrain interaction phenomena, with an ultimate goal of developing models that will lead to improved robot mobility performance.

1 Introduction—Analysis and Design of UHP-UGVs

The first objective of this research was to study the design and control of ultra high-performance unmanned ground vehicles (UHP-UGVs) that utilize a new wheel drive system to achieve omnidirectional mobility in rough terrain. A UHP-UGV would be able to kinematically track non-smooth paths and execute turns with zero radius of curvature. They can also aid mobile manipulation tasks, by allowing the robot base to move with a high degree of precision. Non-smooth, “zig-zagging” behavior might also help a robot evade tracking and targeting by hostile entities. Additionally, the high agility of these systems would allow vehicles to quickly evade obstacles detected at close-range. The result of this research was an experimental demonstration of a prototype UHP-UGV with measurable agility improvement in rough terrain compared to Ackerman or skid-steered vehicles.

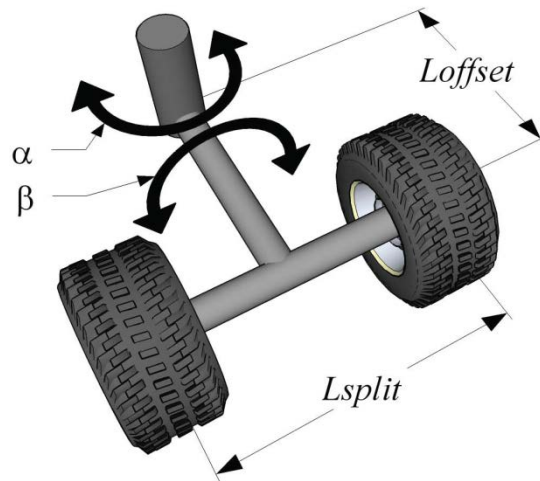


Figure 1: Example of an Active Split Offset Castor (ASOC) drive module.

Previous research in omnidirectional drives has shown that significant agility gains can be derived from these systems [11, 5, 21]. However, omnidirectional drives have generally been applied to robots operating on flat terrain. This is likely due to the fact that most omnidirectional drive systems employ components or mechanisms that are intolerant of dirt, terrain unevenness, or high loads. Thus, they are not well suited to operation in rough terrain. A key aspect of the proposed research is the development of omnidirectional drive systems that are rugged and robust enough for rough terrain operation. The UGVs designed in this research program will employ an omnidirectional drive system based on the Active Split Offset Castor (ASOC), first described in [22] and shown in Figure 1.

The ASOC is composed of two independently powered wheels that are “split” a distance L_{split} from each other and “offset” a distance L_{offset} from an axis, α , which is free to rotate 360 degrees. By driving the wheels at different velocities, the position of an offset mounting point (the “joint”) can be arbitrarily controlled. When two joints are attached to a vehicle, this design allows the vehicle to instantaneously move in any direction or turn in place. Multiple such modules will be used to drive a UHP-UGV.

Unlike most omnidirectional drive designs, ASOC modules use conventional off-road tires. Since multiple driven wheel pairs are employed, the vehicle ground pressure can be minimized and the wheel thrust can be large. The design can easily be coupled with classical suspension designs, has low scrubbing torque compared to other omnidirectional drives that utilize

conventional wheels [22], and can be designed to exhibit favorable control characteristics [19]. The combination of these unique characteristics make the UHP-UGV tolerant of dirt, terrain unevenness, and high loads.

The main focus of the first year research was on continued development of the experimental platforms and the development of advanced control methods. The work accomplished from July 2009 to July 2010 is given below and categorized into five sections:

- Development of soil/tire interaction models for small wheels and low loads to be used in an advanced control algorithm.
- Development of the Omnidirectional UGV (ODV) with a focus on the electrical subsystems and code development.
- Tip-over analysis of the ODV.
- Experimental validation of autonomous feedback control.
- Development of a dynamic model for use in an advanced control algorithm.

Each of the above is discussed in detail below.

2 Soil/Vehicle Interaction Models

One of the goals of the project was to develop control algorithms that take into account the effects of the terrain to improve performance. Initial investigations lead us to realize that in order to develop a control algorithm that incorporates these effects, we needed accurate models of the soil/tire interaction effects. This is especially pertinent to vehicles traversing deformable soils, such as sand, snow, and muskeg. These soils are seldom beneficial to vehicular mobility and never homogeneous. This means that each of a vehicle's wheels/tracks/legs will behave differently, according to the soil beneath it. Vehicle-terrain interaction is not a new area of study, having been applied to large vehicles for decades. However, recent studies have shown that vehicle-terrain theory, known as Bekker theory, is inaccurate when applied to vehicles with wheel diameters less than ~50 cm and normal loading less than ~45 N [4, 15, 16]. This poses a challenge, as these bounds encompass the majority of modern UGVs, including the omnidirectional experimental platform. Thus, we deemed it necessary to improve the fidelity of the wheel-soil interaction models since the ability of a soil to provide traction dictates a large proportion of a vehicle's mobility performance.

This section details work undertaken to improve vehicle-terrain theory and the dynamic modeling of UGVs on deformable soils. Experimental results focus on the pressure-sinkage relationship for sub 50 cm diameter wheels. These results are used in a new pressure-sinkage model. This model is then used to derive new wheel sinkage and compaction resistance equations, the accuracy of which is shown to be significantly improved. It is expected that this model will be used as the basis of a control algorithm that can improve the mobility of the omnidirectional vehicle.

By improving mobility models, we also improve our ability to estimate the real-time state of the wheel-soil interface during vehicle operation. By mapping soil properties to the observed mobility performance of the ODV, it is proposed that the improved mobility models may be included in the ODV's control algorithm. Furthermore, it is believed that if the state of each

ASOC is monitored during operation, ASOCs can operate cooperatively to ensure the best overall traction is developed.

2.1 Vehicle Terrain Theory

We hypothesize that the errors associated with Bekker theory stem from the use of the Bernstein-Goriatchkin pressure-sinkage model. Bekker uses this model in the derivation of both sinkage and compaction resistance equations. The Bernstein-Goriatchkin model for pressure, P , is given as:

$$P = kz^n \quad (1)$$

where k is the sinkage modulus, z is the sinkage and n is the sinkage exponent.

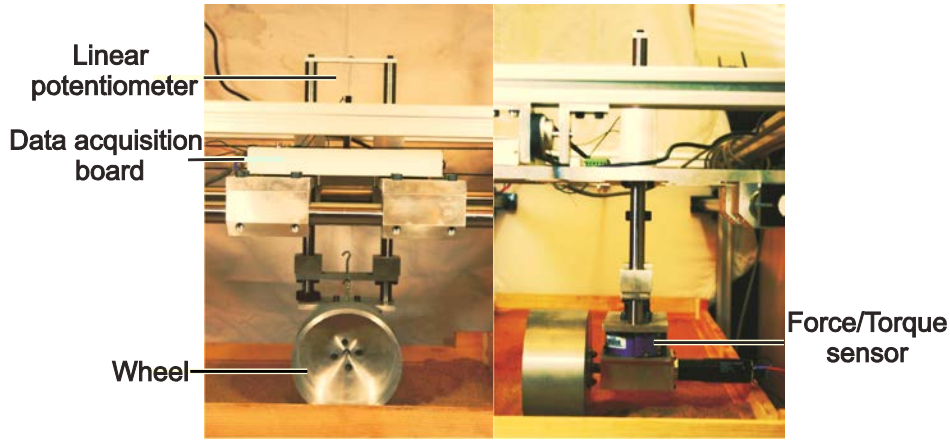


Figure 2: Single-wheel vehicle-terrain testbed.

To reduce the errors associated with small wheel diameters, a modified wheel pressure-sinkage model that is a function of wheel diameter is introduced:

$$P = kz^n D^m \quad (2)$$

where D is the wheel diameter and m is the diameter exponent. The parameter m is a function of soil properties and can be negative or positive. In general, for soft soils (e.g. loose snow), m is negative. This means that as wheel diameter increases, the contact area grows faster than the applied normal force. Conversely, for hard soils (e.g. compacted sand), m is generally positive, which means that as the diameter increases, the normal force increases faster than the contact area.

Substituting the proposed model into Bekker's equations yields a new wheel sinkage equation:

$$z_0 = \frac{3W}{b(3-n)kD^{m+0.5}}^{2/2n+1} \quad (3)$$

and a new compaction resistance equation:

$$R_c = bkD^m \frac{z_0^{n+1}}{n+1} \quad (4)$$

where z_0 is the total wheel sinkage, W is the normal load on the wheel and b is the wheel width.

2.2 Experimental Evaluation of Sinkage Prediction Accuracy

In order to evaluate the accuracy of Bekker's sinkage model when applied to the omnidirectional vehicle's wheels, experiments were performed using a wheel-terrain testbed (see Figure 2). The testbed is instrumented to accurately measure wheel speed, wheel slip, loading, drawbar pull, terrain resistance, and sinkage. Tests were performed on dry sand as detailed in Table 1. These parameters were chosen to match the specifications of the ODV. The wheel was driven with zero slip to ensure that the measured sinkage was not due to rutting. The geotechnical properties of the dry sand, detailed in Table 2, were found from plate sinkage and direct shear tests.

Table 1: Experimental Test Conditions.

Wheel Diameter	Wheel width	Forward velocity	Normal load
$D (m)$	$b (m)$	(cm/s)	$W (N)$
0.17	0.085	10	46 and 84

Table 2: Dry sand physical properties

Cohesion	Friction angle	Sinkage exponent	Sinkage modulus
$C (kPa)$	$\phi (deg)$	n	$k (N/m^{n+2})$
2.05	27.5	0.75	1783

Based on 20 tests, experimental sinkage results were significantly higher than the predicted sinkage values. The results are given in Table 3. Note that the errors yielded by Bekker's model lead to sinkage under-predictions. This means that in the field, the ODV's wheels may exhibit greater sinkage than predicted, which can lead to greater resistances and impaired tractive performance.

Table 3: Errors in predicted sinkage for ODV wheel

Normal load (N)	Sinkage z_0 (% error)
46	27.5
84	33

In summary, the experimental results indicate that significant errors exist when using Bekker's model for small wheel diameters. The next section highlights one potential source of these errors.

2.3 Sinkage and the Flat Plate Approximation

We hypothesize that the aforementioned discrepancy between experimental results and Bekker's sinkage model is a result of a key assumption made by Bekker that does not hold true for small wheel diameters. This section investigates that assumption and its associated limitations when applied to Bekker's sinkage and compaction resistance models.

2.3.1 An Introduction to Bekker's Sinkage and Compaction Resistance Equations

Of the performance metrics Bekker developed, sinkage is perhaps the most fundamental; it is utilized in the derivation of compaction and bulldozing resistances, contact area, thrust, and drawbar pull. To derive a sinkage model for a wheel in deformable soil, Bekker related sinkage to normal pressure through the Bernstein-Goriatchkin equation, which is given in (1). Bekker

expanded k into three constituent parts, k_c (cohesive modulus), k_ϕ (frictional modulus) and b (wheel width).

He also claimed that there existed a linear relationship between k_c and b such that:

$$k = \frac{k_c}{b} + k_\phi \quad (5)$$

Bekker used these parameters in the derivation of his sinkage and compaction resistance equations. Bekker's derivation of the sinkage equation begins by considering wheel normal loading, W :

$$W = -b \int_0^\theta P dx \quad (6)$$

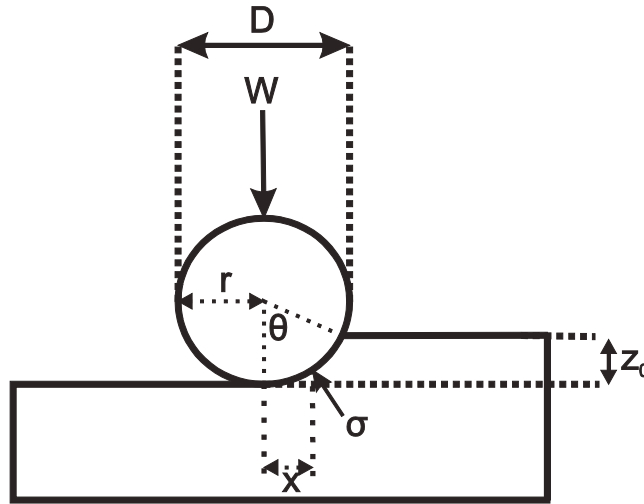


Figure 3: Geometry of the wheel-soil contact region.

which, after substituting in (1) and (5), becomes:

$$W = -b \int_0^\theta \left(\frac{k_c}{b} + k_\phi \right) z_0^n dx \quad (7)$$

where x is the horizontal location of the point of maximum normal pressure for a rolling wheel (See Figure 3). In (7) the pressure term in the integrand is replaced by Bekker's modified Bernstein-Goriatchkin equation. Solving (7) and re-arranging, yields Bekker's relationship for sinkage:

$$z_0 = \frac{3W}{b(3-n)\left(\frac{k_c}{b} + k_\phi\right)\sqrt{D}}^{2/2n+1} \quad (8)$$

Qualitatively, sinkage is expressed as the vertical distance between the undeformed soil surface and the point on the wheel's circumference located directly beneath its centroid.

Compaction resistance is equivalent to the work done on the soil in the vertical direction by a normally loaded wheel. As such, it is highly dependent on the pressure-sinkage relationship. In general, compaction resistance is the largest factor in motion resistance. According to Bekker, compaction resistance is given as:

$$R_c = b \int_0^{z_0} k z^n dz \quad (9)$$

and thus:

$$R_c = bk \frac{z_0^{n+1}}{n+1} \quad (10)$$

2.4 The Flat Plate Assumption

In (8) and (1), wheel sinkage is given only as a function of terrain constants and applied pressure. As such, Bekker's sinkage equation postulates that there is no dependence on wheel diameter. Bekker himself noted this phenomenon:

“Predictions for wheels smaller than 20 inches in diameter become less accurate as wheel diameter decreases, because the sharp curvature of the loading area was neither considered in its entirety nor is it reflected in bevameter tests [3].”

In other words, Bekker indicates that his sinkage equation is appropriate only when the sinkage-to-wheel-diameter ratio is small enough such that the contact patch is approximately flat. It is this approximation that allows Bekker to use the Bernstein-Goriatchkin expression (which is specifically for flat plates) in the derivation of his sinkage equation. This yields a reasonable approximation for large diameter wheels experiencing only modest sinkage. However, the sharp curvature of small wheels cannot be accurately approximated by the flat plate assumption. Investigating the pressure-sinkage dependence on wheel diameter for small wheels is the focus of the following sections.

2.5 The Pressure-Sinkage Relationship

This section details experimental results that demonstrate the need for a pressure-sinkage model that includes both sinkage and wheel diameter, such that $P = f(z, D)$. We hypothesize that the Bernstein-Goriatchkin expression is insufficient for modeling small wheel sinkage because it assumes a constant contact area between the wheel and soil. For the sharp curvature of small diameter wheels, this is not a valid assumption. As a wheel sinks from the surface level to z_0 , the contact area increases.

2.5.1 Experimental Procedure

In order to evaluate the effect of wheel diameter on the pressure-sinkage relationship, tests were conducted using multiple wheel diameters and soils. In total, 160 pressure-sinkage tests were performed. Five wheel diameters were used, ranging from 0.1 m to 0.3 m. This range encapsulates the ODV and the majority of wheels used on modern UGVs [2, 7, 9, 12, 17]. The physical properties of the three soils chosen for testing are detailed in Table 4.

Table 4: Physical properties of test soils.

Property	Dry Sand	Calcium silicate	Moist earth
Cohesion, C (kPa)	2.05	3.08	3.13
Friction angle, ϕ (deg)	27.2	32.2	34.0

To perform the experiments, a custom-built pressure-sinkage testbed (shown in Figure 4) was used. The testbed is instrumented with a JR³ 90M40A 6-axis force/torque sensor, linear actuator and potentiometer. The linear actuator provides up to 50 mm of sinkage. The normal load was limited to <450 N. Note that the low normal loading condition discussed in Section 1 is a separate area of study from the tests detailed here; in this instance, we are only investigating the effect of small wheel diameters. Force and sinkage were measured using the force/torque

sensor and linear potentiometer. Required soil bin dimensions were calculated using Terzaghi's bearing capacity theory for shallow foundations [18]. This is necessary to ensure that the soil bin walls do not interfere with the stress distributions beneath the loaded wheel section.

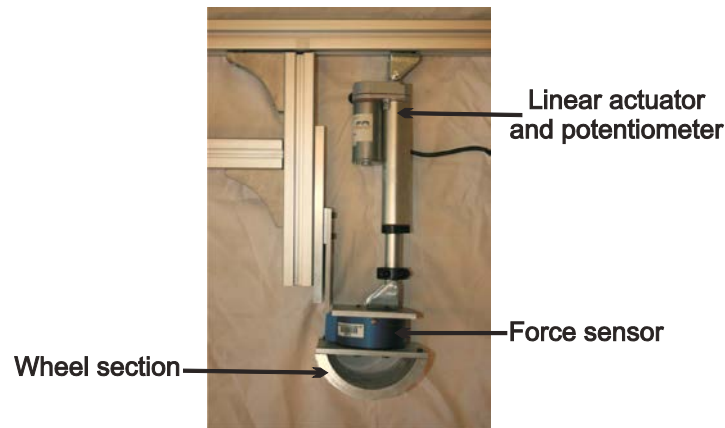


Figure 4: Pressure-Sinkage testbed.

2.6 Results

Figures 5, 6, and 7 show experimental results for each wheel diameter and soil. Each figure represents one soil, within which each line represents one diameter.

Figure 5 shows the results for dry sand. The curves exhibit a clear dependence on wheel diameter. As the diameter increases, so does the observed pressure. This implies that as the wheel diameter increases, the force required to attain a given level of sinkage increases faster than the contact area.

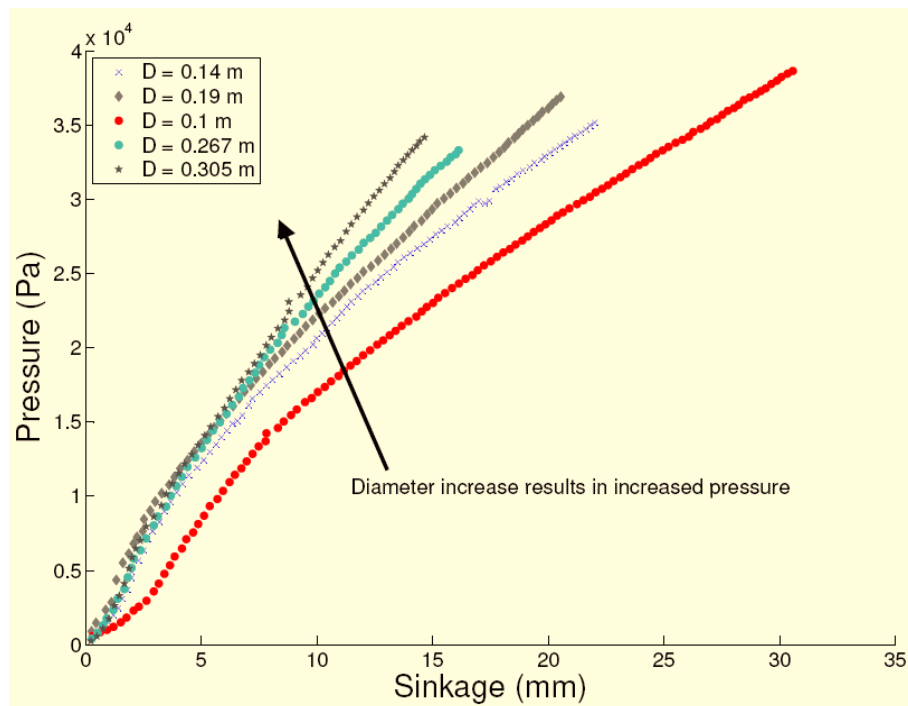


Figure 5: Pressure-Sinkage results for dry sand.

Figure 6 shows the results for calcium silicate. Calcium silicate is a fine powder and exhibits an almost fluid-like behavior. The force required to achieve total sinkage in this case was around one tenth of that for dry sand. The consequence of this low force is that the overall change in pressure as a function of wheel diameter is very low. This is represented in Figure 6 where the pressure-sinkage relationship exhibits negligible dependence on wheel diameter.

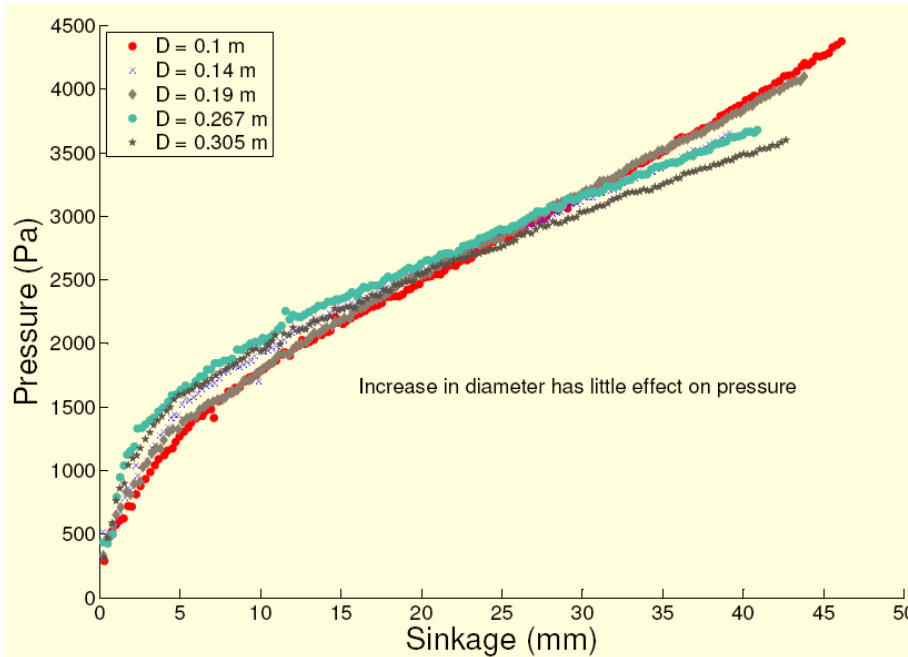


Figure 6: Pressure-Sinkage results for calcium silicate.

Figure 7 shows the results for moist earth. The soil moisture content was kept near-constant by performing the tests indoors over two consecutive days. As with dry sand, the results show a large dependence on wheel diameter. However, in this case, as the wheel diameter increases, the pressure decreases. This implies that for moist earth, as the wheel diameter increases, the contact area increases faster than the force. This is the opposite effect than that of dry sand.

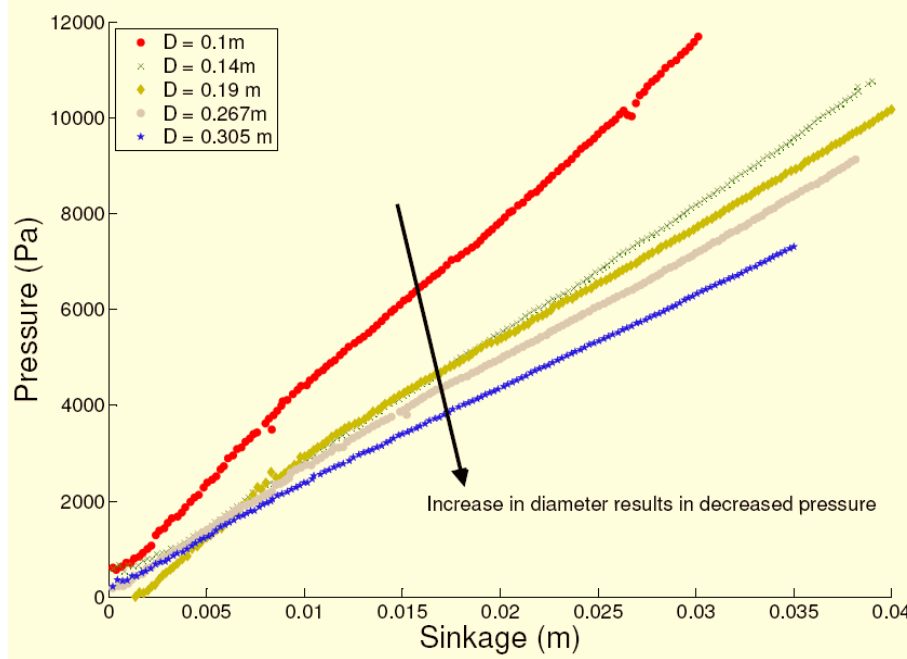


Figure 7: Pressure-Sinkage results for moist earth.

What is evident in both the dry sand and moist earth results is that a change in wheel diameter has a definite effect. Furthermore, it is clear that this effect manifests itself as a change in the curvature of the pressure-sinkage relationship.

2.7 A New Pressure-Sinkage Model

Based on the results of the aforementioned experimental tests, a new model is proposed to account for the dependence on wheel diameter:

$$P = kz^n D^m \quad (11)$$

where D is the wheel diameter and m is the diameter exponent that describes the degree of influence the diameter has on the pressure for a given soil. Much like the Bernstein-Goriatchkin equation, the proposed model describes a power curve for which k , n and m are fitting constants. The improvement in the proposed model stems from the inclusion of D^m , which ensures that the curvature of the pressure-sinkage relationship is a function of both sinkage and diameter. The constants k , n and m found for each of the soils tested are shown in Figure 5. Note that the parameter, m , can be negative. This occurs in loose soils when the wheel-soil contact area grows faster than the applied force.

Table 5: Proposed model soil properties.

	Dry Sand	Calcium silicate	Moist earth
$k \text{ (kN/m}^{n+2}\text{)}$	1604	16.7	78.8
n	0.8	0.48	0.88
m	0.39	0.00	-0.49

Figure 8 shows an example of the improvement in the pressure-sinkage model when using (11) as opposed to the Bernstein-Goriatchkin equation. Results are shown for the smallest and

largest wheel diameters tested. Again, the single pressure-sinkage curve offered by the Bernstein-Goriatchkin expression is insufficient when dealing with varying wheel diameters. We also see that the proposed model yields significantly more accurate results in both cases. This was found to be true for all the tested wheel diameters and soils. The improvement is further exemplified for all soils in Figures 9, 10 and 11, which compare the root mean squared error (RMSE) of pressure-sinkage predictions using both the Bernstein-Goriatchkin and proposed models. All three figures demonstrate a significant improvement over a wide range of wheel diameters when using the new model proposed here.

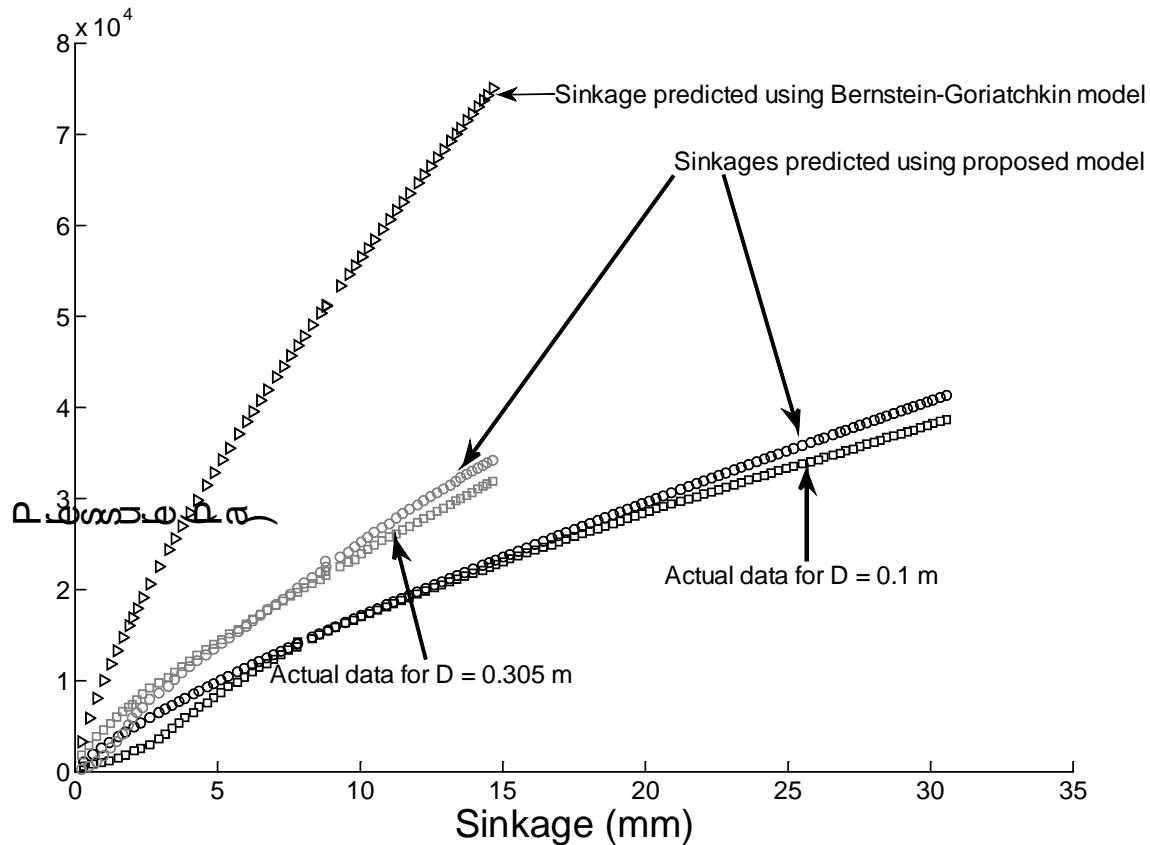


Figure 8: Comparison of Bernstein-Goriatchkin and proposed model on dry sand.

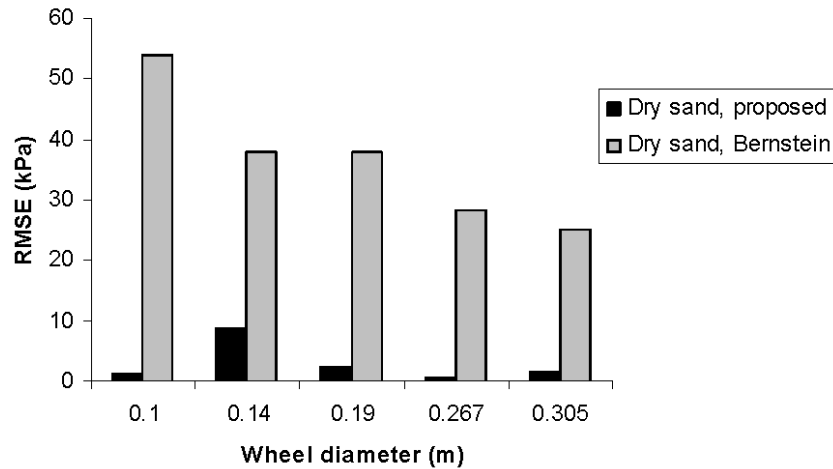


Figure 9: Comparison of root mean square error values using the Bernstein-Goriatchkin equation and the new proposed model for dry sand.

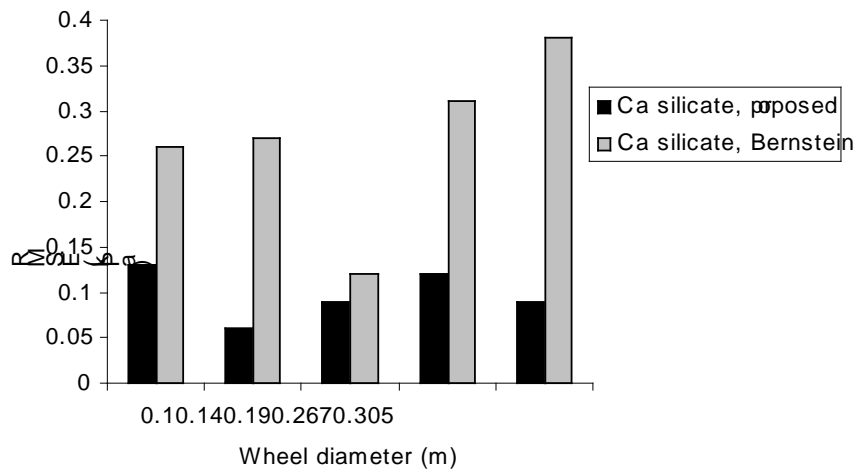


Figure 10: Comparison of root mean square error values using the Bernstein-Goriatchkin equation and the new proposed model for calcium silicate.

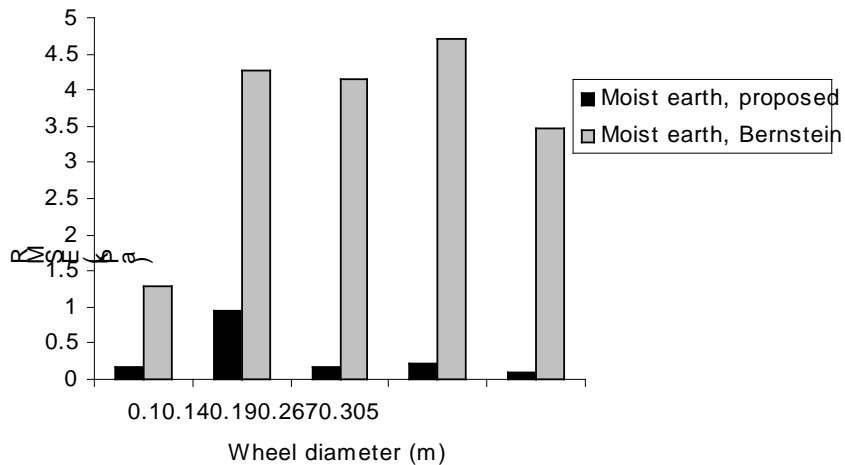


Figure 11: Comparison of root mean square error values using the Bernstein-Goriatchkin equation and the new proposed model for moist earth.

2.7.1 Updating the Sinkage and Compaction Resistance Models

Using (11) and the geometry shown in Figure 3, new models for sinkage and compaction resistance are derived. For sinkage, the wheel normal loading is given as:

$$W = -b \int_0^{\theta} \sigma r \cos \theta d\theta \quad (12)$$

where σ is the normal pressure over the contact patch and r is the wheel radius. Substituting in the new pressure-sinkage model yields:

$$W = -b \int_0^{\theta} k z^n D^m dx \quad (13)$$

where P is the pressure and the integrand of (12) has been replaced in (13) by use of the proposed pressure-sinkage model. Solving (13), we obtain:

$$W = \frac{bkD^{m+0.5}}{3} z^{n+0.5} (3-n) \quad (14)$$

which, after rearranging for sinkage, becomes:

$$z_0 = \frac{3W}{b(3-n)kD^{m+0.5}}^{2/2n+1} \quad (15)$$

Similarly, from the geometry of Figure 3, the compaction resistance is:

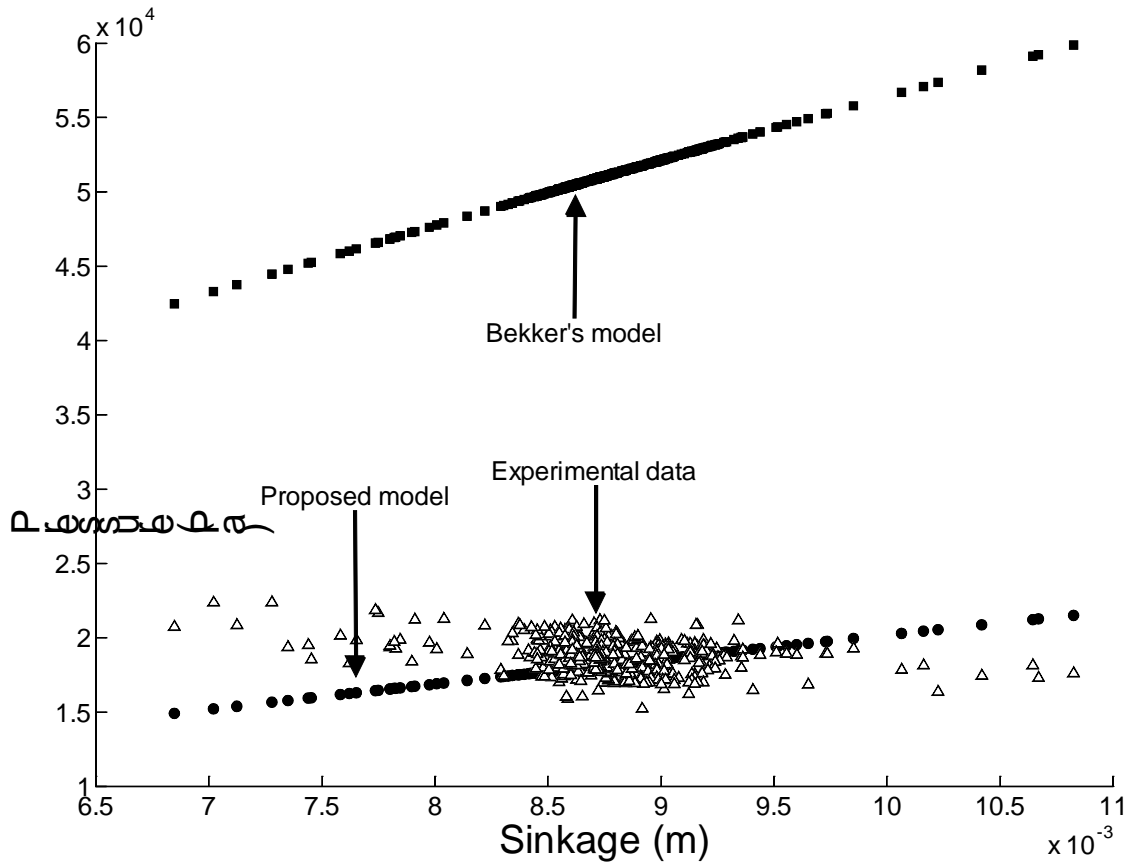
$$R_c = b \int_0^{\theta} \sigma r \sin \theta d\theta \quad (16)$$

which, using the proposed pressure-sinkage model, may be expressed as:

$$R_c = b \int_0^{z_0} k z^n D^m dz \quad (18)$$

2.7.2 Validation of the Proposed Model for the Rolling ODV Wheel

To validate the new sinkage and compaction resistance models, experiments using the vehicle terrain testbed shown in Figure 2 were conducted. The tests utilized the ODV's wheel under the conditions given in Table 1. These tests were performed to validate the derivation of the sinkage and compaction resistance equations shown in Section 6.1. The results for wheel pressure as a function of sinkage are shown in Figure 12. Bekker's equation clearly over-estimates the pressure required to achieve the experimentally found level of sinkage. The proposed model, however, adheres to the pressure-sinkage data with good accuracy.



Figure

12: Comparison of experimental sinkage data fit with Bekker and proposed models.

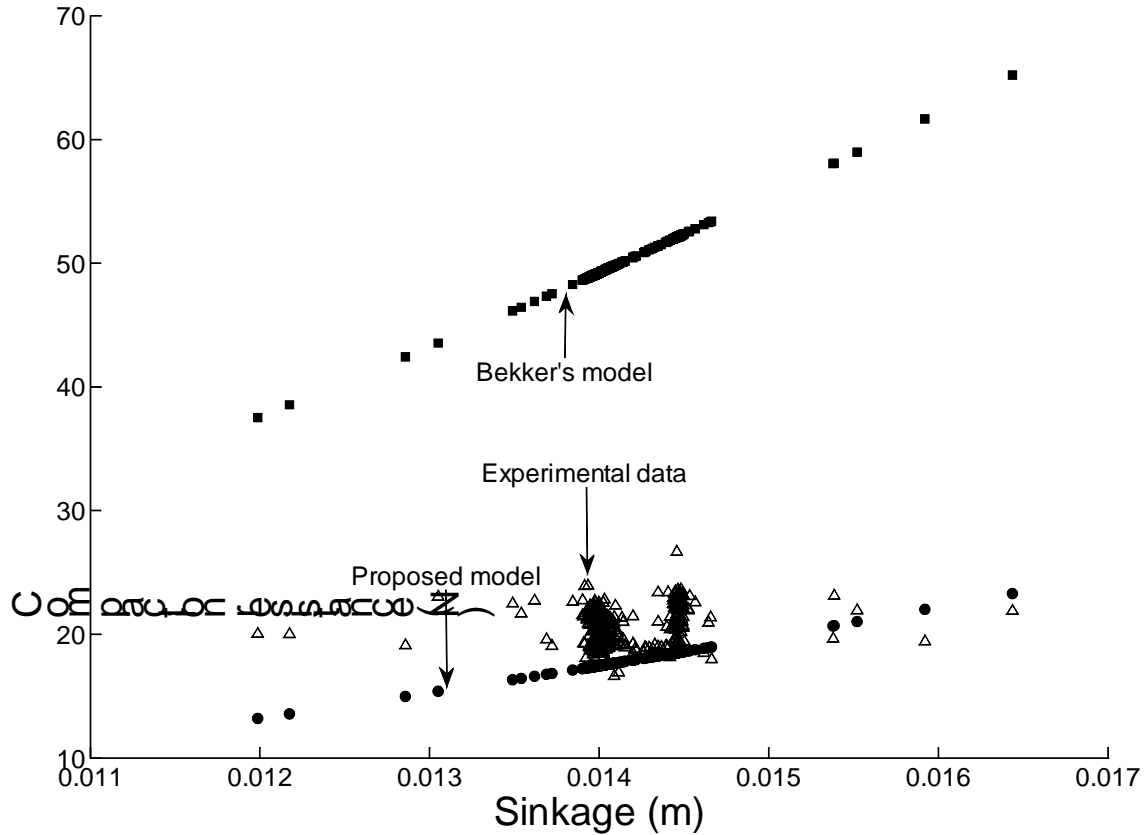


Figure 13: Comparison of experimental compaction resistance data fit with Bekker and proposed models.

For compaction resistance, tests were performed by measuring the motion resistance while towing the wheel under the conditions given in Table 1. Results are shown in Figure 13, which show that Bekker's equation significantly over-estimates the resistance. Again, the proposed model reduces the error substantially. A slight under-estimation of resistance by the proposed model is observed. This is attributed to a small amount of un-modeled bulldozing resistance.

Table 6 summarizes and compares the accuracy of the proposed model versus Bekker's model for the above tests.

Table 6: Accuracy comparison for Bekker and new models.

	Experimental	Bekker	Proposed	Improvement
z_0 (mm)	8.8	5.2	9.8	3.6x
R_c (N)	20.8	50.6	17.9	10x

2.8 Application of the Proposed Model to the ODV

To understand the benefit of applying the wheel-terrain model to the ODV, consider the scenario of the vehicle traversing undulating, sandy terrain, as may be experienced in a desert or arid region. The physical properties of the soil is known through basic tests. Mapping these soil properties and the ODV's geometry to the wheel-soil model, we may ascertain the expected wheel-soil interface pressure and thus sinkage. Furthermore, we can use this sinkage to calculate the expected soil resistances and maximum obtainable traction. With these parameters in mind,

metrics such as maximum scalable incline, maximum surmountable object, acceleration and traction as a function of slip can be determined. These metrics may be used for the real-time path planning and control of the vehicle.

If proprioceptive sensors are used to monitor slip, pitch, roll and wheel torque, it can be determined how efficiently the vehicle is generating traction from the soil. From this, the wheel motors can be controlled in a more efficient manner. Additionally, cooperative control between ASOCS may be established, whereby each ASOC receives feedback on the other ASOCs' performance. Thus, if ASOC w is experiencing a high level of slip, which may lead to rutting and increased resistance, ASOCs x , y and z can compensate for this loss in traction.

2.9 Concluding Remarks and Related Future Work

This section outlined the inaccuracy of Bekker's wheel-soil model when applied to the ODV. Experimental results from 160 tests have been used to validate a new pressure-sinkage model, which has been subsequently shown to improve the accuracy of sinkage and compaction resistance models.

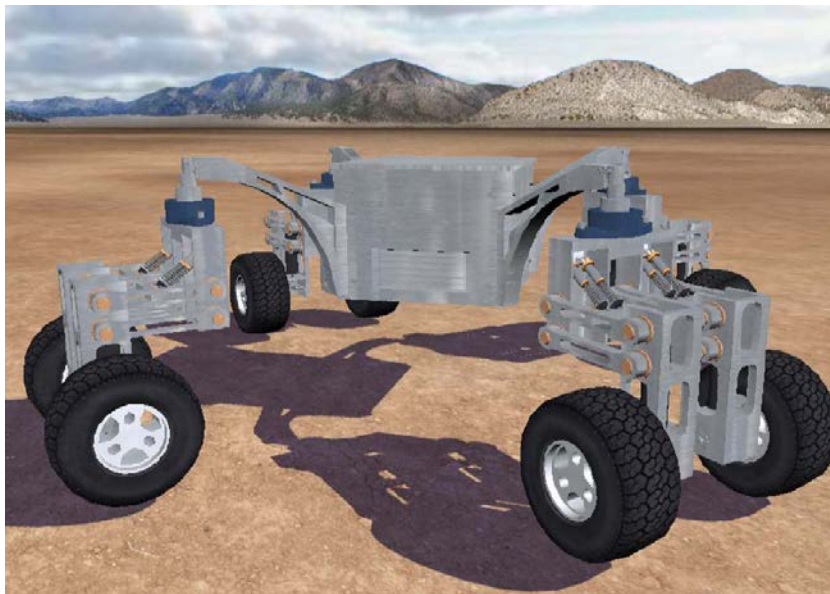


Figure 14: The ODV inside the ANVEL test simulation.

A vehicle-terrain simulation of the ODV is currently being developed in cooperation with the software development company, Quantum Signal. This rigid body dynamics simulation, housed within the Autonomous Navigation and Virtual Environment Laboratory (ANVEL) software, will allow the simulation of the ODV's mobility over a variety of terrains. Crucially, the mobility model used is configurable to obey either Bekker's or the IIT proposed model. A snap-shot of the ODV in the ANVEL test environment is shown in Figure 14. Following completion of the simulation software, simulation results will be compared with real-world experiments performed with the ODV. If the simulation and experimental results confirm the accuracy of the proposed wheel-terrain model when applied to the ODV, this model will be utilized to optimize the operation and control of the ODV over deformable terrains.

3 Development of the Omnidirectional UGV

This section details the ongoing development of the omnidirectional platform. The majority of the work focused on developing the electronics and software for the vehicle and included several key advances that will allow for the execution of multiple experimental trials.

3.1 Electronics

This section outlines the design of the ODV's embedded electronic circuit boards and its associated code. The circuit boards are necessary because of the nature of the ASOCs, which require the ability to rotate more than 360°. This requires either the use of mechanical slip rings (disregarded due to cost and reliability issues) or ASOCs that house their own power supplies and communicate wirelessly to a central on-board computer. An overview of the central controller located on the on-board computer is also discussed. The two possible methods to design the software architecture are discussed below.

1. Compute the ASOC wheels' velocity commands on the embedded microcontroller located on each ASOC. This solution has the advantage that few data transmissions between the central on-board computer and the ASOCs need to occur. However, it requires the ASOC's microcontroller (a MicroChip PIC) to perform numerous computations. This solution was initially implemented but ultimately rejected because the computation capabilities of the PIC micro controller were not fast enough to compute the wheels' desired velocity in real time.

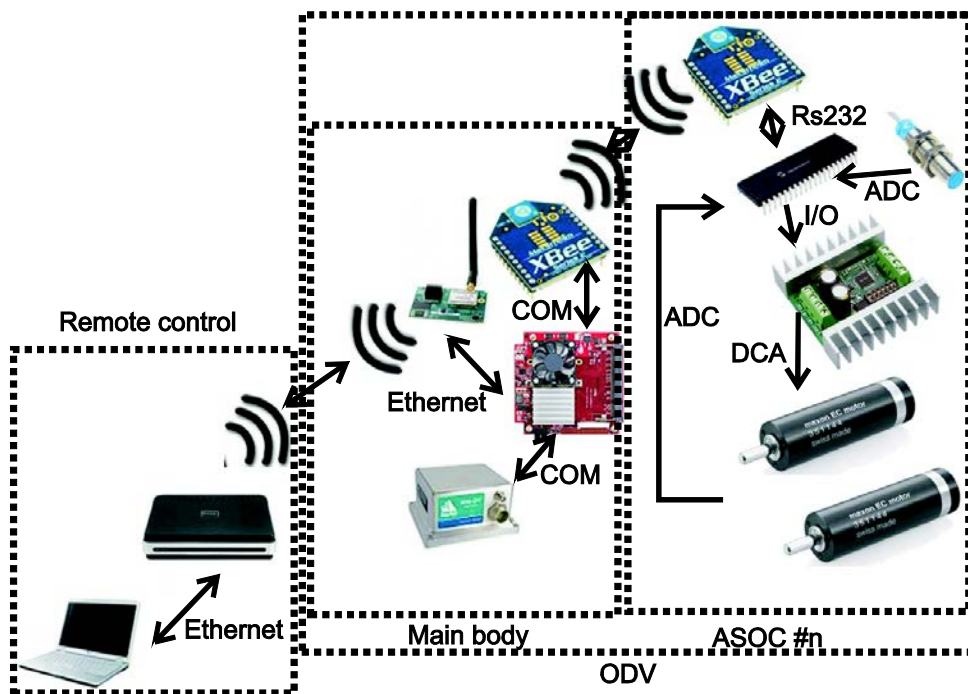


Figure 15: General electronics architecture.

2. Compute the wheels' velocity on the central on-board computer and transmit the data to the electronics board. The electronics board will thus be used only to perform a low level feedback control of the wheels. This solution was ultimately implemented and yielded good results.

The architecture of the second solution is shown in Figure 15. The electronics architecture is segmented into three parts. The first is the remote laptop, by which the user can send commands to the vehicle. The second is the on-board computer, connected through an Ethernet

port to the remote laptop. This on-board computer is used to process the data coming from the GPS/INS system as well as the user commands. The last part is the electronics board on every ASOC, built around a PIC micro controller, that is connected to the on-board computer with XBee modules. Figure 15 illustrates this setup.

A XBee module is used to transmit and receive data between each ASOC module and the central on-board computer. The data frame in API mode is a different from other serial transmission protocols. It is divided into a header, the data, and a checksum. When data are transmitted, the checksum must be computed and added to the data, however, when data are received, the module will check the checksum by itself and release the data only if it is coherent with the emitted data. Figure 16 illustrates the data frame for emitted data, and Figure 17 illustrates the received data frame.

On both data frames, the start bit (bit 0 in the Header) is set by the user. Checking this bit ensures that the data arriving on the serial port is coming from the correct XBee. Bits 5 and 6 in the Header define the address of the Xbee. Table 7 summarizes the important configuration settings.

0x7E,0x00,0x08,0x01,0x00,0x50,0x00,0x01	0x00,0x00,0x00	0x00
Header	Data	Checksum

Figure 16: Transmitted data from the on-board computer to the PIC. The start bit, 0x7E, is set by the user.

0x7E,0x00,0x08,0x01,0x00,0x50,0x00,0x01	0x00,0x00	0x00
Header	Data	Checksum

Figure 17: Received data from the PIC to the on-board computer.

Table 7: Main Xbee settings.

Item	Value
Baud rate	38400bps
ASOC's XBee Address	5001 to 5004 (16bits)
Main body's Xbee Address	5000 (16bits)
Data frame length from Computer to ASOC	9 bytes
Data frame length from ASOC to Computer	12 bytes

3.1.1 Main Electronics Board

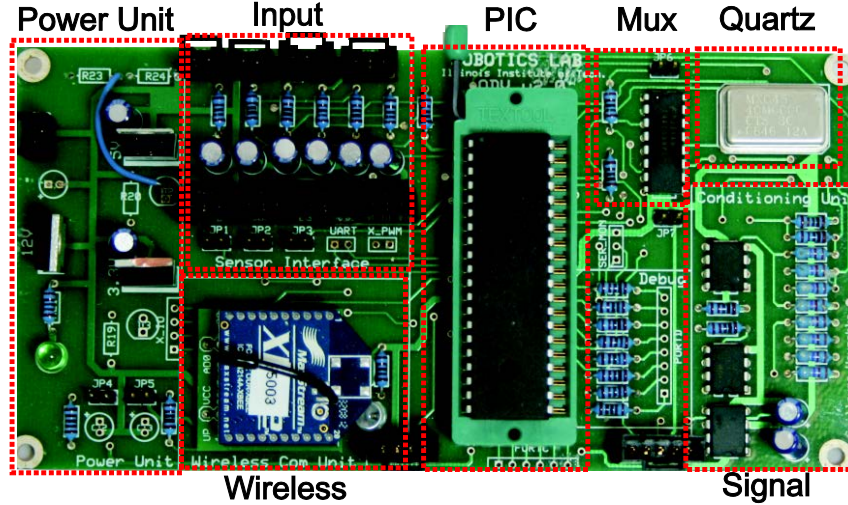


Figure 18 illustrates the ASOC's electronics board, which is split into four sections: power management, signal amplification, wireless communication, and the microcontroller.

Power Management Four different voltage levels are needed to supply the electronics. Three DC to DC converters and one voltage converter are used to create them. Figure 19 illustrates the voltage conversion setup.

The main input power comes directly from the battery, which delivers 22.2 V as required by the motors. That voltage is converted to 12 V through the first converter. The resulting 12V is used as a reference voltage to create -12, +5 and +3.3V. These converters have been sized so they can fulfill the power requirements for all the components, which are given in Table 8.

Signal Conditioning Each motor is equipped with a tachometer that delivers a voltage ranging from -5V for full reverse speed to +5V for full straightforward speed. The ADC of the PIC has a full scale of 5 Volts. In order to obtain the best resolution, the signal has to fit to this range. Thus, the signal amplifier unit needs to rescale the signal. The resolution will thus be divided by two, but it will allow full range feedback from the motor. The schematic of the operational amplifier and its circuit is shown in Figure 20. Equation 19 gives the equation between the output and the input of the circuit. With appropriate resistors, we can switch the output voltage to the desired scale (see Eq. 20).

$$AN_0 = \frac{\left(\frac{R_4}{R_3} + 1\right) \left(\frac{5}{R_1} + \frac{TAC_1}{R_2}\right)}{\left(\frac{1}{R_6} + \frac{1}{R_5}\right) \left(\frac{1}{R_1} + \frac{1}{R_2}\right) R_5} \quad (19)$$

Table 8: Voltage and current consumption of the ASOC electronics components.

Component	Voltage (Volt)	Current (mAmps)
PIC 18F4431	5	200 (max)
XBee	3.3	40 (max)
Demultiplexer	5	negligible
Operational Amplifier	12/-12	negligible

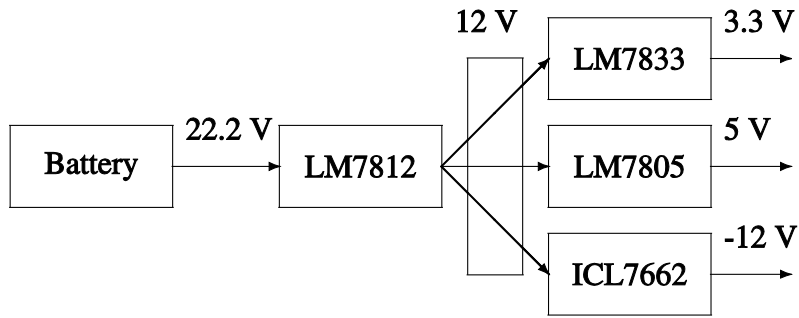


Figure 19: Voltage regulator setup.

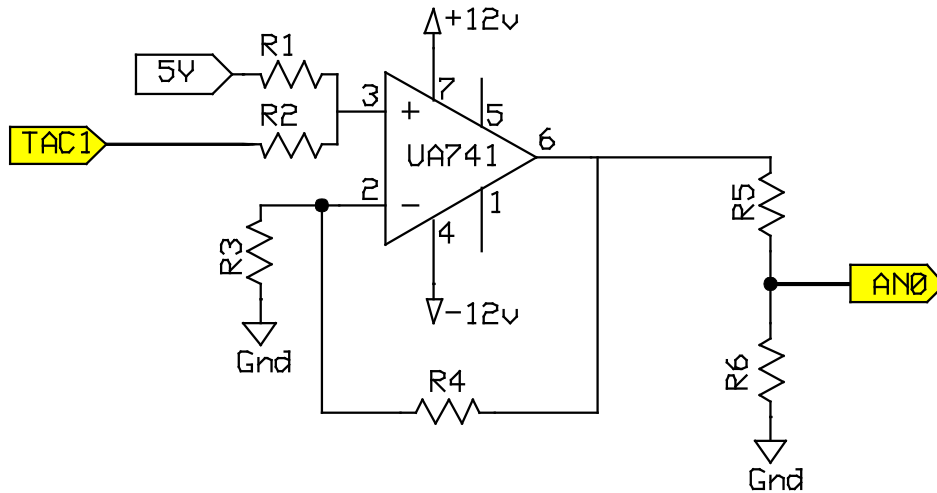


Figure 20: Amplifier circuit.



Figure 21: The motor driver used for each ASOC.

If $R1 = R2 = R3$ and $R4 = R5 = R6$, the desired gain is obtained and the output voltage will be scaled between 0 and 5 Volts as:

$$AN_0 = \frac{5 + TAC_1}{2} \quad (20)$$

Wireless Communication Wireless communication is provided through a Xbee microchip. In its simplest configuration mode, only four pins need to be connected on the Xbee, +3.3V, Ground, Rx (receive) and Tx (transmit). These two pins are connected to the PIC through a demultiplexer. The demultiplexer allows the PIC micro controller to connect more than one peripheral on the same serial port. **Microcontroller** The microcontroller acquires the data from the sensor on its

ADC channels ADC0, ADC1, and ADC2 and receives and transmits data to the Xbee and to the motor driver through the serial port (via the demultiplexer).

3.1.2 Motor Driver

The ASOC's motors are driven by a motor driver (see Figure 21). For the UGV, the driver runs in the packetized serial mode. This mode uses multi-byte serial commands to set the motor speed and its direction. It is a one direction only interface, which means that there is no feedback coming from the motor driver to the PIC. Because different motor drivers can be plugged on the same line, an address has to be assigned to the driver. Each motor velocity is coded on 7 bits, and an extra byte is used to determine the command mode. There are four different commands: 1) Drive motor 1 forward, 2) Drive motor 1 backward, 3) Drive motor 2 forward, and 4) Drive motor 2 backward.

3.2 Microcontroller Code

The code used to drive the ASOCs is written in C using MPLab. The full code can be found in Appendix C. A simplified version of the code is presented in Figure 22. To reduce complex arithmetic involving sines and cosines from the PIC, the computations to calculate motor velocity are performed on the on-board computer. Therefore, the PIC only computes a low level PID control signal for wheel velocity. A serial interruption is used to receive the data coming from the XBee and to send the sensors' data back. The interrupt's program outline is presented in Figure 23.

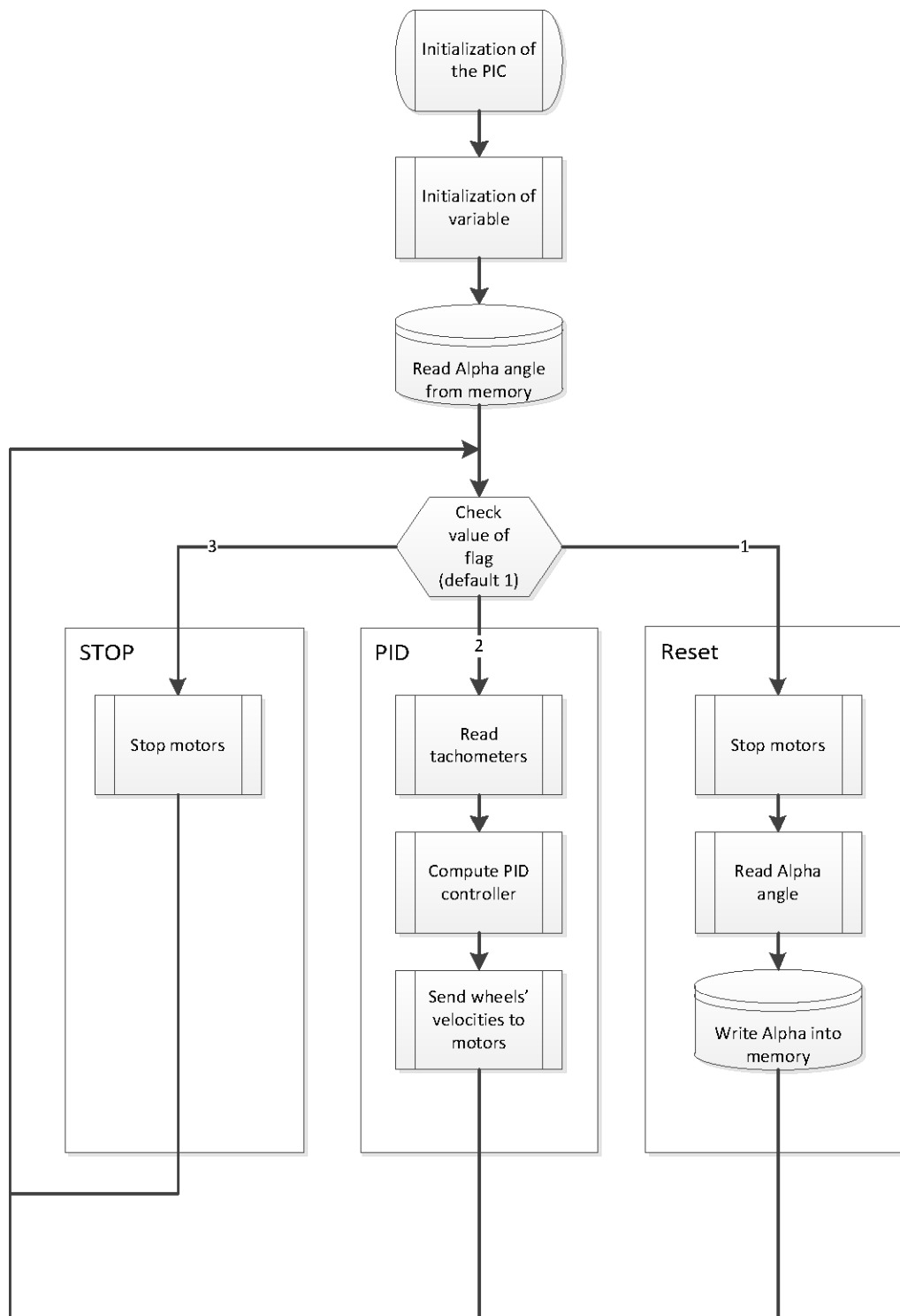


Figure 22: PIC main code.

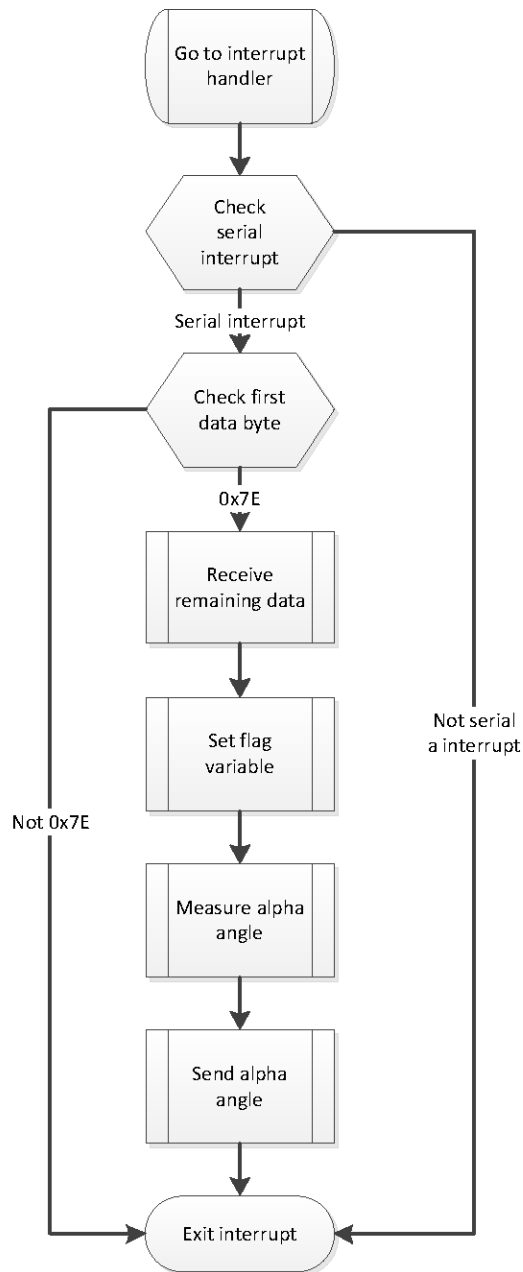


Figure 23: PIC interrupt code.

3.3 Central Body Embedded Electronics

As described above, the ASOC is only responsible for the low level control of the wheels' velocities. The ASOCs receive the desired velocities from the on-board computer located on the main body of the vehicle. This section describes how the on-board electronics works. The outline of the code is presented as is how to configure the GPS/INS system. A brief introduction to QNX, the real-time operating system used on the UGV, is also presented.

3.3.1 On-board Computer Utilization

The on-board computer is a Versallogic PC104 "Cheetah" equipped with a 1GHz CPU, 2USB ports, 2COM ports, a 4GB compact flash hard drive and 1GB of RAM. It is recognized that

these specifications are well beyond what is necessary to operate the vehicle; however, the computer is well equipped to address any expansion needs that may arise. The PC104 computer runs the micro-kernel, real time QNX neutrino operating system. A windows software, Phindows, is used to connect and take remote control of the computer. The program can therefore be launched from a distant laptop. Basic commands on how to operate Phindows and QNX are given in Appendix D.

3.3.2 Code Algorithm

The on-board computer is responsible for receiving data coming from the IMU system, the angles from each ASOC optical encoder, and computing the wheels' velocities accordingly to the desired path and the actual location. Figure 24 presents the pseudo-code used in the on-board computer.

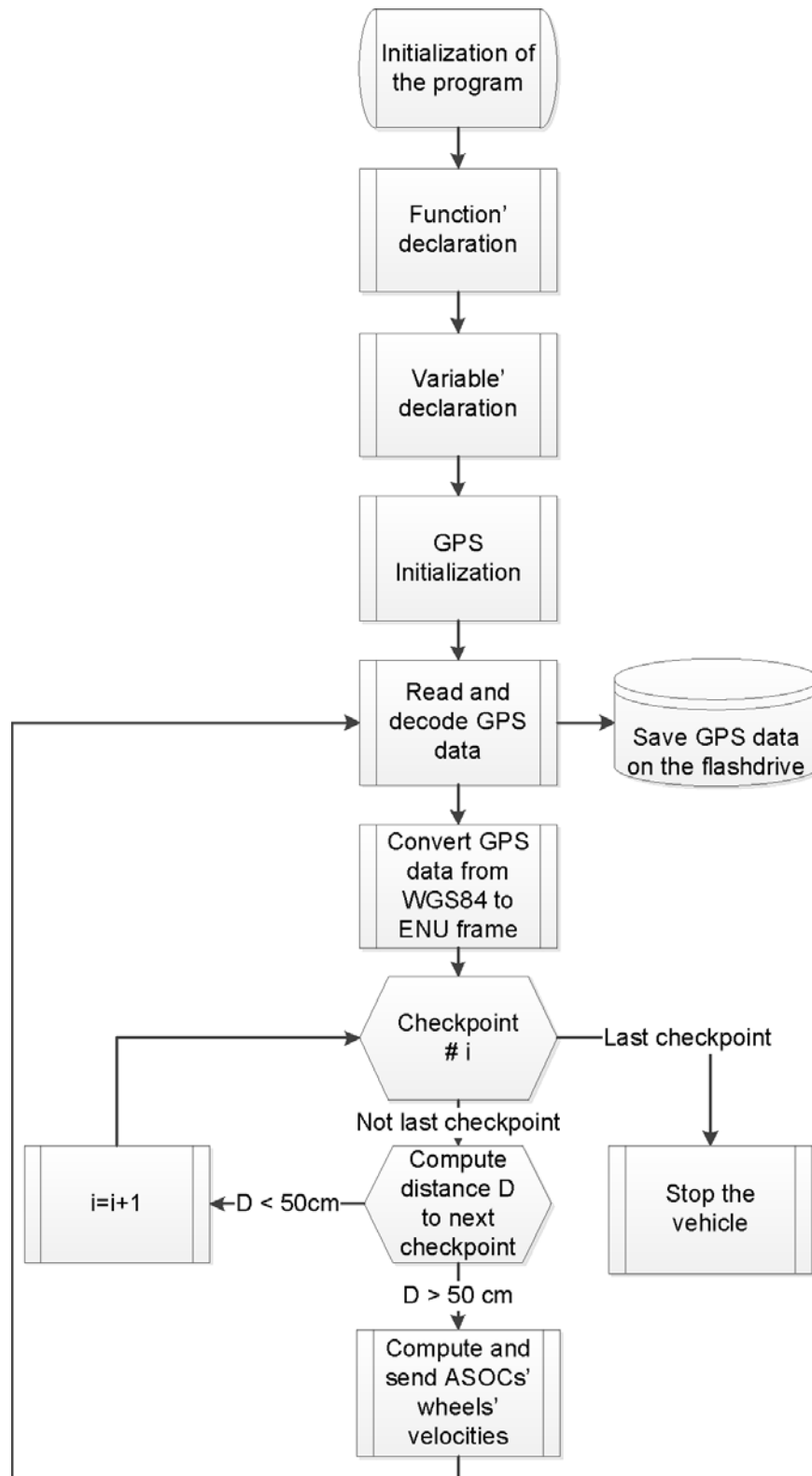


Figure 24: Main code outline.

3.3.3 GPS Configuration

The GPS/INS is a receiver “Span-CPT” from Novatel. The system mounted on the rover outputs different data frames that can be chosen as a function of the needs. The following parameters are needed for the computation of the wheels’ velocity:

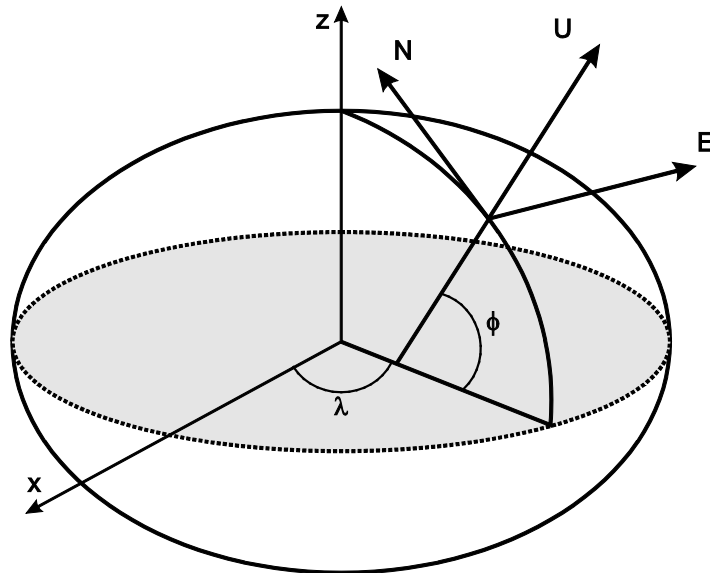


Figure 25: East-North-Up (ENU) coordinate system [13].

The log INSPVAS (INS Position, Velocity, Attitude, Short header) has been chosen. It provides the previously listed parameters, as well as the north, east and up velocities and the roll and pitch angles. Before being able to output this log, the IMU needs to be configured. The baud rate and the frequency have to be set, and the initial parameters of the IMU (antenna offset and initial orientation) also have to be set.

Once the GPS is set, it will output the data at a constant frequency until an “unlog” command is sent. It is then necessary to convert the position data given in terms of latitude, longitude and altitude (WGS84 geodetic coordinates) in a local coordinate frame. This local coordinate frame is called “ENU” (for East North Up) and is defined as follows:

1. X-axis is created pointing East
2. Y-axis is created pointing North (perpendicular to the X-axis)
3. Z-axis is created following the right hand rule, and is therefore pointing up.

Figure 25 illustrates the East-North-Up coordinate system. It is important to note that the ENU coordinates are expressed in meters whereas the geodetic WGS84 coordinates are in degrees.

3.4 Communication procedure

As discussed above, the on-board computer receives data from each ASOC, computes the wheels’ velocities, and sends the commanded velocities to the ASOCs. Figure 26 illustrates this procedure, which is to be interpreted along with Figure 23, which illustrates the PIC interrupt process.

3.5 Concluding Remarks

This section detailed the ongoing progress to developing the experimental ODV platform. The focus was on developing the electronics hardware and the associated software needed for autonomous control of the vehicle.

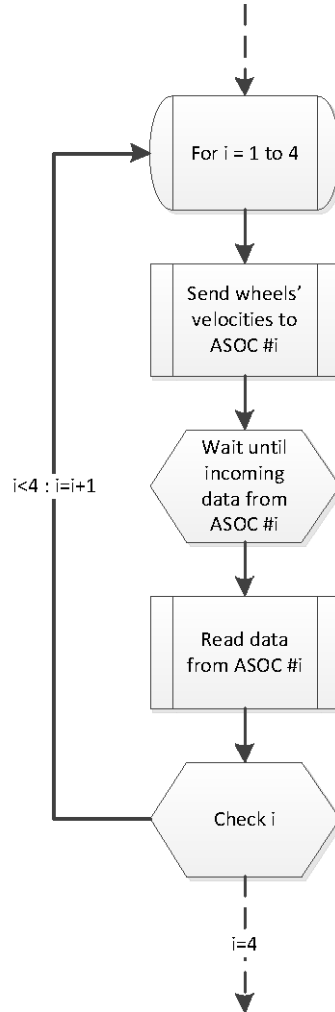


Figure 26: Communication procedure on the on-board computer.

4 Stability Analysis on Inclined Terrain

This section outlines the stability analysis of the experimental vehicle. The focus is on determining the bounds on slip and tip-over and understanding whether or not these bounds are affected by UGV's kinematic configuration and direction of travel.

4.1 Slip Analysis

A basic static analysis determined the relationship between the coefficient of friction, μ , and the maximum slip angle, ψ :

$$-\sin(\Psi) + \mu * \cos(\Psi) \geq 0 \quad (21)$$

Common values for the traction coefficient, μ , are between 0.6 and 1.2. Using the relationship shown above, the maximum incline angle is about 50. This value is in agreement with an experimentally procured value of 47 degrees.

4.2 Tip-over Analysis

A tip-over analysis was also performed to determine whether the UGV will tip-over before sliding occurs, and if so, whether there is a preferred direction of travel that can minimize this occurrence. The analysis also yields information regarding the maximum terrain inclination angles. The tipover analysis was performed using the force-angle measurement method first described in [14].

This is a full three-dimensional analysis assessing when tip-over will occur for a given vehicle based on several factors, including the height of the UGV's center of mass and terrain inclination. A brief introduction to this analysis is presented first. A tip-over (or rollover) is said to occur when "a nominally upright vehicle body undergoes a rotation which results in a reduction of the number of ground contact points such that all remaining points lie on a single line (the tip-over axis)" [14]. Since the ASOCs are free to rotate 360 degrees, its convex contact polygon, or the convex polygon formed by the contact points between the wheels and the terrain, differ depending on the UGV's heading angle (see Figure 27). Each wheel is modeled as a contact point of the vehicle with the ground. Note that in the case where $\theta = 0$, two of the wheels lie within the convex polygon and are therefore not considered as a vertex of the polygon.

Tip-over occurs when the direction of vector sum of all the external forces acting on the UGV's center of mass that lies outside of the convex contact polygon. This instance takes place when, α_t , the tip-over stability metric is less than or equal to zero:

$$\alpha_t = (\Theta_i)_{\min} \|f_r\| \quad (22)$$

where $\|f_r\|$ is the sum of all external forces acting on the center of mass and θ is the angle between $\|f_r\|$ and the vector pointed from the center of mass to the line that connects two vertices of the convex contact polygon. If $\alpha_t > 0$ then the UGV is stable. If $\alpha_t < 0$ then the UGV is in the process of tip over.

For the omnidirectional UGV described here, two simplifications were made:

1. Due to the relatively low UGV velocity and acceleration, inertial forces were neglected. Thus, the only force acting on the OGV is its weight.
2. The contact point between the wheel and the ground is always assumed to lie directly below the wheel's center. It is noted that the UGV may operate on rough terrain, and that this assumption will not always be valid; however, the differences in the final results are expected to be minimal.

As an omnidirectional vehicle, the vehicle does not have any preferential direction, thus, the analysis was performed for a set of values of θ (see Figure 27 for a definition of θ) ranging from 0 to 90 degrees. Figure 28 shows the result of this analysis.

It is clear from the plot that there exist multiple stable orientations. This is especially true when the angle θ is equal to 0 or 90 degrees. But since the maximum climbable incline is 47 degrees, the UGV will experience sideslip well before tip-over occurs.

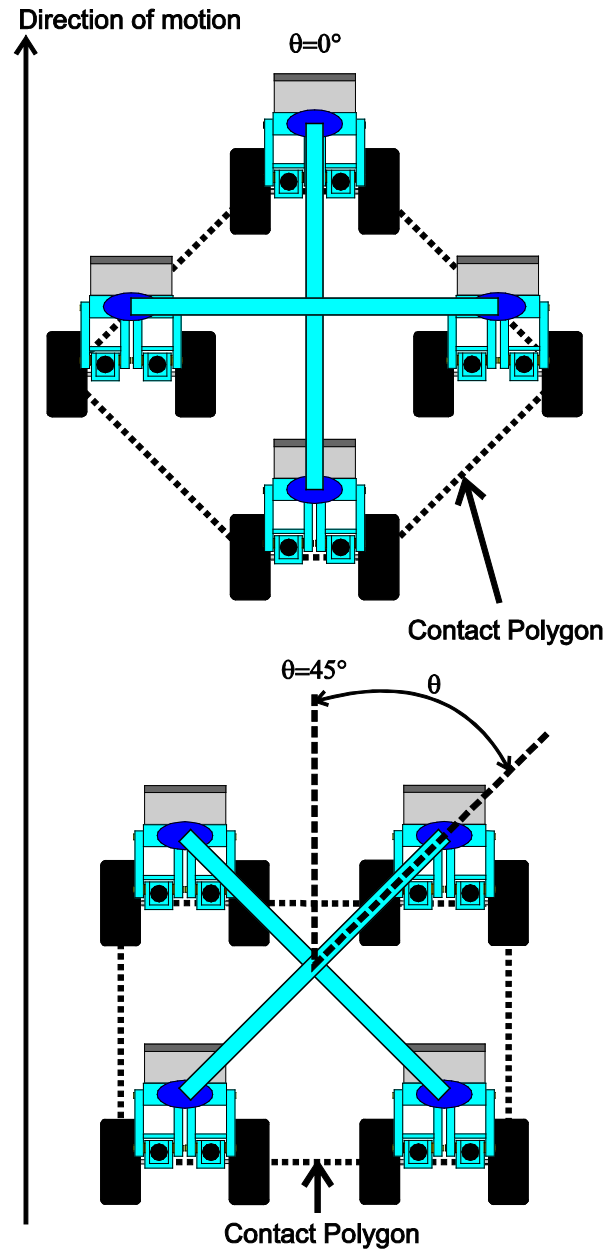


Figure 27: The convex contact polygon for two different ODV configurations. In the case $\theta = 0$, two of the wheels lie within the convex polygon and therefore do not constitute a vertex of the polygon.

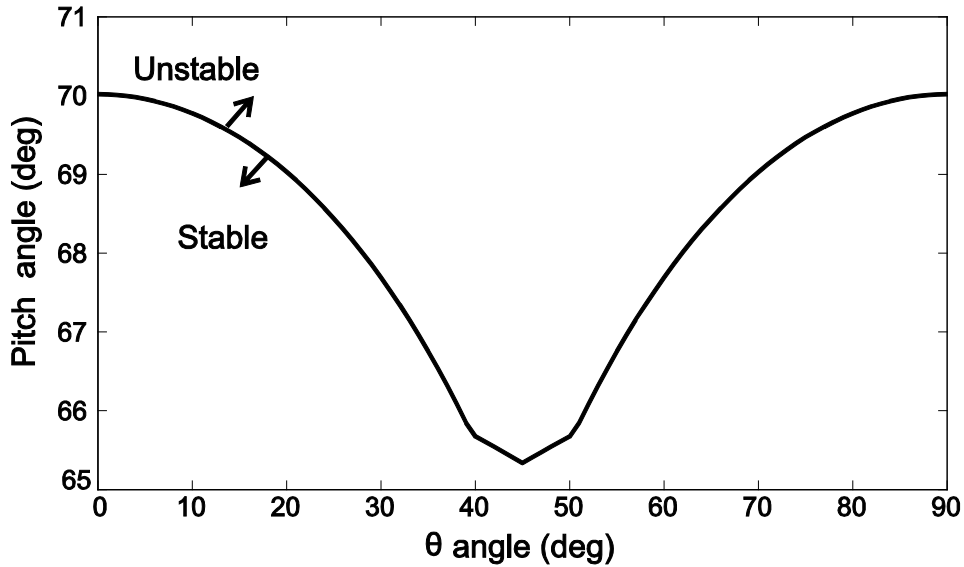


Figure 28: Tip-over angle as a function of orientation, (θ), angle.

4.3 Tip-over as a function of roll and pitch angle

To understand if roll angle affects the tip-over stability, we focus on the two extreme configurations (see Figure 28), $\theta = 0$ degrees, and $\theta = 45$ degrees. Figures 29 and 30 show the Force Angle Stability measure as a function of the roll and pitch angles. Recall that the system is stable whenever this measure is greater than 0, and a value less or equal than 0 means that a tip-over is in progress. Notice that in the $\theta = 0$ degrees case the vehicle is stable for a larger set of roll and pitch angle values than it is in the $\theta = 45$ degrees case. Depending on the roll angle, the vehicle may tip-over before it reaches its maximum climbable incline (red colored area on Figure 30). Thus, even though the vehicle is omnidirectional, it is recommended to drive it with $\theta = 0$ when traversing steep terrain.

Concluding Remarks: A tip-over analysis was conducted on the vehicle when driving on a single-inclination terrain. This analysis was then extended to a pitch and roll inclination terrain. The results of the analysis found the most stable configuration to drive the vehicle, which show that it is best to operate the ODV with one ASOC leading (equivalent to $\theta = 0$) whenever possible. This decision does not affect the omnidirectionality of the vehicle, but makes the vehicle more stable when the vehicle is operating on steeply inclined terrain.

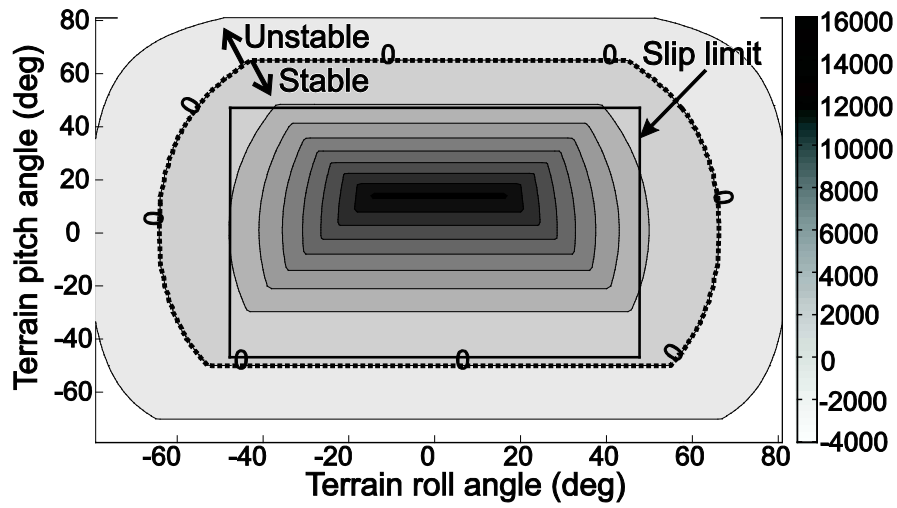


Figure 29: Stability metric for $\theta = 0$ degrees as function of pitch and roll angle.

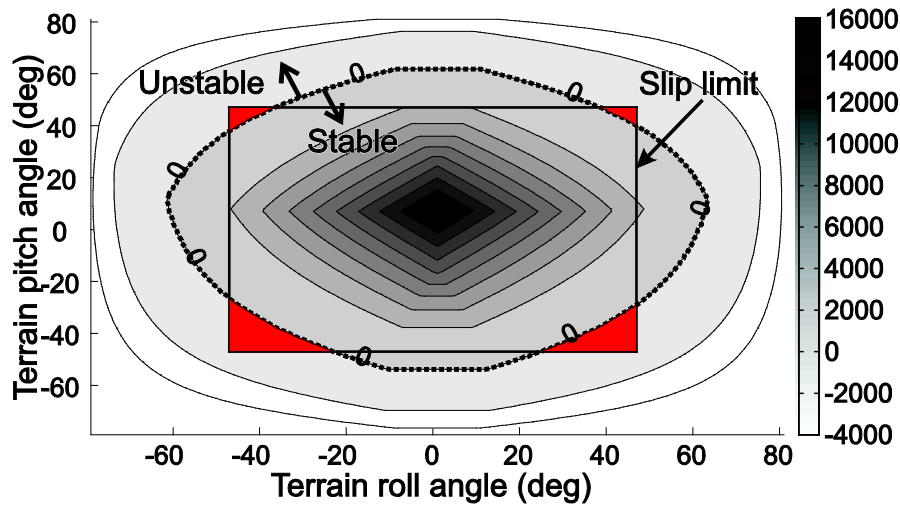


Figure 30: Stability metric for $\theta = 45$ degrees as function of pitch and roll angle. The red colored area is sets of angle for which tip-over occurs before slip.

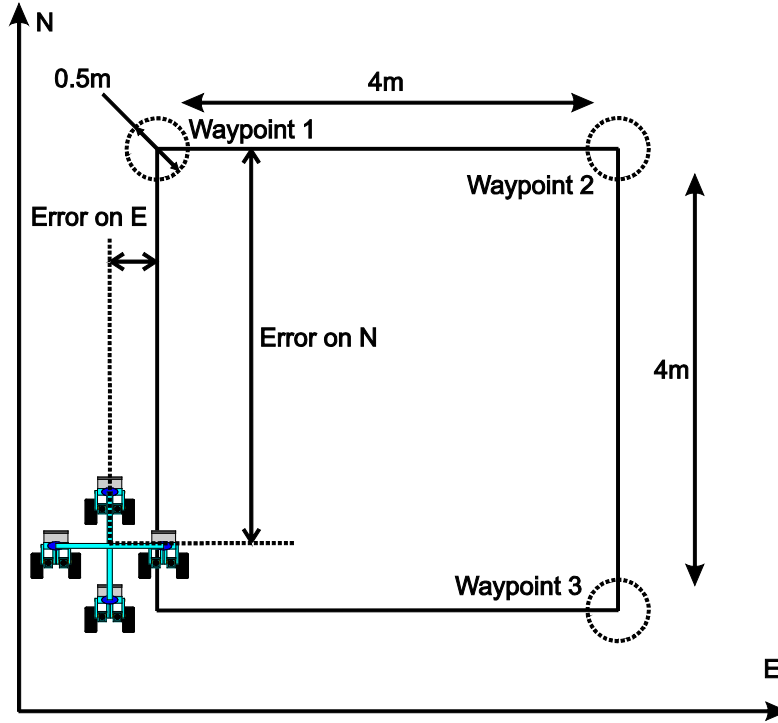


Figure 31: Expected path of the ODV during the testing.

5 Experimental Validation of the ODV

This section describes initial experimental results performed with the ODV to validate its ability to autonomously follow a non-smooth path. To begin, several key parameters of the omnidirectional vehicle were determined experimentally and are detailed in Table 9.

Table 9: UGV metrics.

Item	Value
Mass	32 kg
Maximum Speed	1.3 m/s
Maximum operating time (at max speed)	27 min
Maximum scalable incline (experimental)	47°

In order to demonstrate the omnidirectionality of the vehicle, the vehicle was commanded to follow a square path, with four way points and a constant rate of rotation and mean velocity. Figure 31 presents the path and way points tolerances.

The mean velocity is set to be constant in the code at 0.8m/s. Figure 32 presents the current controller used to validate the embedded electronics. It uses position feedback from the GPS and controls the velocity of the vehicle to correct its position. In order to simplify the model, a simple proportional controller is used. The error between the current position and the desired position is computed, a gain K_p is applied to it, and is used as velocity input in the direction of the error to reduce it.

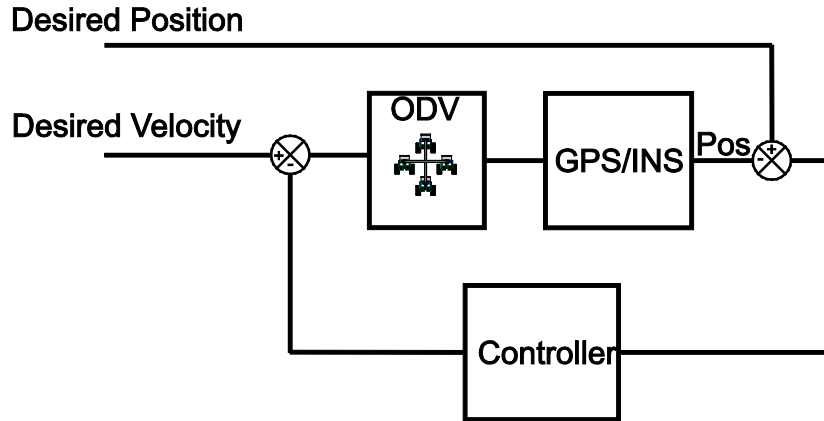


Figure 32: Position controller used to validate the embedded electronics.

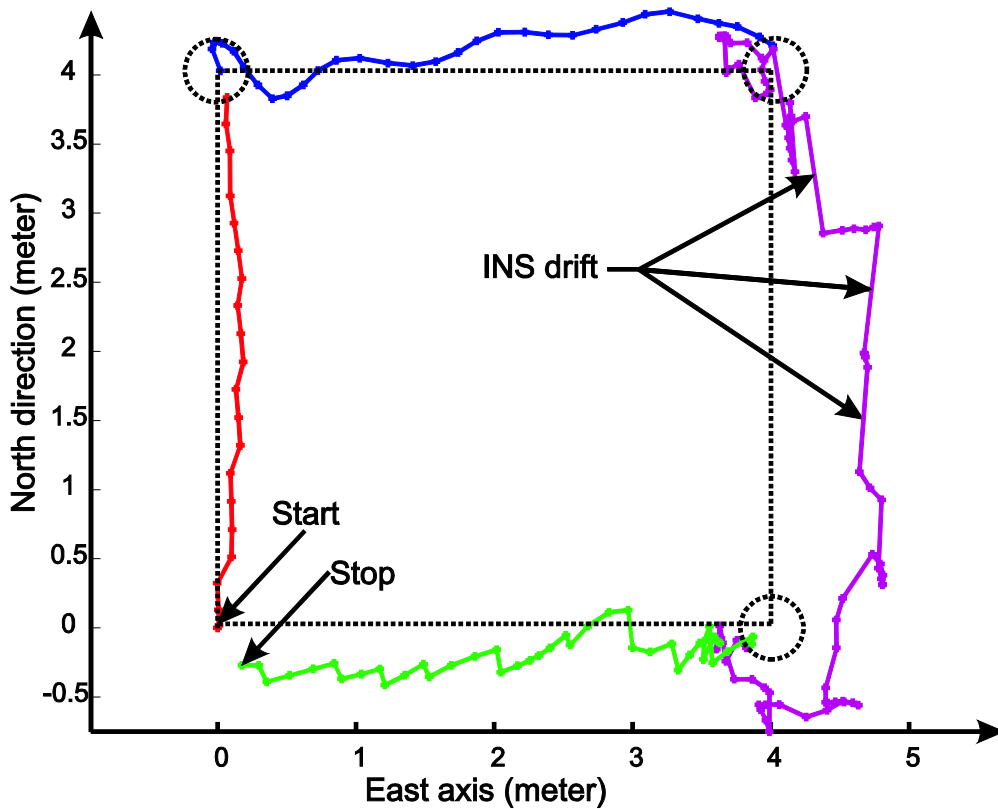


Figure 33: Position of the vehicle along a square.

5.1 Results

Figure 33 shows the vehicle's position in the ENU coordinate frame. The circles show the waypoints.

Several conclusions arise from the results:

1. The vehicle generally follows the path and goes through every way point. This indicates that the main structure of the code is working properly.

2. The position error is large when the vehicle changes its direction. There are several possible explanations for this unacceptable error. First, the controller gain is poorly tuned for the application. Second, and the most likely explanation, is that multiple mechanical errors result in the poor performance. These problems are discussed in detail in the next section.

3. The data coming from the GPS/INS is not accurate enough for the experiments. The data from the GPS possible drifts in several portions of the path. Table 10 shows the specifications of the INS unit. Future tests need to be run in an open-sky field to avoid these issues.

Table 10: Specification of the Novatel Span CPT.

Item	Accuracy
Horizontal Position Accuracy (RMS)	0.1m
Velocity Accuracy	0.02m/s
Roll and Pitch Accuracy (RMS)	0.05°
Azimuth (RMS)	0.1°



Figure 34: Damaged motors.

5.2 Mechanical Failures Encountered During Experimentation.

During vehicle testing, a variety of mechanical issues arose. Figure 34 illustrates two issues pertaining to the motors. The left side of the figure shows a bent motor shaft. The leading thought as to the cause of this issues is that when the wheel is stuck, the force applied by the motor to the shaft exceeds the gearbox shaft strength. According to the manufacturer's specifications, the motor can output a peak torque is about 0.9Nm. The gearbox has an 18:1 reduction with 75% of efficiency. Therefore, the maximum peak torque on the gearbox output is 12Nm. However, the gearbox can handle a torque up to 6Nm peak. As a result, the bevel gears connecting the motors to the drive shaft become misaligned and wear down.

On the right side of Figure 34, another problem is illustrated. The gears are mounted on motors using a set screw. Two set screws are used for each gear, set apart by 90. The torque transmitted through the gears is too large for the set screw, which results in the gears rotating about the shaft. The maximum transmitted torque for set screw of M4 diameter is about 2.5Nm. When a wheel experiences the stall torque from the motor, the peak torque can reach 12Nm, which exceeds the set screws limits.

These two problems are currently being addressed. New gearboxes with larger shaft diameters (10mm) will be employed. This should prevent the shaft from bending. Also, as the diameter of the shaft is bigger, a key will be used to stop the gear from rotating around the shaft. This will eliminate the problem with the set screws. Another solution is to replace the current

motor driver with more advanced one that would allow current control. This would allow to control the maximum torque of the motor and therefore avoid bending the shafts.

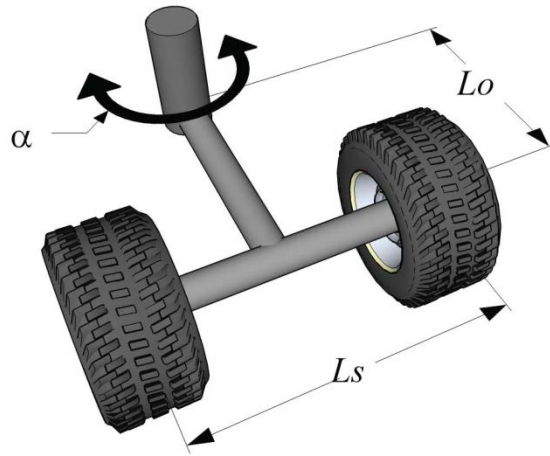


Figure 35: Illustration of an Active Split Offset Castor (ASOC).

5.3 Concluding Remarks

This section presented preliminary results that are meant to exemplify the omnidirectional capabilities of the vehicle. Unfortunately several mechanical errors were encountered due to improper sizing of the transmission elements of the vehicle. These mistakes are being addressed and we expect significantly improved results in the near future.

6 Development of the Equations of Motion for a Dynamic Controller

This section details the derivation of the dynamic equations of motion for the system and compares an inverse dynamic controller with the previously implemented kinematic controller. The ultimate goal is to compare the controller based on the equations of motion to the kinematic controller originally used for the ODV. However, as noted in the following derivation, several assumptions need to be made in order to complete the derivation. These assumptions may not be valid on rough terrain. We have also attempted to derive the equations of motion for the system operating on three-dimensional terrain; however, this attempt has not resulted a closed-form solution and we fear that the goal may not be achievable.

In the section 6.1 the dynamic equations of motion for the ODV are derived. Section 6.2 details the derivation of the controller and compares the results with the previously implemented kinematic controller.

6.1 Vehicle Dynamic Model

In this section the dynamic equations of motion for an omnidirectional UGV consisting of n ASOCs is presented. Note that only two ASOCs are required to achieve omnidirectional motion (with the addition of passive caster to maintain stability), but previous analysis has shown that three or four ASOCs are optimal when operating on terrain of various composition [20]. Figure 36 shows a single ASOC in the inertial reference frame, and the complete UGV using n ASOCs is shown in Fig. 37. The nomenclature for the model is given in Table 11. Note that the external forces acting on the wheels would need to be measured in real-time on an experimental system. Although challenging, estimation of these forces is not unprecedented [1, 8].

Table 11: Nomenclature for the Dynamic Model

Symbol	Description
\mathbf{I}	Inertial reference frame
\mathbf{C}	Caster reference frame
L_O	Distance between \mathbf{C} and wheel axle
L_S	Distance between wheels
r	Wheel radius
b	Distance between caster c.o.m and wheel axle
L	Distance of UGV c.o.m to caster axis
ω_i	Vector of right and left wheel angular velocities
\mathbf{x}_i	Position of i^{th} caster in \mathbf{I} , $[x_i \ y_i]$
α_i	Angular position of i^{th} caster w.r.t i_1 axis
\dot{x}_{mi}^C	Velocity of c.o.m of i^{th} caster along c_1
\dot{y}_{mi}^C	Velocity of c.o.m of i^{th} caster along c_2
\mathbf{X}	Position vector of UGV, $[X \ Y \ \phi]$
ϕ	Angular position of UGV in \mathbf{I}
F_{ri}^C, F_{li}^C	Longitudinal forces from the wheels in \mathbf{C}
R_{ri}^C, R_{li}^C	Lateral forces from the wheels in \mathbf{C}
F_{xi}^C, F_{yi}^C	Forces acting on the axis of i^{th} caster in \mathbf{C}
J_C	Moment of inertia of caster about the vertical axis
j_w	Moment of inertia of wheel about wheel's rotational axis
J	Moment of inertia of UGV body about vertical axis
m	ASOC mass
m_u	UGV body mass
τ_i	Driving torque acting on i^{th} caster wheels
k	Transmission gear ratio

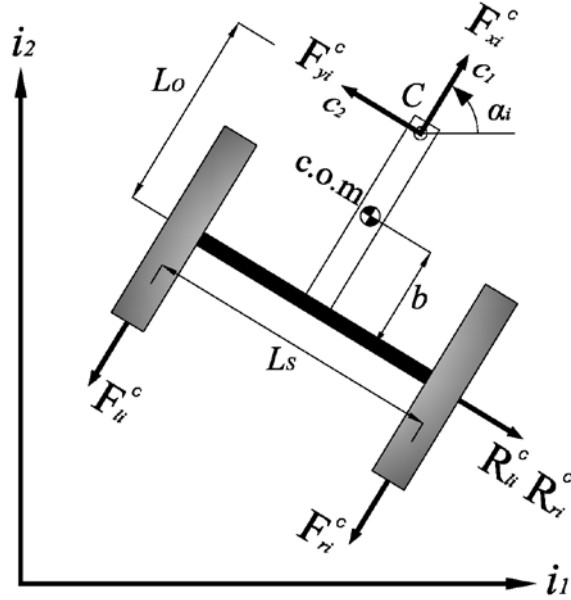


Figure 36: An illustration of a single ASOC in the inertial reference frame. i_1 and i_2 are unit vectors in the X and Y directions.

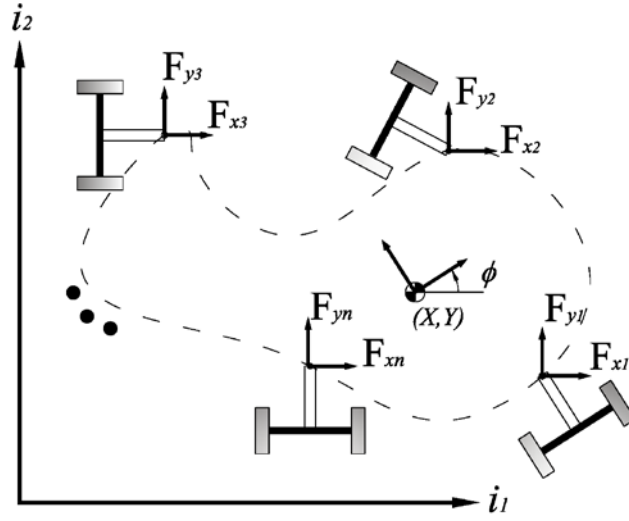


Figure 37: Top view of the UGV model with arbitrary number of ASOCs.

Using inverse kinematics, the angular velocities of the wheels are related to the velocity of point C by:

$$\omega_i = A_i \dot{x}_i \quad (23)$$

where:

$$A_i = \frac{1}{r} \begin{bmatrix} \cos \alpha_i - \frac{L_S}{2L_O} \sin \alpha_i & \sin \alpha_i + \frac{L_S}{2L_O} \cos \alpha_i \\ \cos \alpha_i + \frac{L_S}{2L_O} \sin \alpha_i & \sin \alpha_i - \frac{L_S}{2L_O} \cos \alpha_i \end{bmatrix}$$

The angular velocity of the ASOC is related to the wheel velocities by:

$$\dot{\alpha}_i = \frac{r}{L_S} (\omega_{ri} - \omega_{li}) \quad (24)$$

Let $\dot{x}_c = [\dot{x}_1^T \dots \dot{x}_n^T]^T$. The velocities of casters can be related to the robot velocity, $\dot{X} = [\dot{X} \ \dot{Y} \ \dot{\phi}]^T$ by:

$$\dot{x}_c = G \dot{X} \quad (25)$$

where G is the associated Jacobian and can be computed as:

$$G = \begin{bmatrix} \frac{\partial x_1}{\partial X} & \frac{\partial x_1}{\partial Y} & \frac{\partial x_1}{\partial \phi} \\ \frac{\partial y_1}{\partial X} & \frac{\partial y_1}{\partial Y} & \frac{\partial y_1}{\partial \phi} \\ \vdots & \vdots & \vdots \\ \frac{\partial x_n}{\partial X} & \frac{\partial x_n}{\partial Y} & \frac{\partial x_n}{\partial \phi} \\ \frac{\partial y_n}{\partial X} & \frac{\partial y_n}{\partial Y} & \frac{\partial y_n}{\partial \phi} \end{bmatrix}$$

Let the vector of wheel velocities be:

$$\omega = [\omega_1^T \dots \omega_n^T]^T$$

and

$$\mathbf{A} = \text{Diag} (\mathbf{A}_1, \dots, \mathbf{A}_n)$$

then $\boldsymbol{\omega}$ and $\dot{\mathbf{x}}_c$ are related by:

$$\boldsymbol{\omega} = \mathbf{A} \dot{\mathbf{x}}_c \quad (26)$$

Thus,

$$\boldsymbol{\omega} = \mathbf{A} \mathbf{G} \dot{\mathbf{X}} \quad (27)$$

Balancing forces and moments acting on c.o.m of i^{th} caster gives the following:

$$\begin{aligned} m \ddot{x}_{mi}^C &= F_{ri}^C + F_{li}^C - F_{xi}^C \\ m \ddot{y}_{mi}^C &= R_{ri}^C + R_{li}^C - F_{yi}^C \\ J_C \ddot{\alpha}_i + (R_{ri}^C + R_{li}^C) b + F_{yi}^C (L_O - b) &= (F_{ri}^C - F_{li}^C) \frac{L_S}{2} \end{aligned} \quad (30)$$

The non-holonomic no-slip constraint is given by the condition that the velocity of the point at the center of axle in the c_2 direction is zero. It is noted that this assumption may not hold in outdoor terrain consisting of loose, granular soil. This will be evaluated experimentally in future work. From this it can be shown that:

$$\dot{y}_{mi}^C = b \dot{\alpha}_i \quad (31)$$

Differentiating (31) and defining, $\mathbf{F}_i^C = [F_{xi}^C \ F_{yi}^C]^T$, $\dot{\mathbf{x}}_{mi}^C = [\dot{x}_{mi}^C \ \dot{\alpha}_i]^T$, and $\mathbf{F}_{Wi} = [F_{ri}^C \ F_{li}^C]^T$ then (28), (29), and (30) can be written as:

$$\mathbf{F}_{Wi} = \mathbf{B}_i \ddot{\mathbf{x}}_{mi}^C + \mathbf{D}_i \mathbf{F}_i^C \quad (32)$$

where:

$$\mathbf{B}_i = \frac{1}{2} \begin{bmatrix} m & \frac{2(J_C + mb^2)}{L_S} \\ m & \frac{-2(J_C + mb^2)}{L_S} \end{bmatrix}, \quad \mathbf{D}_i = \frac{1}{2} \begin{bmatrix} 1 & \frac{2L_O}{L_S} \\ 1 & \frac{-2L_O}{L_S} \end{bmatrix}$$

Using the transformation from C to I, (32) can be written as:

$$\mathbf{F}_i = \mathbf{T}_{iC}^I \mathbf{D}_i^{-1} (\mathbf{F}_{Wi} - \mathbf{B}_i \ddot{\mathbf{x}}_{mi}^C) \quad (33)$$

where:

$$\mathbf{T}_{iC}^I = \begin{bmatrix} \cos \alpha_i & -\sin \alpha_i \\ \sin \alpha_i & \cos \alpha_i \end{bmatrix}$$

Thus, the equation for the forces acting on the α axis of the i^{th} caster, we can map these forces on the UGV center using the Jacobian already given above. If $\mathbf{F} = [\mathbf{F}_1^T \ \dots \ \mathbf{F}_n^T]^T$ and $\mathbf{M} = \text{Diag} (m_u, m_u, J)$, then forces and torques acting on the robot body can be given by:

$$\mathbf{M} \ddot{\mathbf{X}} = \mathbf{G}^T \mathbf{F} \quad (34)$$

\mathbf{F} can be written as:

$$\mathbf{F} = \mathbf{D}^{-1} (\mathbf{F}_W - \mathbf{B} \ddot{\mathbf{x}}_m^C) \quad (35)$$

where:

$$\begin{aligned}\mathbf{D}^{-1} &= \text{Diag}(\mathbf{T}_{1C}^I \mathbf{D}_1^{-1}, \dots, \mathbf{T}_{nC}^I \mathbf{D}_n^{-1}) \\ \mathbf{B} &= \text{Diag}(\mathbf{B}_1, \dots, \mathbf{B}_n) \\ \mathbf{F}_W &= [F_{W1}^T \quad \dots \quad F_{Wn}^T]^T \\ \ddot{\mathbf{x}}_m^C &= [\ddot{x}_{m1}^{CT} \quad \dots \quad \ddot{x}_{mn}^{CT}]^T\end{aligned}$$

The relation between the velocity of c.o.m of i^{th} caster in \mathbf{C} and $\dot{\mathbf{x}}_i$ can be given as:

$$\dot{\mathbf{x}}_{mi}^C = \mathbf{E}_i \dot{\mathbf{x}}_i \quad (36)$$

where:

$$\mathbf{E}_i = \begin{bmatrix} \cos \alpha_i & \sin \alpha_i \\ -\frac{1}{L_O \sin \alpha_i} & \frac{1}{L_O \cos \alpha_i} \end{bmatrix}$$

Expanding (36) for all n ASOCs yields:

$$\dot{\mathbf{x}}_m^C = \mathbf{E} \dot{\mathbf{x}}_c \quad (37)$$

where:

$$\mathbf{E} = \text{Diag}(\mathbf{E}_1, \dots, \mathbf{E}_n)$$

Using (25), (37) can be written as:

$$\dot{\mathbf{x}}_m^C = \mathbf{E} \mathbf{G} \dot{\mathbf{X}} \quad (38)$$

Differentiating (38) yields:

$$\ddot{\mathbf{x}}_m^C = (\dot{\mathbf{E}} \mathbf{G} + \mathbf{E} \dot{\mathbf{G}}) \dot{\mathbf{X}} + \mathbf{E} \mathbf{G} \ddot{\mathbf{X}} \quad (39)$$

Equation (39) gives the acceleration of the center of mass of the ASOCs. Now the wheel torques for each wheel are introduced assuming that the friction in the driving mechanism is negligible and defining:

$$\mathbf{R} = r \mathbf{I}_{2n} \quad (40)$$

$$\mathbf{K} = k \mathbf{I}_{2n} \quad (41)$$

$$\boldsymbol{\tau} = [\boldsymbol{\tau}_1^T \quad \dots \quad \boldsymbol{\tau}_n^T]^T \quad (42)$$

$$\mathbf{J}_W = j_W \mathbf{I}_{2n} \quad (43)$$

where \mathbf{I}_{2n} is the $2n \times 2n$ identity matrix. The actuator dynamics can be given as:

$$\mathbf{K} \boldsymbol{\tau} = \mathbf{J}_W \dot{\boldsymbol{\omega}} + \mathbf{R} \mathbf{F}_W \quad (44)$$

Differentiating (27) yields:

$$\dot{\boldsymbol{\omega}} = (\dot{\mathbf{A}} \mathbf{G} + \mathbf{A} \dot{\mathbf{G}}) \dot{\mathbf{X}} + \mathbf{A} \mathbf{G} \ddot{\mathbf{X}} \quad (45)$$

Now using (34), (35), (39), (44), and (45) the direct dynamic model of the UGV can be written as:

$$\ddot{\mathbf{X}} = \mathbf{Y} (\mathbf{R}^{-1} \mathbf{K} \boldsymbol{\tau} - \mathbf{Z} \dot{\mathbf{X}}) \quad (46)$$

where:

$$\mathbf{Y} = [\mathbf{M} + \mathbf{G}^T \mathbf{D}^{-1} (\mathbf{R}^{-1} \mathbf{J}_W \mathbf{A} + \mathbf{B} \mathbf{E}) \mathbf{G}]^{-1} \mathbf{G}^T \mathbf{D}^{-1} \quad (48)$$

Equation (46) represents the equations of motion for a UGV employing n ASOCs. The procedure can easily be used to find equations of motion of a UGV with any number of ASOC modules.

6.2 Inverse Dynamic Control and Simulation

This section details a inverse dynamic control algorithm and compares the results to a kinematic controller used in previous work [22].

6.2.1 Inverse Dynamic Model

From (34) we can write:

$$\mathbf{F} = \mathbf{G}^\# \mathbf{M} \ddot{\mathbf{X}} \quad (49)$$

where $\mathbf{G}^\#$ is the right pseudo inverse of \mathbf{G} . Also from (35) we can write:

$$\mathbf{F}_W = \mathbf{D} \mathbf{F} + \mathbf{B} \ddot{\mathbf{x}}_m^C \quad (50)$$

Then using (39), (44), (45), (49), and (50) the inverse dynamic model can be written as:

$$\boldsymbol{\tau} = \mathbf{K}^{-1} (\mathbf{P} \dot{\mathbf{X}} + \mathbf{Q} \ddot{\mathbf{X}}) \quad (51)$$

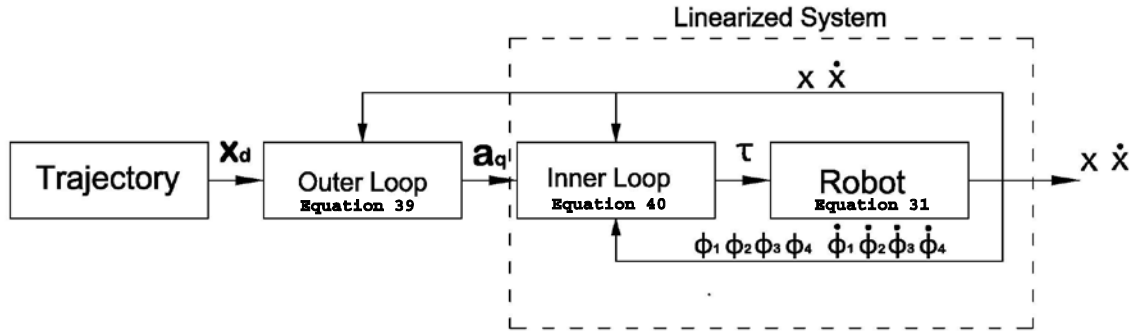


Figure 38: Control architecture for the inverse dynamic model.

where:

$$\mathbf{P} = (\mathbf{J}_W \dot{\mathbf{A}} + \mathbf{R} \mathbf{B} \dot{\mathbf{E}}) \mathbf{G} + (\mathbf{J}_W \mathbf{A} + \mathbf{R} \mathbf{B} \mathbf{E}) \dot{\mathbf{G}} \quad (52)$$

$$\mathbf{Q} = \mathbf{R} \mathbf{D} \mathbf{G}^\# \mathbf{M} + (\mathbf{J}_W \mathbf{A} + \mathbf{R} \mathbf{B} \mathbf{E}) \mathbf{G} \quad (53)$$

If the control input τ is chosen according to:

$$\boldsymbol{\tau} = \mathbf{K}^{-1} (\mathbf{P} \dot{\mathbf{X}} + \mathbf{Q} \mathbf{a}_q) \quad (54)$$

then, the combined system of (51) and (54) will reduce to:

$$\ddot{\mathbf{X}} = \mathbf{a}_q \quad (55)$$

Setting \mathbf{a}_q to:

$$\mathbf{a}_q = \ddot{\mathbf{X}}_d - \mathbf{K}_D \dot{\mathbf{e}} - \mathbf{K}_P \mathbf{e} \quad (56)$$

In (56) $\ddot{\mathbf{X}}_d$ is the desired acceleration, \mathbf{e} and $\dot{\mathbf{e}}$ are the errors in position and velocity respectively, and \mathbf{K}_P and \mathbf{K}_D are the proportional and derivative gains. Substituting (56) in (55) gives:

$$\ddot{\mathbf{e}} + \mathbf{K}_D \dot{\mathbf{e}} + \mathbf{K}_P \mathbf{e} = 0 \quad (57)$$

Equation (57) represents the inverse dynamics control law and provides the feedback linearization for trajectory tracking of UGV.

6.2.2 Simulation Results

The prototype vehicle has four ASOC modules. The Jacobian, \mathbf{G} , for the prototype vehicle with four equally spaced ASOCs can be given as:

$$\mathbf{G} = \begin{bmatrix} 1 & 0 & -L \sin \phi \\ 0 & 1 & L \sin \phi \\ 1 & 0 & -L \cos \phi \\ 0 & 1 & -L \sin \phi \\ 1 & 0 & L \sin \phi \\ 0 & 1 & -L \cos \phi \\ 1 & 0 & L \cos \phi \\ 0 & 1 & L \sin \phi \end{bmatrix}$$

On the experimental system, the angular position of the ASOC modules can be directly measured. For the simulation, angular positions and velocities are calculated using (24) and (27). Table 12 shows the physical parameters used for the simulation, which are based on the experimental system described earlier and control parameters that were tuned to yield suitable results.

Fig. 39 shows the desired trajectory of UGV in the XY plane, the trajectory of the UGV using the inverse dynamics controller, and the trajectory of the UGV using the kinematic controller.

Fig. 40 displays the total path tracking error of the UGV as a function of time when using the inverse dynamics controller and kinematic controller. The results indicate that the inverse dynamics controller performs significantly better than the kinematic controller. The RMS error for the inverse dynamics controller was 1.3 mm. For the kinematic controller the error was 21.7 mm. The differences are especially evident when the trajectory is discontinuous as a function of the path length.

Table 12: Physical Properties used in the Simulation

Parameter	Value	Units
m_u	1.98	kg
m	7.56	kg
j_W	0.0027	$kg \cdot m^2$
J_c	0.1577	$kg \cdot m^2$
J	0.1450	$kg \cdot m^2$
b	0.051	m
L_S	0.285	m
L_O	0.1425	m
r	0.08	m
L	0.415	m
k	1	—
K_P	3	—
K_D	1	—

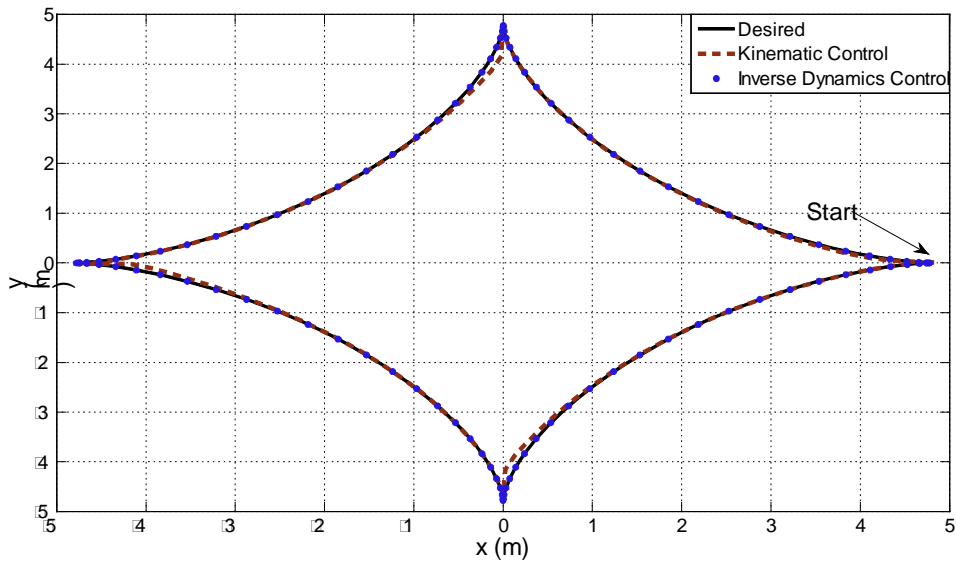


Figure 39: Path tracking results comparing the inverse dynamics controller with a kinematic controller

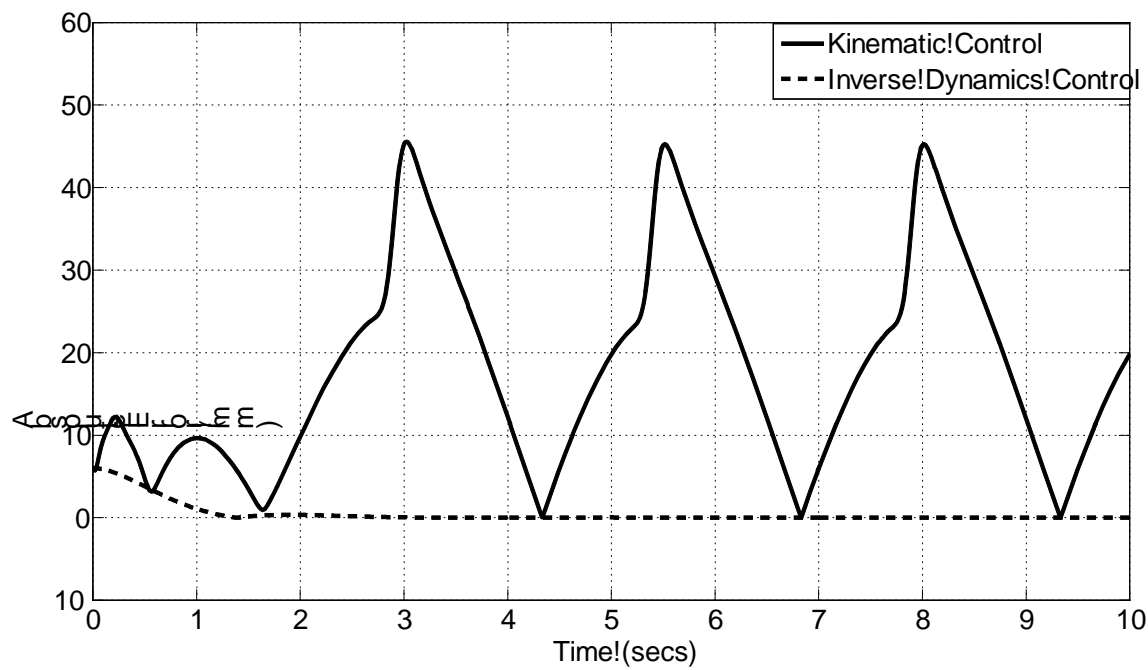


Figure 40: Path tracking error against in time.

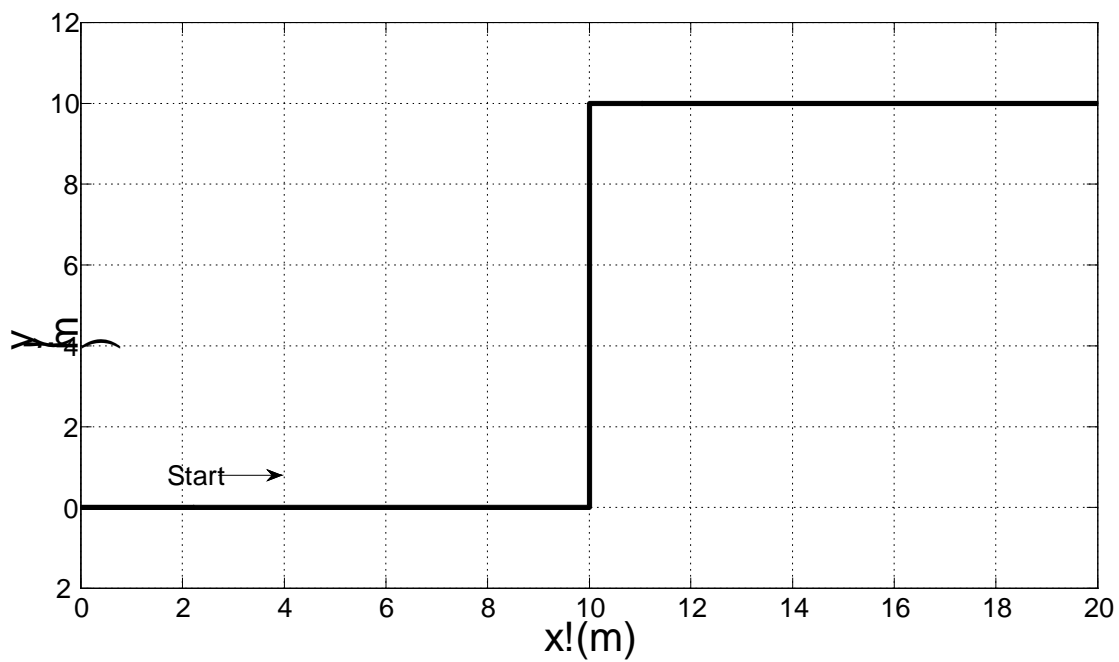


Figure 41: Step trajectory for the simulation.

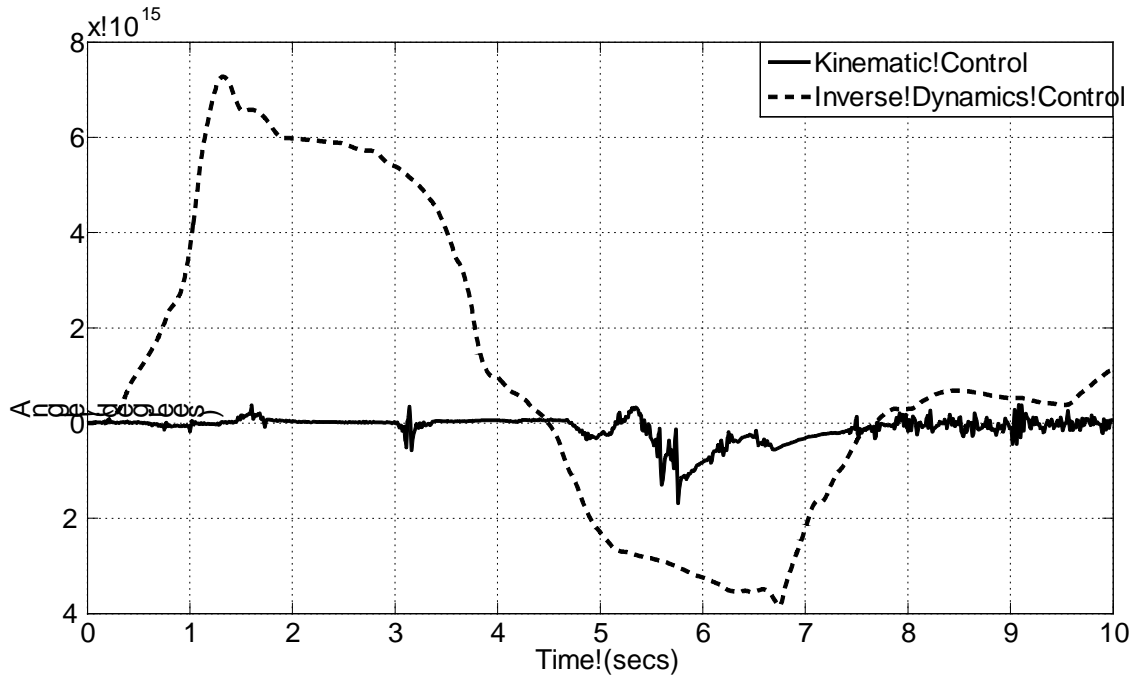


Figure 42: UGV orientation in time for the step trajectory.

A second trajectory is shown in Fig. 41 for the UGV. This trajectory was chosen to demonstrate the omnidirectional capabilities of the UGV. The desired orientation of the UGV was 0 degrees throughout the path. Fig. 42 shows the orientation of the UGV in time for the tracked trajectory.

Note that the UGV maintains its orientation for the entire path with negligible error for both inverse dynamics and kinematic controller. Fig. 43 shows the absolute velocity of the UGV for the step trajectory. For the inverse dynamics control the RMS absolute velocity of the UGV for the path is 3.21 m/sec, and for the kinematic control, the RMS absolute velocity is 3.20 m/sec. The elapsed time to regain the desired velocity at the edges was 1.0 secs both the controllers. At the edges, the magnitude of the velocity does not fall below then 44.0% of the desired magnitude of 3 m/sec for the inverse dynamics control and approaches zero for the kinematic control. Fig. 44 shows the angular position of one ASOC in time. The ASOCs rotates by ≈ 2 radians at the edges in approximately 0.5 s for both controllers.

6.3 Concluding Remarks

In this section, the dynamic equations of motion for a unique omnidirectional UGV consisting of an arbitrary number of ASOCs were derived and an inverse dynamics based controller was chosen to analyze the model. Using simulations an inverse dynamics control law was compared to a kinematic control law for the prototype vehicle. Simulation results indicate that an inverse dynamic controller performed better than the kinematic controller and the UGV was able to follow the desired trajectories with good accuracy while exhibiting omnidirectional capabilities.

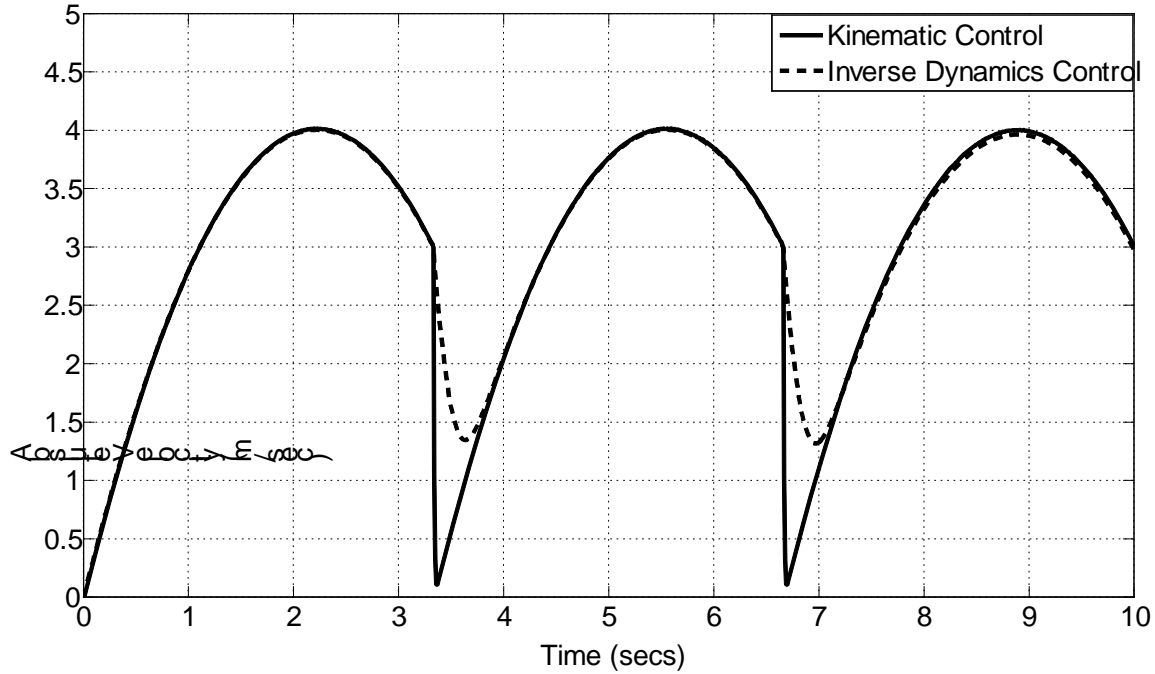


Figure 43: Absolute velocity of UGV against time for the step trajectory.

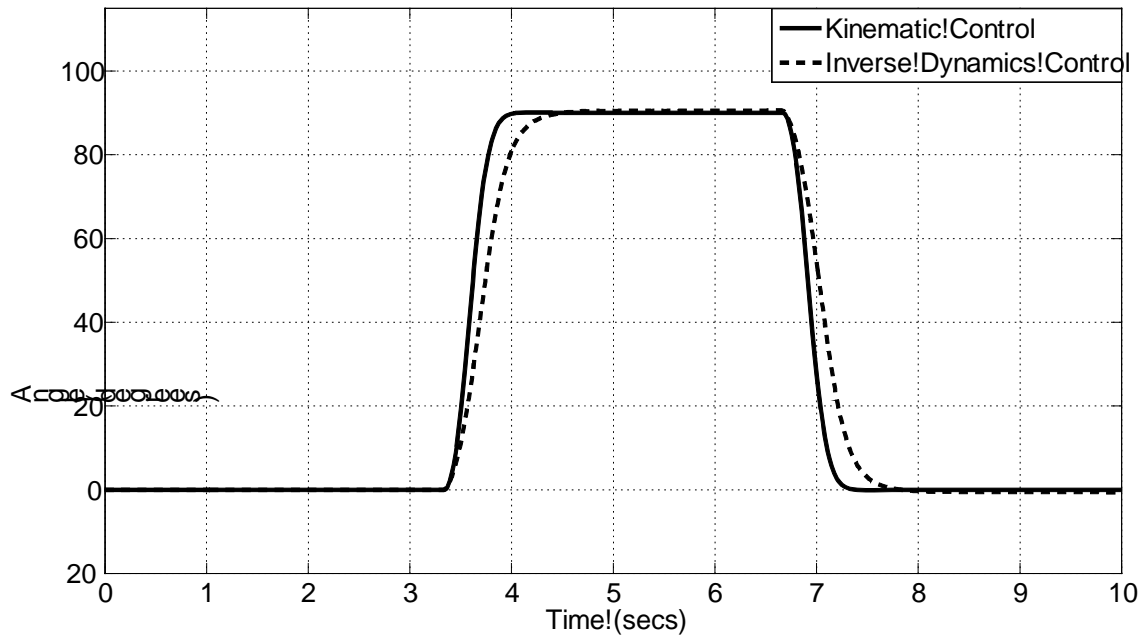


Figure 44: Angular position of one ASOC against time for the step trajectory.

It is noted that the dynamic model derived in this paper is for a robot operating on a planar surface, and that it is not always appropriate to assume that outdoor terrains are planar. Thus, future work will entail experimental validation of these results in an outdoor environment. Based on the results of those experiments, a full six DOF dynamic model and controller may need to be derived and implemented.

References

- [1] Guillaume Baffet, Ali Charara, and Daniel Lechner. Estimation of vehicle sideslip, tire force and wheel cornering stiffness. *Control Engineering Practice*, In Press, Corrected Proof:–, 2009.
- [2] P. Bartlett, D. Wettergreen, and W. Whittaker. Design of the scarab rover for mobility and drilling in the lunar cold traps. In *International symposium on artificial intelligence, robotics and automation in space*, CA, USA, 2008.
- [3] M. G. Bekker. *Introduction to Terrain-Vehicle Systems*, volume I. University of Michigan Press, Ann Arbor, MI, 1969.
- [4] W. D. III Carrier. Trafficability of Lunar Microrovers (Part 3). Technical report tr96-01, Lunar Geotechnical Institute, July 1996.
- [5] L. Ferriere and B. Raucent. Rollmobs, a new universal wheel concept. In *IEEE International Conference on Robotics and Automation*, pages 1877–1882, 1998.
- [6] K. Iagnemma, M. Udengaard, G. Ishigami, Matthew Spenko, S. Oncu, and I. Khan. Design and development of an agile, man portable unmanned ground vehicle. In *Proceedings of the 26th Annual Army Science Conference*, 2008.
- [7] I. Khan and M. Spenko. Dynamics and control of an omnidirectional unmanned ground vehicle. In *IEEE/RSJ international conference on intelligent robots and systems*, MO, USA, 2009. IEEE.
- [8] James Lacombe. Tire model for simulations of vehicle motion on high and low friction road surfaces. In *WSC '00: Proceedings of the 32nd conference on Winter simulation*, pages 1025–1034, San Diego, CA, USA, 2000. Society for Computer Simulation International.
- [9] R. Lindemann and C. Vorhees. Mars exploration rover mobility assembly design, test, and performance. In *IEEE SMC Conference*, HI, USA, 2005. IEEE.
- [10] G. Meirion-Griffith and M. Spenko. An empirical study into the terramechanics of small unmanned ground vehicles. In *IEEE Aerospace Conference*, Big Sky, MT, 2010. IEEE.
- [11] P. Muir and C. Neuman. Kinematic modeling for feedback control of an omnidirectional wheeled mobile robot. In *IEEE International Conference on Robotics and Automation*, 1987.
- [12] C. Nie, S. Cusi von Dooren, J. Shah, and M. Spenko. Execution of dynamic maneuvers for unmanned ground vehicles using variable internal inertial properties. In *IEEE/RSJ international conference on intelligent robots and systems*, MO, USA, 2009. IEEE.
- [13] P. Enge P. Misra. *Global Positioning System: Signal, measurements, and performance*. Ganga-Jamuna Press, 2001.
- [14] E. Papadopoulos and D. A. Rey. A new measure of tipover stability margin for mobile manipulators. In *Proceedings of the IEEE Int. Conf. on Robotics and Automation*, 1996.
- [15] L. Richter, M. Bernasconi, and P. Coste. Analysis, design and test of wheels for a 4kg-class mobile device for the surface of mars. In *14th International Conference of the International Society for Terrain-Vehicle Systems*, pages 1–11, Vicksburg, MS, 2002. ISTVS.

- [16] G .P. Scott, G. N. Meirion-Griffith, C. Saaj, and E. Moxey. A comparative study of the deformation of planetary soils under tracked and legged locomotion. In Space 2008 Conference and Exposition, volume 7897, pages 1–12, San Diego, CA, 2008. AIAA.
- [17] D. Shirley. Mars Pathfinder microrover flight experiment - a paradigm for very low-cost spacecraft. Memo i aa-l-0506, JPL, 1994.
- [18] K. Terzaghi. Theoretical Soil Mechanics. John Wiley and Sons, New York, USA, 1943.
- [19] M. Udengaard and K. Iagnemma. Kinematic analysis and control of an omnidirectional mobile robot in rough terrain. In Proceedings of the IEEE/RSJ International Conference on Intelligent Robots and Systems, pages 795–800, 2007.
- [20] M. Udengaard and K. Iagnemma. Design of an omnidirectional mobile robot for rough terrain. In Proceedings of the 2008 IEEE International Conference on Robotics and Automation, 2008.
- [21] M. Wada and S. Mori. Holonomic and omnidirectional vehicle with conventional tires. In IEEE International Conference on Robotics and Automation, pages 3671–3676, 1996.
- [22] H. Yu, Matthew Spenko, and S. Dubowsky. Omni-directional mobility using active split offset castors. ASME Journal of Mechanical Design, 126(5):822–829, 2004.

1. INTRODUCTION—DESIGN OF AN OMNIDIRECTIONAL UGV BASED ON ANISOTROPIC FRICTION

An omnidirectional vehicle is able to kinematically move in any planar direction regardless of its current pose. This is in contrast to typical steered wheeled vehicles, which must travel along arcs, and thus have difficulty performing complex maneuvers. Omnidirectional vehicles have been widely applied in many practical areas: mobile robotic bases for research, materials handling vehicles (i.e. fork trucks) for logistics, and wheelchairs.

To date, a wide variety of wheels have been developed that allows a vehicle to realize omnidirectional motion. Roller wheel designs [1]-[4] employ a series of slender rollers along the circumference of a wheel that are mounted perpendicular to the wheel rotational direction (Fig. 1). The wheel generates thrust in the wheel's rotational (longitudinal) direction and passively slides in the lateral direction using the slender rollers. Omnidirectional motion of vehicle is obtained by orienting several of these wheels (usually, three or four) in different directions. The common design element of these wheels is that they possess a single wheel with a large ("major") diameter, which contains many smaller diameter wheels with axes of rotation that are skew to the major axis.

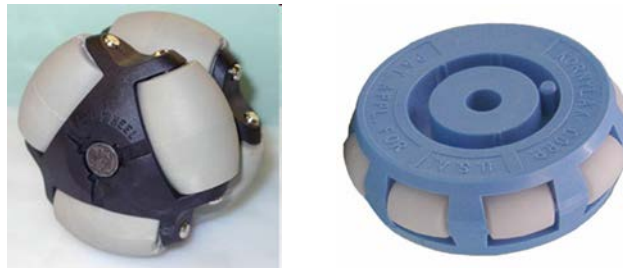


Fig.1 Examples of roller wheels (Left: *Omniwheel*, Right: *Transwheel*[®], from *Kornylak Corporation*¹⁾)



Fig.2 Examples of vehicles using Mecanum wheels (from [1] and *AirTrax*²⁾)

Mecanum wheels [4]-[8] are similar to roller wheels in that they employ rollers along the outer edge of a wheel; however, the rollers are aligned at 45 degrees to the plane of the wheel to produce angular contact forces with the ground. Vehicles equipped with four mecanum wheels, as shown in Fig. 2, can produce omnidirectional motion. While the vehicles can move forward and backward as conventional wheels do, they can also move laterally by rotating the front and rear wheels in opposite directions.

A drawback of these wheel designs is that they are complex, with numerous roller, axle, and bearing elements. The novel wheel described in this report is able to realize omnidirectional motion by exploiting the same "driving and sliding" property utilized by conventional omnidirectional drive wheels. The novelty and utility of the invention derives from the fact that the wheel is a single component, with two distinct materials. Thus the proposed wheel is less

complex, more robust (due to fewer moving components), and potentially less expensive to produce than conventional omnidirectional wheels.

This report is organized as follows: Section 2 describes the design of the proposed wheel and mechanism of the anisotropic friction realized by the wheel. Section 3 presents a prototype of an omnidirectional vehicle using the proposed wheels. A comparison of the proposed wheel and conventional wheels are also described.

2. OMNIDIRECTIONAL WHEEL WITH ANISOTROPIC FRICTION

2.1 Design Concept

The proposed wheel has a large (“major”) diameter with a series of bendable “nodes” on its circumference (see Fig. 3). Each node is composed of two materials with differing friction property. A high friction material is present in a narrow strip on the surface of the node, with the strip oriented parallel to the wheel face (i.e. perpendicular to the axis of rotation of the wheel). The high friction material can be imparted to the node through various manufacturing processes, including molding and deposition, or by adhesion or fastening. In the prototype shown in Fig. 3, the high friction material was imparted in a rapid prototyping process—thus the wheel was “printed” from multiple materials in a single process. During wheel rotation, the high friction strip contacts the ground and generates a traction force in the vehicle’s longitudinal direction.

A node’s side faces (i.e. the regions outside the strip) are composed of a material with low friction properties. Also, the node itself is designed in such a way that the connection to the major diameter (the “root”) is somewhat flexible. Therefore, when the wheel is pushed laterally while contacting the ground, the node deforms slightly, which causes the low friction material to contact the ground (see Fig. 4). This causes the vehicle to slide. This phenomenon is described further in Section 2.3.

When multiple wheels (ideally four) are arranged as shown in Fig. 5, wheels in orthogonal directions can be driven to generate traction forward, backward, or laterally. The driven wheels experience only modest resistance from sliding wheels. Thus, by exploiting the anisotropic friction property described here, a vehicle with the proposed wheels can realize omnidirectional motion.

2.2 Omnidirectional Wheel

A CAD design and prototype of the proposed wheel for omnidirectional vehicle is shown in Fig.3. The prototype has a dimension of 49.0 mm (diameter) and 18.5 mm (width), and weighs 15.0 g. The wheel consists of wheel rim made of low friction material (83 Shore Scale D, gray-colored part in Fig.3), a thin strip of high friction material (27 Shore Scale A, orange-colored part), and a series of bendable nodes. The wheel is fabricated as a single-piece component using 3D printing technology³⁾, and it is possible to directly mount the wheel to a drive actuator.

The nodes should generally be closely and evenly spaced so that the motion resulting from the wheel is smooth and not bumpy in the vertical direction. In the prototype, two parallel rows of nodes were employed, with the rows slightly offset from one another, to increase smoothness of travel. In principle, three or more rows of nodes could be employed. In the current prototype, the total number of nodes is 32 aligned in dual lines, each half of which has 11.25 degrees of phase difference.

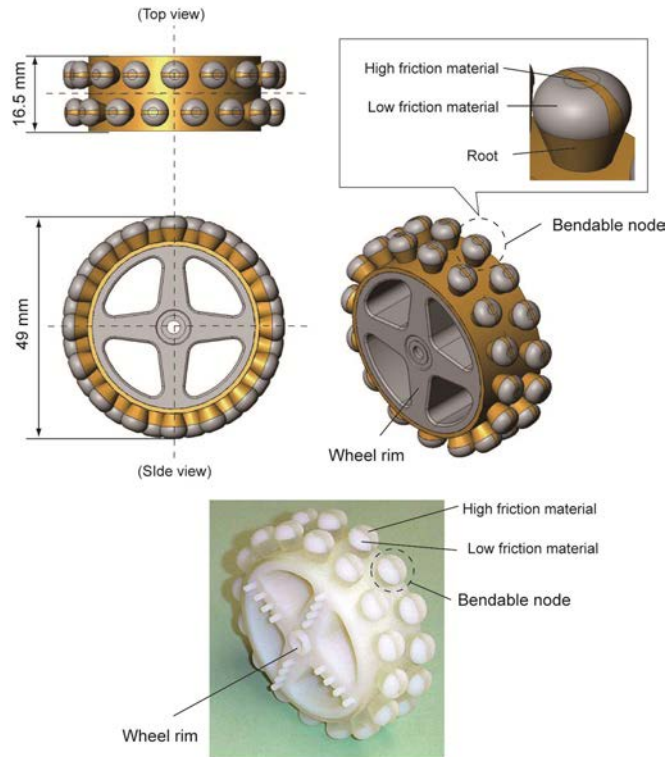


Fig.3 CAD model and prototype of the multi-material anisotropic friction wheel for omnidirectional vehicle

2.3 Bendable Node

Omnidirectional motion of a vehicle with the proposed wheel is achieved via the anisotropic friction properties of the nodes. The nodes should have a high friction strip to grip the ground and generate traction forces, just as conventional pneumatic tires do. The nodes should also have low friction side faces that will contact the ground when the node bends at the root, so that the wheel can slide, resulting in lateral motion of the vehicle. The root is designed such that a nominal load on the wheel will cause the root to deflect enough that the face of the node (i.e. the point of contact with the ground) shifts from the high friction strip to the low friction area.

The initial concept of using an anisotropic material for anisotropic friction was first presented in [9], in the context of an inchworm-like mobile robot. There, a planar “foot” with anisotropic was used in a sliding manner. The main difference between the proposed wheel and the foot reported in [9] is that 1) the device reported in [9] is a planar mechanism and not a wheel, and 2) the device of [9] cannot be used in any obvious manner to achieve omnidirectional motion.

It should be noted that the particular design of the node in Fig. 3 is only one example of a set of possible designs that could exploit the principle of anisotropic friction for omnidirectional wheeled vehicles. The node could be designed in slightly different geometries to realize different load/deflection properties, which would affect vehicle motion. Also, the geometry of the high friction strip could potentially be modified somewhat while still maintaining omnidirectional motion properties.

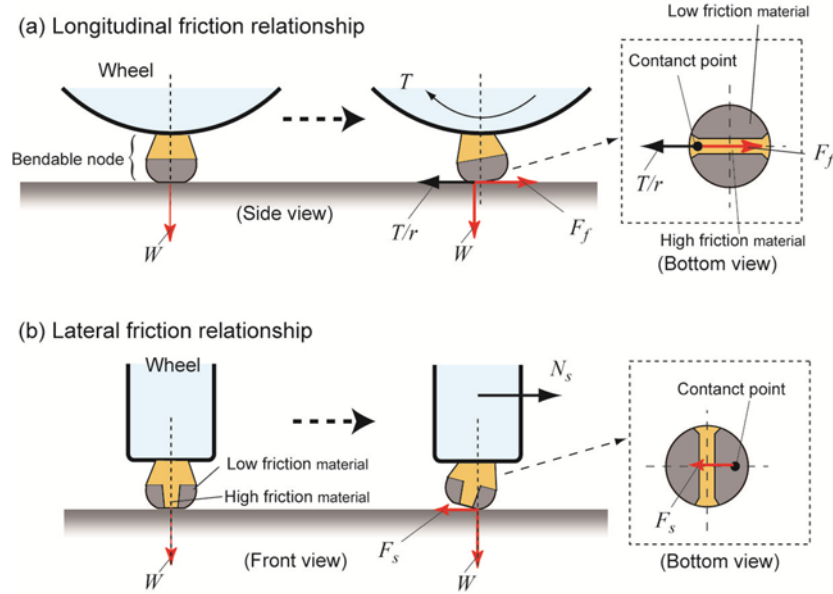


Fig.4 Anisotropic friction mechanics of the bendable node

2.4 Anisotropic Friction Mechanics

Fig. 4 illustrates the mechanics of the anisotropic friction properties realized by the proposed wheel.

When the wheel is at rest, under load from the wheel and robot (and possible a payload), the high friction strip contacts the ground, since the high friction strip lies directly beneath the wheel (i.e. at “bottom dead center”).

When a driving torque T is applied to the wheel (Fig. 4(a)), the node bends due to low flexural stiffness at the root. Then, the high friction strip (the orange colored region in the bottom view) contacts the ground, generating a friction force $F_f = \mu_h W$. The material for high friction strip is chosen such that the friction coefficient μ_h is high, and therefore the driving force F_f is large.

When a force N_s is applied to the wheel in lateral direction (Fig. 4(b)), for example by forces caused by orthogonally-oriented driven wheels on the vehicle, the node bends laterally due to low flexural stiffness at the root. Then, the low friction region of the node contacts the ground and the high friction strip does not. In this scenario, the wheel generates a friction force $F_s = \mu_l W$. The material for low friction region is chosen such that the friction coefficient μ_l is low, and therefore the sliding force F_s is small.

Assuming a vehicle employing four wheels in an orthogonally-oriented configuration (see Fig. 5), the net traction force N_s generated by two wheels (i.e. right and left) is:

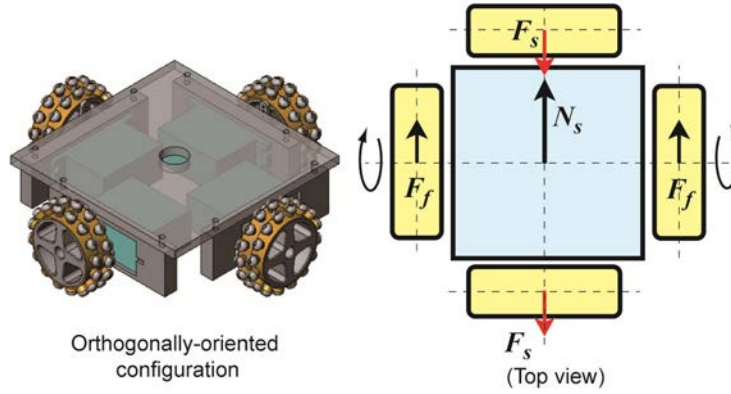


Fig. 5 Vehicle in orthogonally-oriented configuration

$$N_s = 2F_f = 2\mu_h W \quad (1)$$

Then, comparing N_s to the sliding forces $F_s (= \mu_l W)$ due to the low friction material of the other two wheels (i.e. front and rear):

$$N_s - 2F_s = 2\mu_h W - 2\mu_l W = 2W(\mu_h - \mu_l) \quad (2)$$

The properties for high/low material are chosen such that they have a relationship as $\mu_h > \mu_l$. Therefore, from Eq. (2), $N_s > F_s$ is realized, and the vehicle can achieve omnidirectional mobility.

Comparing the mechanics of omnidirectional motion for a vehicle with conventional wheels to a vehicle with the proposed wheels, a vehicle with conventional wheels realizes an anisotropic friction effect through the use of slender rollers, as noted in Section 1. On the other hand, the proposed wheel exploits distinct friction properties of two distinct materials, and thus “tribologically” achieves an anisotropic friction effect.

3. PROTOTYPE OF OMNIDIRECTIONAL ROBOT AND EXPERIMENTAL TEST

3.1 Omnidirectional Robot Prototype with Proposed Wheel

Fig. 6 shows a physical prototype of an omnidirectional mobile robot that employs four of the proposed wheels in an orthogonally-oriented configuration. The dimensions of the robot are 159 mm x 159 mm, and weighs 690.0 g. Each proposed wheel is actuated by servomotors. Power for the motors is supplied by four AA batteries. The robot is operated by an on-board micro controller, which sends drive signals to each servo to execute predefined omnidirectional motions (i.e. forward, back, or laterally, resulting in square motion, diagonal motion and others).

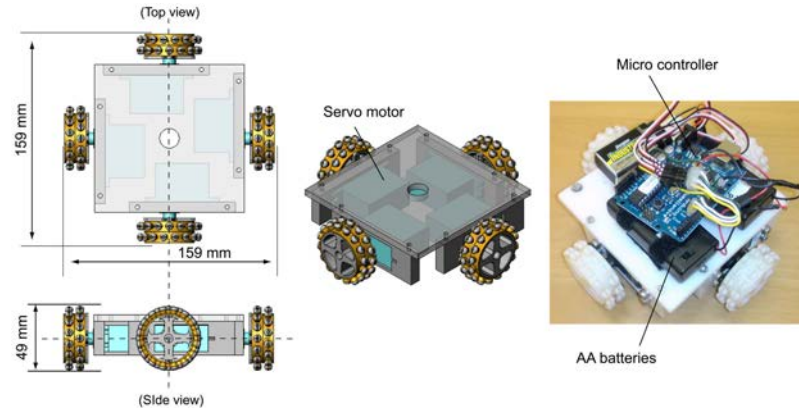


Fig. 6 Prototype of the omnidirectional mobile with proposed wheel

3.2 Performance Test

Two experimental tests, omnidirectional mobility test and traction performance tests were conducted to study the motion performance of the proposed wheel. In the tests, two conventional omnidirectional wheels are used for performance comparison: Omniwheel and Transwheel®, as shown in Fig.1. The outer diameter of these wheels is the same as the proposed wheel.

3.2.1 Omnidirectional Mobility

In these tests, the vehicle is controlled to repeatedly move along a square (i.e. right, forward, left, and back) at a fixed wheel velocity for a fixed amount of time, and the distance traveled is measured using camera images captured from above. Then, the omnidirectional mobility of the wheels (the proposed wheel, Omniwheel, and Transwheel) is compared based on the distance traveled.

The snapshots of the test are shown in Fig.7. The vehicle with the proposed wheels can achieve omnidirectional motion, and the distance traveled is 92.8 % of that with Transwheel, and 99.0% of that with Omniwheel. This performance is likely to vary depending on the material that the vehicle is traveling on, since the friction coefficient is material dependent. However this test serves as a proof of concept of the utility of the proposed wheels.

3.2.2 Traction Performance

The slope climbing test was conducted to evaluate the traction performance of the proposed wheel. In this test, the test bed is controlled to maintain its wheel driving velocity, and measure the slope angle θ_s at which the test bed stalls. In this case, the maximum traction force generated by the wheels is equal to the tangential component of the vertical load of the test bed, namely $W \sin \theta_s$.

Fig. 8 shows the snapshots of the traction performance test. The slope surface is plywood. From the results, the proposed wheel generates traction force ($=W \sin \theta_s$) approximately 3.2 times larger than that of Transwheel, and 2.1 times larger than Omniwheel. The conventional ones are made of only low friction material, and because of this, the friction coefficient in longitudinal direction of wheel becomes relatively low, resulting in the low traction force. However, the proposed wheel has bendable node with high friction materials, which can stick to the ground and generate large traction force. This high traction performance of the proposed wheel is significant improvement over the conventional wheels.

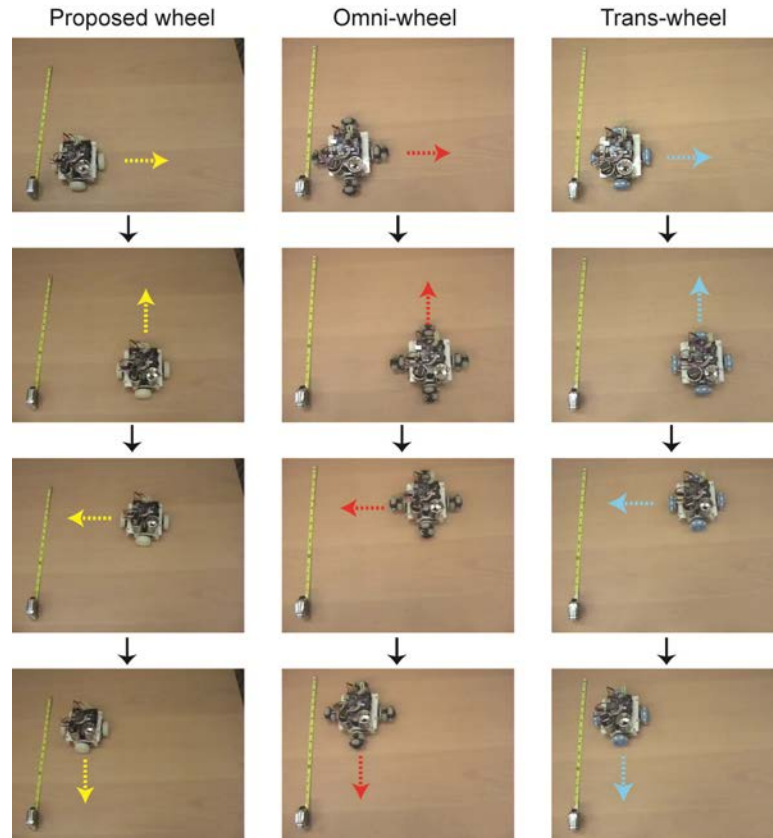


Fig. 7 Omnidirectional mobility test

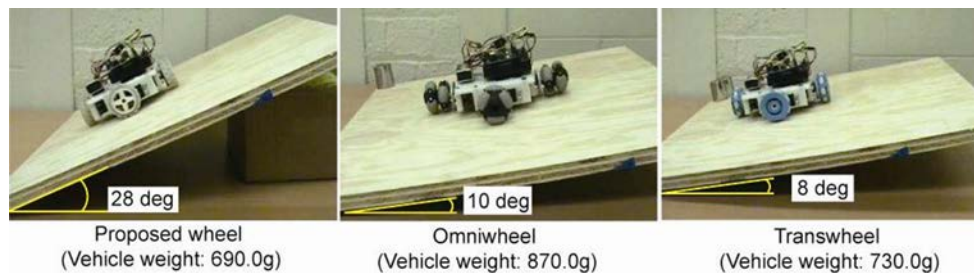


Fig. 8 Traction performance test

4. CONCLUSION— DESIGN OF AN OMNIDIRECTIONAL UGV BASED ON ANISOTROPIC FRICTION

In this report, a novel design of wheel for omnidirectional vehicle utilizing anisotropic friction properties has been described. The proposed wheel has a series of bendable nodes on its circumference, the surface of which is covered with materials having differing friction property.

From the experimental results presented in Section 3.2, it has been confirmed that the vehicle with the proposed wheels has similar omnidirectional motion characteristics to a vehicle with conventional omnidirectional wheels. The proposed wheel can also grip to the ground with its high friction property, enabling the vehicle to generate much larger traction force than conventional wheels do. Thus, a significant improvement by the proposed wheel over the conventional omnidirectional wheels is the high traction performance while having equivalent

omnidirectional mobility. In addition, the proposed wheel consists of single, moldable element and no mechanical components such as bearings and axles, which allows for a reduction in design complexity and potential for decreased production cost and increased robustness.

The proposed wheel is applicable in any situations in which conventional wheels have been used, but in particular, the proposed one will be possible to enhance a mobility performance of an omnidirectional vehicle requiring both high traction performance and omnidirectional motion (i.e. for vehicle towing or for environment such as sloped ground).

ACKNOWLEDGMENT

This material is based upon work supported in part by the U. S. Army Research Laboratory and the U. S. Army Research Office under contract/grant number W911NF-09-1-0334. The authors would like to thank Malik Hansen of Boston Dynamics for introducing the idea of multi-material surfaces for robotic mobility.

REFERENCES

- [1] Blumrich, J., "Omnidirectional Wheel," US Patent 3,789,947 (1974).
- [2] Smith, R., "Omnidirectional Vehicle Base," US Patent 4,715,460 (1987).
- [3] Fujisawa, S., Ohkubo, K., Yoshida, T., Satonaka, N., Shidama, Y., and Yamaura, H., "Improved Moving Properties of an Omnidirectional Vehicle Using Stepping Motor," *Proc. the 36th Conf. on Decision and Control*, San Diego, CA, pp.3654–3657 (1997).
- [4] Williams, R., Carter, B., Gallina, P., and Rosati, G., "Dynamic Model with Slip for Wheeled Omni-Directional Robots," *IEEE Trans. on Robotics and Automation*, vol. 18, no. 3, pp. 285-293 (2002).
- [5] Ilon, B., "Wheels for a course stable self-propelling vehicle movable in any desired direction on the ground or some other base," US Patent 3,876,255 (1975).
- [6] Muir, P., and Neuman, C., "Kinematic Modeling for Feedback Control of an Omnidirectional Wheeled Mobile Robot," in *Proc. the 1987 IEEE Int. Conf. on Robotics and Automation*, Raleigh, NC, pp. 1772–1778 (1987).
- [7] Agullo, J., Cardona, S., and Vivancos, J., "Kinematics of vehicles with directional sliding wheels," *Mechanism and Machine Theory*, vol. 22, issue 4, pp. 295-301, (1987)
- [8] Gferrer, A., "Geometry and kinematics of the Mecanum wheel", *Computer Aided Geometric Design*, vol. 25, issue 9, pp. 784-791 (2008)
- [9] Cheng, N., Ishigami, G., Hawthorne, S., Chen, H., Hansen, M., Telleria, M., Playter, R., and Iagnemma, K., "Design and Analysis of a Soft Mobile Robot Composed of Multiple Thermally Activated Joints Driven by a Single Actuator," in *Proc. of the 2010 IEEE Int. Conf. on Robotics and Automation*, Anchorage, AK, pp. 5207–5212, (2010).

SUPPORTING ONLINE MATERIALS

- 1) Kornylak Corporation, Transwheel®, <http://www.kornylak.com/wheels/wheels.html>
- 2) AirTrax, <http://www.airtrax.com/>
- 3) Connex500™ Multi-Material 3D Printing System, http://www.objet.com/3D-Printer/Objet_connex500/

1.0 INTRODUCTION—EXPERIMENTAL METHODS FOR WHEEL-TERRAIN INTERACTION MODELING

Robotic vehicles are frequently deployed in unwelcoming, hazardous environments. From military robots to planetary rovers, vehicle mobility is a key aspect of mission success. Several models for traction modeling of tracked and wheeled vehicles have been developed in the past decades; however, a comprehensive understanding of soil behavior under running gear is still missing to date. The work of Bekker and Wong, which began in the 1950's, has laid the foundation for modern terramechanics. The application of classical results from plasticity theory, combined with semi-empirical formulations, has provided satisfactory solutions to the problem of mobility modeling for large, heavy vehicles. However, the expanded use of lightweight vehicles (especially man-portable robotic vehicles) has called for a new effort in modeling vehicle-terrain interaction problems. In fact, some researchers have suggested that classical models are of questionable utility when applied to vehicles one order (or more) of magnitude smaller than tanks, Humvees, large trucks, and the like [1].

This report will describe novel experimental methods aimed at understanding the fundamental phenomena governing the motion of lightweight vehicles on dry, granular soils. A single-wheel test rig is used to empirically investigate wheel motion under controlled wheel slip and loading conditions on a sandy, dry soil (Figure 1). Test conditions can be designed to replicate typical field scenarios for lightweight robots, while key operational parameters such as drawbar force, torque, and sinkage are measured. This test rig enables imposition of velocities, or application of loads, to interchangeable running gears within a confined soil bin of dimensions 1.5 m long, 0.7 m wide, and 0.4 m deep. This allows testing of small-scale wheels, tracks, and cone or plate penetrators.

The soil under investigation has been fully characterized with a series of direct shear tests (ASTM D3080) and penetration tests. Direct shear tests were performed to estimate soil shearing parameters such as cohesion, angle of internal friction, and shear modulus. Penetration tests, although not standard tests, were performed to evaluate 'Bekker' parameters, necessary for characterization of pressure-sinkage behavior of the soil under the methodology described by Wong [2].

The aforementioned experiments represent a typical experimental approach to macro-scale characterization of wheel-soil interaction. However, the application of classical terramechanics model to lightweight vehicles may potentially show discrepancy between experiments and predictions, warranting the development of new methods to probe the fundamental mechanics of a small robot's interaction with soil.

To this end, two additional experimental methodologies have been developed. The first relies on high-speed imaging of the wheel-soil interface and the use of particle image velocimetry (PIV) to measure micro-scale terrain displacement (Figure 1). This methodology, although confined to plane strain cases, allows measurement of soil flow velocities, and observation of the formation of shear bands beneath the wheel/track. Though this method does not explicitly permit calculation of the velocities of individual soil particles, it does allow estimation of a regularly-spaced velocity field in the soil. While such visualization techniques have been widely employed in the field of experimental fluid mechanics, their application to the study of soils is a relatively new development [3, 4].

The second experimental methodology is intended to complement the PIV-based soil kinematics analysis. It employs a custom force sensor array located at the wheel-terrain interface. The force sensors are strain gauge-based flexural elements with interchangeable interface surfaces that are designed for integration with wheels or other running gear. The sensors allow explicit measurement of normal and shear forces (and, therefore, estimation of normal and shear stresses) at numerous discrete points along the wheel-soil interface. When coupled with PIV-derived kinematic data, this allows for a richer characterization of soil loading and failure regimes than would be possible with either kinematic or pressure information alone. In particular, this experimental methodology allows joint visualization of the soil displacement in the bulk soil medium, and measurement of shear and normal stress at points along the interface. This could lead to development and validation of novel constitutive relations describing soil behavior under loading imposed by running gear.



Figure 1: CAD drawing of the terramechanics testbed showing the imager for PIV experiments (top). Actual PIV setup with the high speed camera and two flood lights (bottom)

Experiments have shown that soil failure, at certain slip levels, is qualitatively different under cases of low vertical load (which is typical for lightweight robots) compared to cases of high vertical load (typical for large ground vehicles). Also, soil flow patterns have been observed to exhibit periodic failure phenomena, giving rise to interesting features such as surface ripple formation. These results, obtained through PIV analysis, provide deeper understanding of the mechanics of traction generation. Experimental measurements gathered by these test methodologies are compared against the results from well-established semi-empirical models, to understand limitations of these models and propose modifications and improvements.

2.0 SINGLE WHEEL TESTBED DESCRIPTION

The Robotic Mobility Group at MIT has designed and fabricated a multipurpose terramechanics rig based on the standard design described by Iagnemma [5]. The testbed is pictured in Figure 1 and is composed of a Lexan soil bin surrounded by an aluminum frame where all the moving parts, actuators and sensors are attached. A carriage slides on two low-friction rails to allow longitudinal translation while the wheel or track, attached to the carriage, is able to rotate at a desired angular velocity. The wheel mount is also able to translate in the vertical direction. This typical setup allows control of slip and vertical load by modifying the translational velocity of the carriage, angular velocity of the wheel, and applied load. Horizontal carriage displacement is controlled through a toothed belt, actuated by a 90W Maxon DC

motor while the wheel is directly driven by another Maxon DC motor. The motors are controlled thorough two identical Maxon ADS 50/10 4-Q-Dc servoamplifiers. The carriage horizontal displacement is monitored with a Micro Epsilon WPS-1250-MK46 draw wire encoder while wheel vertical displacement (i.e., sinkage) is measured with a Turck A50 draw wire encoder. A 6-axis force torque ATI Omega 85 transducer is mounted between the wheel mount and the carriage in order to measure vertical load and traction generated by the wheel. Finally, a flange-to-flange reaction torque sensor from Futek (TFF500) is used to measure driving torque applied to the wheel. Control and measurement signals are handled by a NI PCIe-6363 card through Labview software.

The rig is capable of approximately 1 meter of horizontal displacement at a maximum velocity of approximately 120 mm/s with a maximal wheel angular velocity of approximately 40 deg/s. The bin width is 0.6 meters while the soil depth is 0.16 meters. Considering the wheel sizes and vertical loads under study, these physical dimensions are sufficient for eliminating boundary effects. Moreover, the same testbed, with some adaptations, can be used to perform soil penetration tests and analyze different running gears (e.g., both wheels and tracks).

For the experiments described in this report, the Mojave Martian Simulant (MMS) was employed as a test medium [6]. MMS is a mixture of finely crushed and sorted granular basalt intended to mimic, both at chemical and mechanical level, Mars soil characteristics. MMS particle size distribution spans from micron level to mm level with 80% of particles above the 10 micron threshold.

3.0 GRANULAR SOIL PARTICLE IMAGE VELOCIMETRY

Particle image velocimetry (PIV) describes an experimental method, based on image cross-correlation techniques, used for the determination of flow velocity fields. The use of PIV for the calculation of fluid velocities initially emerged in the 1980's [7, 8]. Since then, PIV has played an important role in many fluid mechanics investigations [9]. Two of the main advantages of PIV over other methods for the measurement of velocity (e.g. hot-wire-velocimetry, Pitot tubes etc.) are that it is non-intrusive, and allows for relatively high resolution measurements over an extended spatial domain.

During fluid-based PIV analysis, the fluid is typically seeded with marker particles that refract, absorb, or scatter light, have a high contrast with the fluid, and do not interrupt the fluid flow. Imaging is performed at high speed over an area of the flow illuminated by a light source, typically a pulsed laser. Captured images are post-processed with algorithms that perform frame-to-frame feature tracking and calculation of flow velocity fields.

PIV is also a useful method for measuring soil motion, with the notable constraint that soil is typically observed through a glass sheet, limiting the resulting analysis to plane strain scenarios. The natural granular texture of soils often generates an intensity pattern that can be readily traced by PIV-algorithms, without the use of marker particles. Also, incandescent light can generally be used for illumination.

Granular PIV has recently been employed in several applications, including the analysis of grains in converging hoppers [10], study of flowing granular layers in rotating tumblers [11], investigation of granular avalanches [12], analysis of soil motion caused by the movement of animals [13], the study of burrowing behavior of razor clams [3], and in the study of wheel-soil interaction [4, 14]. The analysis of soil motion beneath a driven wheel via quantitative analysis of successive temporal images was first introduced by Wong [15]. However, the experimental capabilities of

that study did not allow for high-speed image capture, limiting the accuracy and practical utility of the method.

Soil motion analysis can be broken down into four main steps: 1) image acquisition, 2) image pre-processing, 3) image cross-correlation (PIV), and 4) velocity field post-processing. These steps are briefly described here, and methods for parameter selection are presented. Note that in the following, the Matlab-based PIVlab software is employed [16].

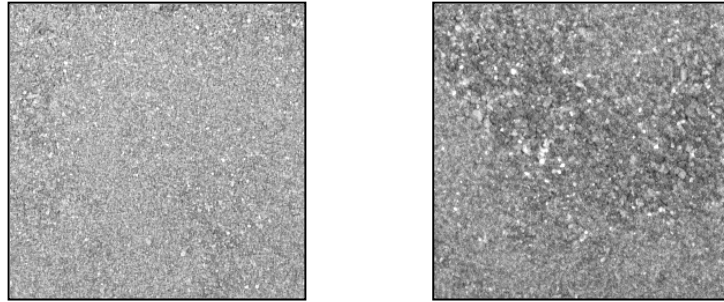


Figure 2: Examples of soil natural textures.

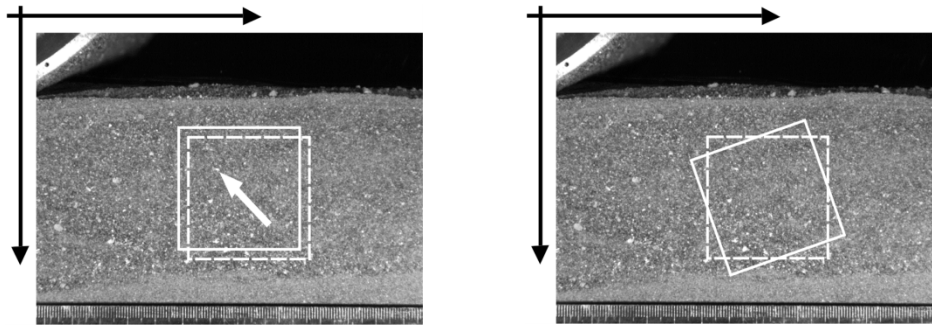


Figure 3: Two examples of image canonical transformations used to evaluate PIV settings. Nine image transformations for coarse and fine soil textures were used to evaluate PIV accuracy

PIV IMAGER CONFIGURATION

The accuracy of PIV strongly depends on the quality of the captured images. For these experiments the testbed was fitted with a 2.54 cm thick tempered glass wall while the running gear was operated flush against this surface (see Figure 1). Both wheels and tracks have been analyzed with this testbed, however this report describes results from rigid wheel testing.

Image sets for the PIV measurement were captured with a Phantom 7 high-speed camera. The Phantom 7 is able to record grayscale images at the maximum resolution of 800x600 pixels at a maximum frame rate of 6688 fps. The camera was placed perpendicular to the front glass wall (see Figure 1) at a distance of 52 cm, while the focal length was set to 77 mm (a zoom lens was used) resulting in an image capture region of approximately 15 x 11.25 cm. It should be noted that determination of image capture region size is largely dictated by the particular experimental conditions. Here, the image capture region was chosen in order to conservatively bound the region of soil that would undergo motion when subjected to wheel passage on the soil surface. Two 250W Lowel Pro-Light photography flood lights were placed on either side of the camera at an angle of 45° towards the object plane, and provided approximately homogeneous illumination of the soil. By using

two laterally positioned light sources, reflections and shadows can be significantly diminished.

PIV IMAGE PREPROCESSING

The performance of PIV cross-correlation algorithms generally improves when images are of high contrast, feature dense, and have low noise. In practice, images are subject to nonuniform illumination, image sensor noise, and lack of natural contrast in the granular material, all of which can degrade PIV algorithm performance. Various image pre-processing methods were investigated to understand their effect on algorithm performance. These include commonly-employed algorithms such as contrast limited adaptive histogram equalization, high pass filtering, and clipping and intensity capping.

To systematically investigate the effect of these preprocessing methods on PIV algorithm performance, test image segments of the Mars regolith simulant with dimensions 256 x 256 pixels were captured, then synthetically deformed in canonical directions. Since the particle distribution in the soil under investigation is locally inhomogeneous, two distinct image segments were captured in order to adequately represent typical apparent grain distributions in the MMS simulant. This resulted in one image populated by relatively large grains and one populated by relatively small grains (Figure 2). Synthetic deformation of the image was performed as a means of generating a ground truth for cases of linear translation (1-4 pixels in both horizontal, vertical, and diagonal directions), rotation (1-8 degrees in clockwise and counter-clockwise directions), shear (1-4 pixels of relative motion between upper and lower image halves), and simple shear (1-4 pixels of motion of upper edge of image) (Figure 3). Since the pixel shift for each deformation was controlled, this methodology allowed quantitative evaluation of PIV algorithm results. An error metric was computed by computing the average difference, over all points in the PIV velocity field, between the velocity vector calculated through PIV and the true velocity vectors.

PIV IMAGE CROSS-CORRELATION

In PIV, images are divided into small interrogation windows (IW) and then analyzed to compute the probable displacement between successive images for each IW using cross-correlation techniques. This results in an equally spaced field of calculated velocity vectors. The probable displacement is determined by using the cross-correlation function:

$$R_{II'}(x, y) = \sum_{i=-K}^K \sum_{j=-L}^L I(i, j) I'(i + x, j + y) \quad (1)$$

where I is the intensity of the first image and I' the intensity of the second image. A detailed description of PIV theory can be found in [17]. Particle density, image resolution, and IW size are interconnected parameters that must be carefully selected to optimize performance. Based on experimental investigations, Keane and Adrian [18] defined empirical rules for optimal PIV setup. The reader is referred to the above report for more details. For the results presented here, the following settings were employed: 25 fps, final IW size of 16, CLAHE filtering with kernel size of 40 pixels. A more complete description of the PIV settings and analysis is presented in [19].

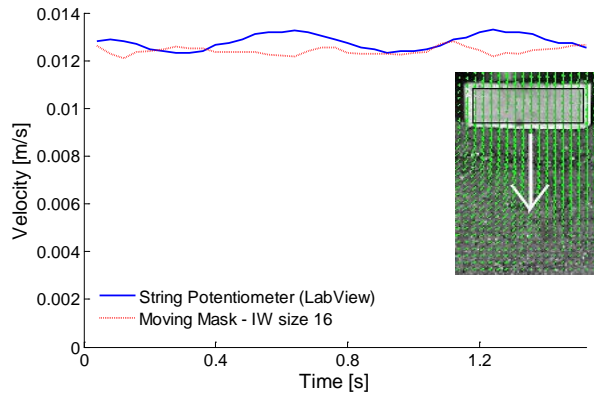


Figure 4: Comparison of velocity calculated through PIV and measured with a draw wire encoder.

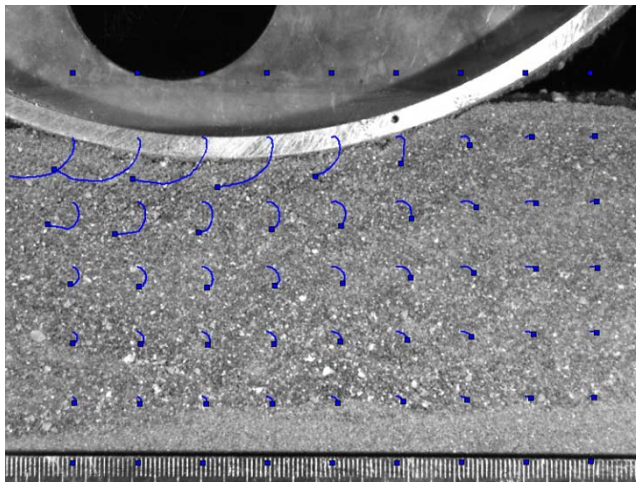


Figure 5: Soil trajectories calculated from velocity field obtained through PIV analysis. Visual inspection showed that PIV yielded tracking of soil regions on the order of 0.5-1 mm after translations of several centimeters.

VELOCITY POST-PROCESSING

FIELD

The raw velocity field produced by PIV calculations can contain spurious vectors (outliers). These outliers can be caused by noise, inappropriate interrogation settings, and accidentally matched patterns. Hence, to improve results, rejection of these outliers and interpolation of missing data points can be performed in a post-processing stage through filtering. Filters for the rejection of outliers can primarily be divided into two separate classes: global and local methods. Global filters commonly employ a simple thresholding method, with the threshold value selected by an operator with empirical or theoretical domain knowledge. If elements of the velocity field exceed the threshold, this element is removed from the results. Local filters are primarily based on relative differences between surrounding vectors, rather than absolute values. A local filter calculates the mean and standard deviation of the velocity for a selected kernel size around each vector. If the velocity exceeds certain thresholds, the vector is

rejected. For the results presented here, a 5x5 kernel with a threshold of 8 times the standard deviation was used for post-processing.

VALIDATION AND VERIFICATION

The synthetically deformed image was determined to be a useful ground truth for determining appropriate PIV operational parameters. However, validation of the PIV algorithm performance was also pursued on two sets of test data that were physically relevant to the running gear-soil interaction case.

The first test consisted of calculating the velocity via PIV of a 2.5 cm thick steel plate performing a soil penetration test. The ground truth velocity of the plate was externally measured by numerically differentiating the output of the draw wire encoder (which nominally provides a position measurement). To obtain a plate velocity measure from PIV, an average of the velocities was computed over a rectangular region of interest aligned with the moving plate.

Figure 4 shows a comparison of the plate velocity as determined from PIV calculations and the velocity measured by the draw wire encoder. The average percent error (for the best settings) between these measurements was below 1%. It should be noted that, for this test case, the PIV algorithm is not performing calculations on the granular soil, but rather the steel plate edge. However, this test remains of interest since the soil in contact with the plate necessarily moves at the same velocity.

The second test consisted of calculating the time evolution of motions of discrete features associated with MMS simulant soil beneath a driven rigid wheel. Trajectories $s(t)$ are calculated for a grid of 9 x 6 regions of interest over the soil area. The time evolution of the positions of the center of the regions of interest was computed by integrating the velocities with a fourth order Runge-Kutta method.

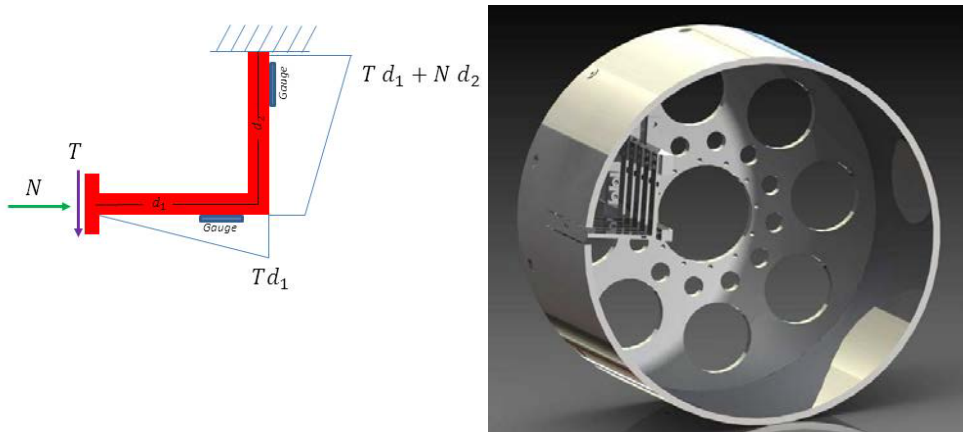


Figure 6: Working scheme of the custom force sensor for interfacial stress measurement (top left). Five sensors are distributed from the wheel median axis to the wheel edge (bottom left). Sensors are rigidly connected to the wheel hub (right)

$$s(t) = \int_0^t v(t) dt \quad (2)$$

The motion of these tracked regions were compared to trajectories of individual soil particles that are large enough to be manually tracked from frame to frame, thereby providing a qualitative performance evaluation. Also, the calculation of feature trajectories is useful for illustrating soil flow when subjected to various loading conditions.

Figure 5 displays the trajectories computed while the wheel was advancing at 17 deg/s with 30% slip. Note that the area above the soil surface was masked during pre-processing, and hence these features remain at their original location. The squares show the final position of the tracked features and the lines represent the motion evolution. Manual inspection showed that the selected PIV yielded tracking of soil regions in the order of 1-2 pixels, corresponding to 0.5-1 mm after translations of several centimeters.

4.0 WHEEL-TERRAIN INTERFACE FORCE SENSOR DESCRIPTION

Measurement of the normal and shear stress acting on a moving wheel is important for empirical testing and validation of models describing interfacial

phenomena. While numerous COTS sensors exist for measuring pressure [20], the authors are unaware of any available sensors that can measure both pressure and shear stress, at a scale and resolution suitable for investigation of the interaction mechanics of small, lightweight vehicle running gear and deformable soil.

Therefore, a custom sensor array was designed and fabricated (Figure 6). Each sensor is a solid-state L-shaped aluminum flexure instrumented with two full bridge strain gages. The sensor is mounted rigidly to the running gear, and its interface element is exposed to the soil. The interface element is generally subjected to normal (N) and shear (T) loading. These forces cause the flexure elements to deflect in a linear elastic manner. From measured deflection, and given prior calibration data, the applied forces can be uniquely computed. (Axial strain is intrinsically rejected by the full bridge configuration.) Stress can then be inferred assuming uniform pressure distribution over the known sensors' head area.

Sensors are mounted on the surface of a 26 cm diameter rigid aluminum wheel (see Figure 6). Note that a twin wheel, without the array, was used for PIV testing. Five sensors have been fabricated and integrated in a linear array spanning one half of the wheel width (i.e. from one edge to the center of the wheel). Sensors were first calibrated by applying test weights of 100, 200, and 500 grams in the normal and tangential direction. Measurement linearity error, across all the sensors, was found to be below 3%.

The sensor array is extremely sensitive to misalignment and thus an uneven contact patch profile can easily unbalance the output reading. To ensure accurate alignment, sensors alignment was verified after every 5 tests, by driving the wheel over a flat, rigid, aluminum plate covered with a thin layer of polyurethane foam in order to verify that the sensor output was uniform. Due to the difficulty in precisely controlling soil preparation, each test was repeated at least 15 times. In fact, local soil density variation, inhomogeneity (due to non-uniform distribution of larger grains, for example), and surface unevenness all were observed to affect measurement output. The 15 trials highlighted test variability and were analyzed to detect outliers and eventually remove tests where anomalies were detected.

5.0 SOIL PROPERTIES

Characterization of the soil under investigation is a necessary step for any terramechanics investigation. Detailed chemical composition, particle size distribution, and shearing properties of the MMS simulant under investigation can be found in [6]. However, pressure-sinkage properties (i.e. Bekker's parameters) for the soil were unknown, and therefore a series of plate penetration tests were performed.

Since the wheel has a width of 0.13 m and a nominal contact patch length of 0.05 m (estimated assuming nominal conditions of $F_z = 100$ N and low slip) three rectangular plates with the following dimensions were selected: 0.13 m x 0.03 m, 0.13 m x 0.05 m, and 0.13 m x 0.07 m.

Each plate was mounted on a linear actuator, which was anchored to the testbed and then pushed perpendicularly into the soil while the vertical load and penetration length (i.e. sinkage) were measured with a load cell and a draw wire encoder, respectively.

For each plate, tests were repeated 15 times. Between each test, soil was manually agitated and then re-leveled. Figure 7 shows an example of the data collected. Test-to-test variation was observed, but was not considered unusual due to the nondeterministic nature of soil testing.

The scope of the tests was to fit experimental data to Bekker's pressure-sinkage equation [21]:

$$p = \left(\frac{k_c}{b} + k_\phi \right) z^n \quad (3)$$

where p is pressure, z is sinkage, b is plate width (3,5,7 cm) and $\{k_c, k_\phi, n\}$ are the parameters under investigation. Adopting the fitting methodology presented in [2] it was noted that $k_{eqb} = \left(\frac{k_c}{b} + k_\phi \right)$ is strongly correlated with n as shown in Figure 8. This correlation necessarily results from the tests having similar amounts of deviation from an exponential curve. While this effect is solely an artifact of experimental estimation, it is still undesirable because it inhibits k_{eqb} from being estimated independently.

The problem is mitigated through adoption of Reece's equation [22] for pressure-sinkage:

$$p = k_{eqr} \left(\frac{z}{b} \right)^n \quad (4)$$

Dimensional analysis of Reece's equation shows that k_{eqr} is not function of n (as it was in Bekker equation). Although variability is still substantial, k_{eqr} estimation becomes less dependent of n as can be seen in Figure 9.

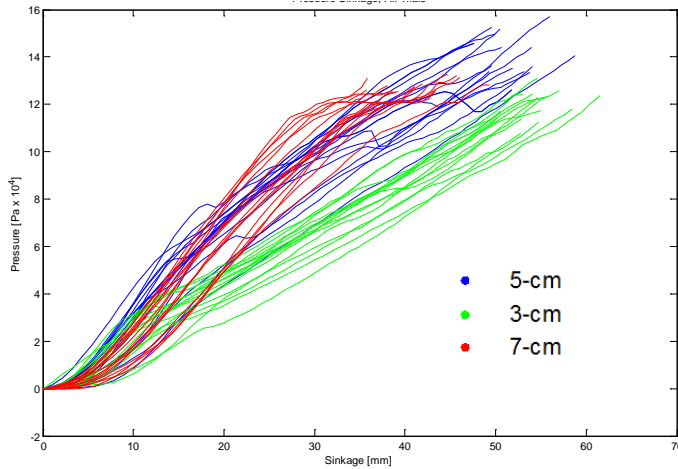


Figure 7: Penetration tests for rectangular plates with the following dimensions 0.13 m x 0.03 m, 0.13 m x 0.05 m, 0.013 x 0.07 m.

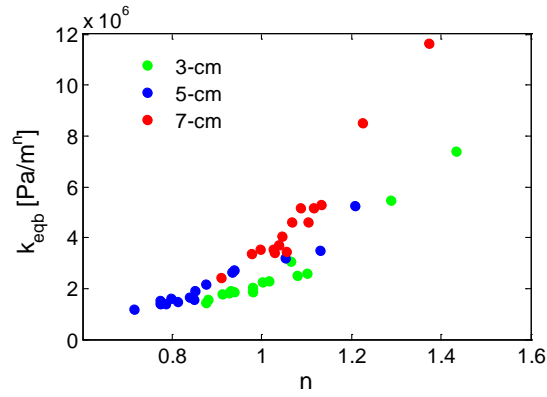


Figure 8: Strong correlation between soil parameters when Bekker equation is used.

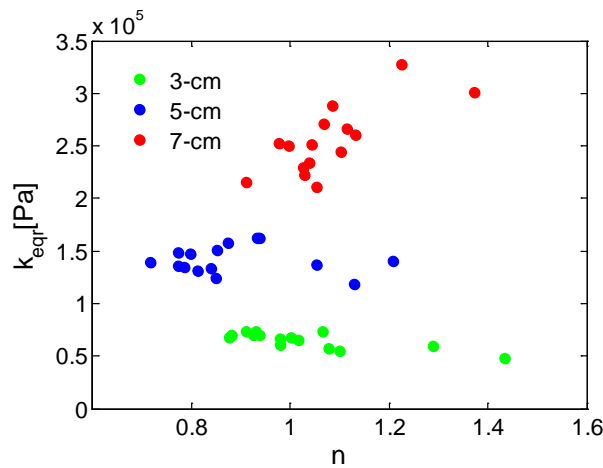


Figure 9: Correlation between soil parameters is mitigated when Reece's equation is used.

Penetration tests variability, even under laboratory controlled conditions, suggests that soil parameters should be derived from statistical distributions rather than deterministic values. A stochastic characterization of terrain properties is currently being investigated by the authors while the results presented in this report are still derived with the method established by Wong [2].

Two parameter sets are reported in Table 1. The set labeled '357' has been obtained considering the full dataset presented in Figure 7 while the set labeled "57" has been obtained only with the 5 cm and 7 cm plates, and truncating the data at 50 kPa. This was motivated by the fact that the wheel under investigation was expected to have contact patch length larger than 5 cm and normal stress distribution below 50kPa. The two datasets show how slightly modifying the design of experiments, can drastically change soil parameter calculation.

Table 1: Bekker soil parameters for the MMS soil.

Set	n	k_c [kN/m ⁿ⁺¹]	k_ϕ [kN/m ⁿ⁺²]
357	0.99	-55	4584
57	1.4	846	6708

6.0 RESULTS AND DISCUSSION

Experiments with the PIV and stress sensor experimental methodologies were conducted separately. For PIV tests, a smooth wheel, coated with MMS simulant (to ensure sufficient interfacial friction) was run flush against a glass wall. For stress sensor tests, a wheel of exactly the same diameter, and again covered with MMS simulant, was run in the middle of the soil bin. Soil was loosened, mixed, and leveled between each test, in an attempt to achieve uniformly loose, homogenous conditions.

Both type of tests were run at approximately 100N of vertical load and for slip levels ranging from -70% to 70% (for PIV tests, slip was limited to $\pm 30\%$). For PIV tests the wheel velocity was fixed at 17 deg/s while for stress sensor tests angular velocity was reduced to 8.5 deg/s to improve measurement quality. (The horizontal carriage velocity was modified to achieve the desired slip level.) For both types of tests, it was first ascertained that velocity did not have an influence on wheel performance. The operational conditions described above were chosen because they are close to those of the Mars Exploration Rover, a successful lightweight robotic vehicle.

A substantial amount of data was collected and cannot be comprehensively described in this report. Instead, a small number of initial results are presented.

PIV Analysis

Analysis of PIV data was performed to qualitatively analyze soil motion (a quantitative analysis would have required to investigate the complex mapping between stress and displacement, this goes beyond the scope of this preliminary study). Figure 10 presents a snapshot of a 30% slip test, and displays the following information from top-left-clockwise: velocity vectors, u-velocity, v-velocity, and velocity magnitude. Analysis of such images can provide insights into the spatial distribution of soil velocity under running gear, and can vary dramatically for such cases as slip, skid, free-rolling wheels, braked wheels, etc.

Decomposition of this flow field can yield useful insight into soil shearing (which occurs primarily in the horizontal direction, see upper right image) and soil compaction phenomena (which occurs primarily in the vertical direction, see lower right image). Here, a blue region corresponds to no motion while red indicates a maximum velocity. Analysis of these images shows that soil flow remains attached to the wheel rim. Moreover, for low vertical load (such as the one utilized during experiments) it was observed that two separate slip failure lines did not evolve, as predicted by classical theory [23, 24]. This finding is interesting because according to [23], the maximum stress occurs where the soil flow separates. The absence of flow separation, however, does not prevent stress to reach a maximum (see Figure 11).

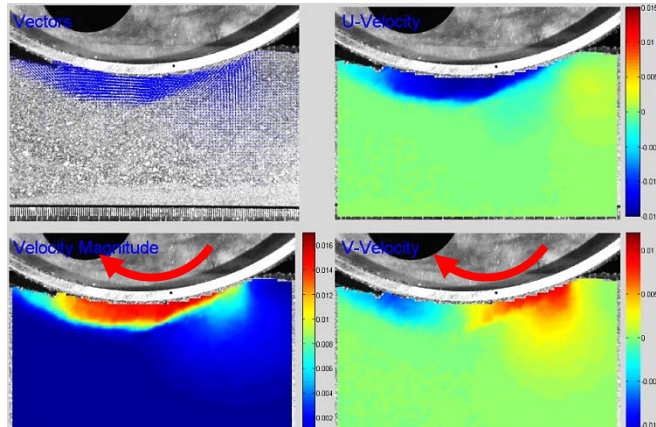


Figure 10: A snapshot of a 30% slip test. Nominal vertical load was 100N and wheel angular velocity of 17 deg/s. From top-left-clockwise: velocity vectors, u-velocity, v-velocity, and velocity magnitude.

For slip levels below $\pm 10\%$, the soil was not observed to develop a significant shearing plane. Another phenomenon that was clearly highlighted by PIV analysis is the periodic nature of soil failure. For slip level above 10-15%, soil often exhibits a periodic loading cycle of alternating compaction and shearing, which results in discontinuous failure of the soil mass. This has two direct consequences: oscillations in drawbar pull readings and creation of ripples behind the wheel. Note that while these effects have been noted previously, they have been typically assigned to the effect of grousers. However, these effects are present even for smooth wheels, without grousers.

PIV data can be useful for investigation of constitutive models for granular materials, and for development of reduced order models based on soil displacement predictions. An important consideration to bear in mind when examining flow fields like the one presented in Figure 10 is that the relationship between stress and displacement is typically complex, and one must avoid the temptation to directly (i.e., proportionally) correlate velocity magnitudes with stress magnitudes.

For this reason, direct stress measurement of shear and normal forces, and inferences of associated stresses, at the wheel-terrain interface yields valuable information about the traction generation process.

Interface Force Sensor Analysis

Classical terramechanics methods rely on the estimation of the stress distribution under the wheel. The ability to directly measure such quantities allows for a one-to-one comparison of model prediction and experimental reality.

Analysis of stress distribution across a (symmetric) half-wheel width shows that boundary effects become more pronounced as slip increases (see Figure 11). In particular, stress at the wheel edge was observed to be relatively high for positive slip and relatively low for negative slip. It is hypothesized that this effect is caused by soil transport phenomena: for positive slip, soil in the center of the wheel is transported behind the wheel at higher rate than the soil at the wheel edges, which causes the wheel edges to bear proportionally more of the total normal wheel load. On the contrary, for negative slip, soil accumulated in front of the wheel creates a thicker layer under the wheel median axis, causing higher stress in the center.

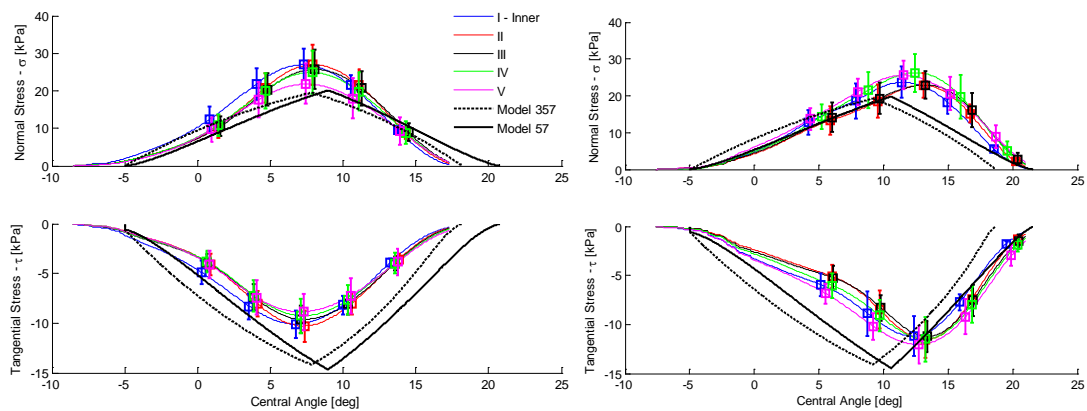


Figure 11: Stress distribution for 10% (left) and 30% (right) slip compared with analytical

model from Wong and Reece [26, 27]. Two soil parameter sets, presented in Table 1, were tested. The difference between the two parameter sets, although significant, it is not dramatic. Normal stress is slightly underestimated while tangential stress is significantly estimated. Tangential stress, however, is primarily based on soil shear properties which were obtained in [29].

For higher loading conditions, Onafeko and Reece [25] noted that normal stress decreases with increasing positive slip since an increasingly larger portion of vertical load is supported by shear stress (which contributes more to vertical load equilibrium because of increased sinkage). This was confirmed experimentally with the stress sensors.

Another interesting aspect of wheel stress distributions is the inversion of shear stress for negative slip conditions. This phenomenon was noted also by [25] and it is consistent with wheel-soil interaction kinematics: for negative slip, the wheel travels forward but simultaneously skids over the soil, generating a shear sign transition. Interestingly, PIV imagery does not show any soil separation or flow inversion where the shear stress changes sign.

In Figure 12, a direct comparison between the measured stress and stress predicted by the model originally proposed by Wong [26, 27] and Janosi and Hanamoto [28] is presented, using the experimentally determined soil parameters (two parameter sets, presented in Table 1, are compared). The normal stress distribution is underestimated and the error seems largely related with the location of maximum stress. Tuning of semi-empirical model parameters could allow better agreement.

The predicted shear stress, however, was found to be overestimated. Note that the shear modulus adopted to produce results in Figure 12 was calculated according to [29]. For larger (but arguably inaccurate) values of shear modulus, it may be possible to obtain better agreement between prediction and experimental data; however this raises a fundamental question about the validity of the assumptions behind the model. In fact, the model assumes that the soil is sheared for a distance corresponding to the amount of relative motion between the wheel and the soil. This assumption, as shown by PIV analysis, is likely erroneous, since the soil at the wheel-terrain interface stays attached to wheel rim, while failure physically occurs (in regular, periodic failure patterns) some distance away from the interface. Although $\{n, k_c, k_\phi\}_{357}$ and $\{n, k_c, k_\phi\}_{57}$ are significantly different (see Table 1), model predictions using these two sets are relatively close. This warrants further efforts in characterizing terrain variability and its influence on stress measurements variability.

CONCLUSIONS—Experimental Methods for Wheel-Terrain Interaction Modeling

Novel experimental methods aimed at understanding the fundamental phenomena governing the motion of lightweight vehicles on dry, granular soils were presented.

Aside from standard wheel experiments (i.e., measurements of drawbar force, applied torque, and sinkage during controlled slip runs) two additional experimental methodologies were introduced. The first relies on high-speed imaging of the wheel-soil interface and the use of particle image velocimetry (PIV) to measure micro-scale terrain kinematics. The second experimental methodology consists of a custom force sensor array located at the wheel-terrain interface. The sensors allowed explicit measurement of normal and shear forces (and, therefore, estimation of normal and shear stresses) at numerous discrete points along the wheel-soil interface.

Analysis of PIV data has shown that soil failure, at certain slip levels, is qualitatively different under cases of low vertical load (which is typical for lightweight robots) compared to cases of high vertical load (typical for large ground vehicles). Also, soil flow patterns have been observed to exhibit periodic failure phenomena, giving rise to interesting features such as surface ripple formation. Soil flow was observed to be always attached to the wheel rim and only one shear failure surface was observed. Soil usually exhibits compression in front of the wheel and then shears beneath it.

Stress measurements showed that, although only one shear failure surface is present, tangential stress goes through sign inversion for negative slip. Stress distribution, along the wheel width, is approximately uniform for low slip while edge effects become increasingly significant for higher slip levels. Although some observations regarding soil shear failure were not confirmed by PIV, classical methods (partially based on those observations) were able to capture main trends for a range of slip conditions. These results provide deeper understanding of the mechanics of traction generation and are expected to open new frontiers for more accurate, and predictive, lightweight vehicle mobility models.

Further investigation of small robot-terrain interaction mechanics will focus on extending these experiments to a wider range of vertical loads. This will provide a basis for validation of constitutive laws and the improvement of reduced-order models. Future work will also focus on stochastic characterization of terrain response and how underlying soil variability affects interfacial stresses modeling. In fact, even under laboratory controlled conditions, penetration plate tests have highlighted significant soil variability, warranting for statistical interpretation of experimental data.

REFERENCES

- [1] Meirion-Griffith, G., and Spenko, M., "A modified pressure-sinkage model for small, rigid wheels on deformable terrains," *Journal of Terramechanics*, Volume 48, Issue 2, pp. 149-155, April, 2011.
- [2] Wong, J.Y., "Data processing methodology in the characterization of the mechanical properties of terrain," *Journal of Terramechanics*, 17(1):13 – 41, 1980.
- [3] Winter, A., "Biologically Inspired Mechanisms for Burrowing in Undersea Substrates," Ph.D. Thesis, Massachusetts Institute of Technology, 2010.
- [4] Moreland, S., Skonieczny, K., Wettergreen, D., "Soil Motion Analysis System for Examining Wheel-Soil Shearing," 17th International Conference of the International Society for Terrain-Vehicle Systems, Virginia, USA, 2011.
- [5] Iagnemma, K., A Laboratory Single Wheel Testbed for Studying Planetary Rover Wheel-Terrain Interaction, Technical Report 01-05-05, Field and Space Robotics Laboratory, Massachusetts Institute of Technology, Cambridge, MA, 2005.
- [6] Beegle, L. W., Peters, G. H., Mungas, G. S., Bearman G. H., Smith, J. A., and Anderson, R. C., "Mojave Martian simulant: a new martian soil simulant," *Lunar and planetary science*, XXXVIII, 2007.
- [7] Adrian, R. J., "Statistical Properties of Particle Image Velocimetry Measurements in Turbulent Flow, *Laser Anemometry in Fluid Mechanics*," Lisbon: Instituto Superior Tecnico, 1988, pp. 115–29.
- [8] Keane, R. D., and Adrian, R.J., "Theory of Cross-Correlation Analysis of PIV Images," *Applied Scientific Research*, Vol. 49, Netherlands, 1992, pp.191-215.

- [9] Adrian, R. J., "Twenty Years of Particle Image Velocimetry," *Experiments in Fluids*, Vol. 39, 2005, pp. 159–169.
- [10] Sielamowicz, I., Błoński, S., and Kowalewski, T. A., "Digital Particle Image Velocimetry (DPIV) Technique in Measurements of Granular Material Flows," *Chemical Engineering Science*, Vol. 61, 2006, pp. 5307 – 5317.
- [11] Jain, N., Ottino, J. M., and Lueptow R. M., "An Experimental Study of the Flowing Granular Layer in a Rotating Tumbler," *Physics of Fluids*, Vol. 14, 2002, pp. 572-582.
- [12] Pudasaini, S. P., Hsiau, S. S., Wang, Y, and Hutter, K., "Velocity Measurements in Dry Granular Avalanches Using Particle Image Velocimetry - Technique and Comparison with Theoretical Predictions," *Physics of Fluids*, Vol. 17, 2005.
- [13] Barnett; C. M., Bengough, A. G., and McKenzie, B. M., "Quantitative Image Analysis of Earthworm-Mediated Soil Displacement," *Biology and Fertility of Soils*, 2009, Vol. 45, pp. 821-828.
- [14] Saengprachatanarug, K., Ueno, M., Taira, E., and Okayasu, T., "Modeling of Soil Displacement and Soil Strain Distribution Calculation under the Traveling Wheel," 17th Int. ISTVS Conference, Blacksburg, Virginia, 2011.
- [15] Wong, J. Y., "Behaviour of Soil beneath Rigid Wheels, *Journal of agricultural Engineering*," Vol. 12(4), 1967, pp. 257-269.
- [16] Thielicke, W., and Stamhuis, E. J., "PIVlab – Time-Resolved Digital Particle Image Velocimetry Tool for Matlab," 2010.
- [17] Adrian, R. J., and Westerweel, J., Particle Image Velocimetry, Cambridge University Press, New York, 2011.
- [18] Keane, R. D., and Adrian, R. J., "Theory of Cross-Correlation Analysis of PIV Images," *Applied Scientific Research*, Vol. 49, Netherlands, 1992, pp.191-215.
- [19] Wulfmeier, M., "Development of a Particle Image Velocimetry Method for Analysis of Mars Rover Wheel-Terrain Interaction Phenomena", B.S. Thesis, Gottfried Wilhelm Leibniz Universitaet Hannover, 2012.
- [20] Nagatani, K., Ikeda, A., Sato, K., and Yoshida, K. "Accurate estimation of drawbar pull of wheeled mobile robots traversing sandy terrain using built-in force sensor array wheel," *Proceedings of the International Conference on Robots and System*, pp. 2373-2378, St. Louis, MO, October, 2009.
- [21] Bekker, M. G., Theory of Land Locomotion, University of Michigan Press, Ann Arbor, MI, 1956.
- [22] Reece, A. R., "Principles of soil-vehicle mechanics," *Proc. Instn. Mech. Engrs.*, Vol. 80, Pt 2A No 2, 1965.
- [23] Wong, J. Y., Theory of ground vehicles - 3rd ed., 528 p., New York, Wiley, 2001.
- [24] Karafiath, L. L. and Nowatzki, E. A., Soil Mechanics for Off-Road Vehicle Engineering, Trans Tech Publications, Series on rock and soil mechanics Vol.2, No.5, Clausthal, West Germany, 1978.
- [25] Onafeko, O., and Reece, A. R., "Soil Stresses and Deformations beneath Rigid Wheels," *Journal of Terramechanics*, Vol. 4(1), 1967.
- [26] Wong, J. Y., and Reece, A. R., "Prediction of rigid wheel performance based on the analysis of soil-wheel stresses part I," *Journal of Terramechanics*, Vol. 4, No. 1, pp. 81-98, 1967.

- [27] Wong, J. Y., and Reece, A. R., "Prediction of rigid wheel performance based on the analysis of soil-wheel stresses part II," *Journal of Terramechanics*, Vol. 4, No. 2, pp. 7-25, 1967.
- [28] Janosi, Z., and Hanamoto, B., "Analytical determination of drawbar pull as a function of slip for tracked vehicles in deformable soils," 1st International Conference on Terrain-Vehicle Systems, Turin, Italy, 1967.
- [29] Senatore, C., and Iagnemma, K., "Direct Shear Behavior of Dry, Granular Soils for Low Normal Stress with Application to Lightweight Robotic Vehicle Modelling," *Proceedings of the International Symposium of the International Society of Terrain-Vehicle Systems*, 2011.